EFFECTS OF MICROSTRUCTURE ON CRACK INITIATION IN AA6451 AND CRACK PROPAGATION IN AA3XXX

A Dissertation
Presented to
The Academic Faculty

by

Yung Suk "Jeremy" Yoo

In Partial Fulfillment
of the Requirements for the Degree
Doctor of Philosophy in the
School of Materials Science and Engineering

Georgia Institute of Technology
May 2020

EFFECTS OF MICROSTRUCTURE ON CRACK INITIATION IN AA6451 AND CRACK PROPAGATION IN AA3XXX

Approved by:

Dr. Joshua Kacher, Advisor
School of Materials Science and Engineering
Georgia Institute of Technology

Dr. Olivier Pierron
School of Mechanical Engineering
Georgia Institute of Technology

Dr. Christopher Muhlstein
School of Materials Science and Engineering
Georgia Institute of Technology

Dr. Sazol Das
Global Automotive Technology
Novelis Inc.

Dr. Richard Neu
School of Materials Science and Engineering
Georgia Institute of Technology

Date Approved: March 12, 2020

With undying respect and gratitude,

dedicated to my mother, Gye Young Hwang

ACKNOWLEDGEMENTS

First, I wish to thank my mother, Gye Young Hwang, for raising me into the person I am today. She has always been supportive of my life decisions and encouraged me to pursue my own dreams, even if it meant she would not see me for years. I will forever be indebted to her years of sacrifice. She has always been a patient mother, a tough teacher, and a respectable role model despite facing numerous difficulties that would have crippled an average person powerless. It would have been impossible for me to make it this far without her love and support, which is why this work is dedicated to her.

I would like to thank my advisor, Professor Joshua P. Kacher, for years of guidance, teaching, and most of all, patience. He has been an invaluable mentor, an incredible source of knowledge, and an excellent role model as a passionate researcher. His pedagogy has not only forged me to be an independent thinker, but also molded me to be a studious investigator who never stops asking questions. His patience during dry periods when I could not deliver results or had to restart my experiments has been a bedrock upon which I can find my footing and rebuild my research.

I gratefully acknowledge Novelis Inc. for funding my work and making this research possible. Novelis also provided wonderful experts who provided insightful feedback: Dr. Sazol Das, Dr. DaeHoon Kang, Dr. Richard Hamerton, and Mr. Paul Nolan. I also want to thank Dr. Saryu Fensin and Dr. Stuart Maloy for providing me with the opportunity to work at Los Alamos National Laboratory. I am indebted to them and other colleagues for a truly unique experience of working in a familial group of world-renowned experts and making me feel welcome in an unfamiliar environment. Thank you to Dr. Yong

Ding, Dr. Samson Lai, Dr. Hojun Lim, Dr. Philip Noell, Dr. Ben Eftink, Dr. Thomas Nizolek, Dr. Eric Hahn, and many more for technical support and helpful advice.

I also want to thank the indispensable members of the Kacher Lab who helped me over the years: Jordan, Pragna, Jahnavi, Katie, Sandra, and Xueqiao. I would like to extend special thanks to Jordan for warding off boredom in the office and to Xueqiao for lending her hand in many experiments, without whom my work would have taken much longer. I am also grateful to all the Materials Characterization Facility staff for all their help—Eric, Dr. Ding, Yolande, Mengkun, Walter, and Todd.

I also want to personally thank friends for helping me get through the arduous marathon of graduate school. The friends I met through the Hapkido Club at GT—Hung, Akshay, Mikaela, Mathias, and Anna—have lent me their ears during my times trouble and made my time in graduate school much more tolerable. The other fellow Korean graduate students in the Materials Science and Engineering community have helped me feel at home despite living in one of the most geographically distant locations away from South Korea. In particular, I want to take this opportunity to thank Dong-Chan and Yohan for their extreme generosity helping me settle in when I first moved to Atlanta. I am also grateful to Greg and Onicha Bennett and their extended family for inviting me every year for Thanksgiving and becoming my surrogate family in the US. Thank you Jingjing for reminding me that there is a reason to smile in life and for nursing me back to health during a medical crisis. I also want to thank my significant other, Sabrina, for encouraging me to explore outside my comfort zone to find joy in life and rekindling my interest in artistic hobbies. Without their love and care, I would never have made it to the finish line.

TABLE OF CONTENTS

LIST OF TABLES

LIST OF FIGURES

LIST OF SYMBOLS AND ABBREVIATIONS

a	Diameter of dispersoids
AA3xxx	3000-series aluminum alloy
AA6061	6061 aluminum alloy
AA6061-T6	6061 aluminum alloy subjected to T6 temper
AA6451	6451 aluminum alloy
AA6451-T4	6451 aluminum alloy subjected to T4 temper
AA6451-T6	6451 aluminum alloy subjected to T6 temper
AA6xxx	6000-series aluminum alloy
AR	Aspect Ratio
b_1	Minor axis 1
b_2	Minor axis 2
C	Constant
d	Recrystallized grain size
D&I	Drawing and Ironing
D_{cell}	Cell size
D_{grain}	Grain size
d_{PFZ}	Width of PFZ
E	Young's modulus
EBSD	Electron Backscatter Diffraction
EBSP	Electron Backscatter Pattern
EBSP	Electron Backscatter Pattern
ECAE	Equal Channel Angular Extrusion

ECAP	Equal Channel Angular Pressing
EDX	Energy-Dispersive X-ray Spectroscopy
f	Dispersoid volume fraction
FCC	Face-Centered Cubic
FIB	Focused Ion Beam
GB	Grain Boundary
GBL	Grain Boundary Ledge
GP zone	Guinier-Preston zone
IPF	Inverse Pole Figure
IQ	Image Quality
K_IC	Fracture toughness
m	Strain rate sensitivity
n	Strain-hardening exponent
n_{PFZ}	Work hardening exponent in PFZ
PC	Pattern Center
PF	Pole Figure
r	Dispersoid mean radius
RD	Rolling Direction
ROI	Region of Interest
SEM	Scanning Electron Microscopy
SSSS	Supersaturated Solid Solution
STEM	Scanning Transmission Electron Microscopy
T4	AA6451-T4 sample
T6	AA6451-T6 sample
TE	Total Elongation

TEM	Transmission Electron Microscopy
TKD	Transmission Kikuchi Diffraction
TTT	Time-Temperature-Transformation
UE	Uniform Elongation
UTS	Ultimate Tensile Stress
WD	Working Distance
YS	Yield Strength
ε_{cPFZ}	Critical strain at onset of crack propagation
θ	Angle between grain boundary and tensile load direction corrected for sample tilt
θ'	Measured angle between grain boundary and tensile load direction
σ_{PFZ}	Flow stress in PFZ
τ_y	Critical shear stress

SUMMARY

Aluminum alloys have been enjoying the spotlight in recent years as the next generation alloy for a wide variety of applications. Their potentially waste-free recyclability, excellent corrosion resistance, and desirable balance in physical properties—low density and high strength-to-weight ratio—makes them an ideal candidate material for efficient and environmentally-friendly products. Mechanical properties of aluminum alloys can be engineered to suit the requirements for different functions by controlling the microstructural features. Naturally, the variety of alloying elements, microstructural features, and thermomechanical processes produce complex microstructures that deform heterogeneously under different mechanical loading conditions. To get a better understanding of the microstructure-driven failure mechanism of aluminum alloys, this dissertation will explore the effects of various microstructural features—with particular focus on dispersoids, a type of second phase particle—on the crack initiation and propagation behaviors. A multiscale electron microscopy-approach was employed to correlate different aspects of the microstructure to localized deformation behavior.

This work is divided into two parts. The first part will delve into the crack initiation mechanism of AA6451 during three-point bending and the influence of dispersoids on each step of the process. It will also discuss the effects of variation in alloying elements and tempering conditions on the microstructure evolution and localized deformation behavior of AA6451. The second part involves studying the crack propagation behavior of deep drawn, ironed, and necked AA3xxx. The dispersoid effects on crack growth direction will be discussed in depth.

CHAPTER 1. INTRODUCTION

1.1 Motivation

Aluminum alloys are becoming increasingly more important for a wide variety of uses—AA6451 for automotive body panels and AA3xxx for beverage packaging—for their excellent corrosion resistance and strength-to-weight ratio [1-5]. As aluminum takes the spotlight in more diverse applications, the importance of improved formability, bendability, strength, and ductility were emphasized to ensure quality control during production. In recent years, these improvements were achieved in part by tailoring the density of dispersoids [6-10], an unshearable second phase particle reported to homogenize strain [11, 12].

Although previous experimental and theoretical studies made considerable progress in understanding the dispersoid effects on the bulk mechanical properties, much remains unclear about their role in dislocation structure evolution and failure initiation in highly deformed alloys [9, 13]. This limited understanding of defect interactions with dispersoids on a microscopic level requires an in-depth study that can explain the mechanical behavior observed in the macroscale.

The present work explores the influence of dispersoids on the crack initiation mechanism of AA6451 during hemming and crack propagation behavior in AA3xxx during bottle-forming. A multiscale electron microscopy-approach is used to capitalize on the versatility of diverse electron microscopy techniques. Mesoscale characterization involves

identifying the microstructural features of interest and correlating the deformation features to the bulk mechanical properties. Microscale characterization explores dispersoid interactions with other defects such as dislocations to bridge the knowledge gap between mechanistic understanding of dispersoid effects and bulk behavior.

1.2 Research Objectives

The objectives of this dissertation are as follows:

1. Investigate the crack initiation mechanism in three-point bend tested AA6451 and find the microstructural factors that are conducive to crack formation.
2. Study the dispersoid interactions with dislocations, slip bands, and cracks in bend tested AA6451.
3. Explore the effects of dispersoid-induced strain homogenization on the crack initiation process in bend tested AA6451.
4. Characterize the crack propagation behavior in deep drawn, ironed, and necked AA3xxx.
5. Investigate the effects of dispersoids on the crack growth paths in drawn AA3xxx.

1.3 Map of Dissertation

This dissertation explores the crack initiation mechanism of AA6451 under three-point bending; crack propagation behavior of AA3xxx during deep drawing and necking; and the effect of dispersoids on the two processes. A multiscale electron microscopy-approach was used to perform mesoscale characterization for correlating the deformation features to the bulk characteristics and microscale characterization for studying the microstructural defect interactions.

This dissertation will contain six chapter and an appendix at the end. CHAPTER 1 gives an overview of the dissertation with motivation, hypotheses, and research objectives.

CHAPTER 2 provides background information about AA6451, AA3xxx, and various microstructural defects that pertains to the localized deformation observed in the aforementioned alloys.

CHAPTER 3 explains the experimental procedures in detail: from sample preparation methods and mechanical testing conditions to characterization techniques and analysis tools. Although the procedures that are used for the projects are mentioned again in their respective chapters, they are condensed and organized in logical order. The full details for each procedure are noted in this chapter.

CHAPTER 4 explores the influence of dispersoids on the crack initiation mechanism of AA6451 during three-point bending. Samples with three different compositions and two different tempering conditions were investigated to understand the

effects of varying composition and processing conditions had on the microstructure development. The three-point bend tested samples were first characterized at the mesoscale to analyze a large sample of grain boundaries and draw an outline of the crack initiation process in AA6451-T6 and -T4. The deformed surfaces were further studied to identify the relevant microstructural features conducive to the selective nature of crack initiation sites. Microscale electron microscopy was employed to probe the defect interactions, which mainly focused on dispersoid interactions with dislocation, slip formation, and grain refinement leading to cracking.

CHAPTER 5 discusses the crack propagation behavior in deep drawn AA3xxx and the effects of dispersoids on crack growth directions. Mesoscale characterization was performed to observe the artifacts of drawing, ironing, and necking. Then lamella specimens were prepared from surface cracks for microscale characterization: transmission electron microscopy and transmission Kikuchi diffraction analyses were performed to study the correlation between dispersoids and crack propagation direction.

CHAPTER 6 summarizes the findings from previous chapters and provides ideas for future directions of research to gain a better understanding of the deformation behavior of AA6451 and AA3xxx.

CHAPTER 2. BACKGROUND AND LITERATURE REVIEW

2.1 Hemming Aluminum to Steel in the Automotive Industry

2.1.1 Joining Aluminum Body Panels to Steel Door Frames

The growing demand for more energy-efficient and environmentally friendly vehicles is pushing the automotive industry to develop lighter cars [14]. However, the gross weight of vehicles is limited by their collision safety, which tends to increase with thicker components [15]. To balance market demand and safety standards, automakers capitalize on the high strength of steel and excellent strength-to-weight ratio of aluminum by using both alloys for different components. For aluminum parts, the most commonly used alloy is the 6000-series aluminum alloy (AA6xxx), a class of heat-treatable alloy containing Mg and Si as principal alloying elements [16]. The heat-treatable aspect of AA6xxx makes it a versatile alloy whose strength and ductility can be engineered by changing the post-process annealing condition called tempering.

The burgeoning use of two different alloys requires improved joining methods [15]. There are several classifications of metal joining techniques: thermal, adhesive, and mechanical. The thermal joining methods involve using heat to fuse the metals together (*i.e.* welding). Resistance spot welding, which has been a common welding technique in the past to join two steel parts together, is not applicable for aluminum components because of its high thermal conductivity, low melting point, and passive oxide layer [17]. The weld can also yield brittle steel microstructure that is more susceptible to cracking [15].

Adhesive joining techniques bond metal parts using epoxy or solvent-based chemicals [17]. The main advantages of this technique include sealing against corrosive environment, improved joint stiffness, low-cost, and undistorted parts. Unfortunately, the chemicals can pose environment and safety hazards on top of their limited shelf life that requires proper disposal. This process is also energy- and time-intensive: the chemicals need heat curing to complete the joining process. The adhesives also require pre-treatment to remove the passivating oxide layer and provide immediate contact with aluminum, which adds cost and complexity to the manufacturing process.

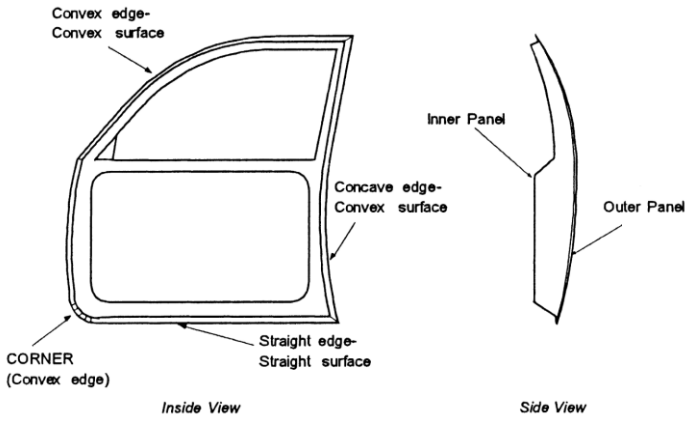

Figure 1. Various hemming shapes for automotive door panels [18]. Reprinted with permission from Elsevier.

Both welding and adhesive techniques are plagued with problems that arise from aluminum's passive oxide layer. One way to resolve this issue without adding too much complexity to the manufacturing line is mechanically joining the components by plastic deformation. An example of mechanical joining is hemming, which is a process that binds aluminum body panels made from AA6451 to steel door frames (**Figure 1**) [15]. It is an attractive alternative because of its high productivity and low cost.

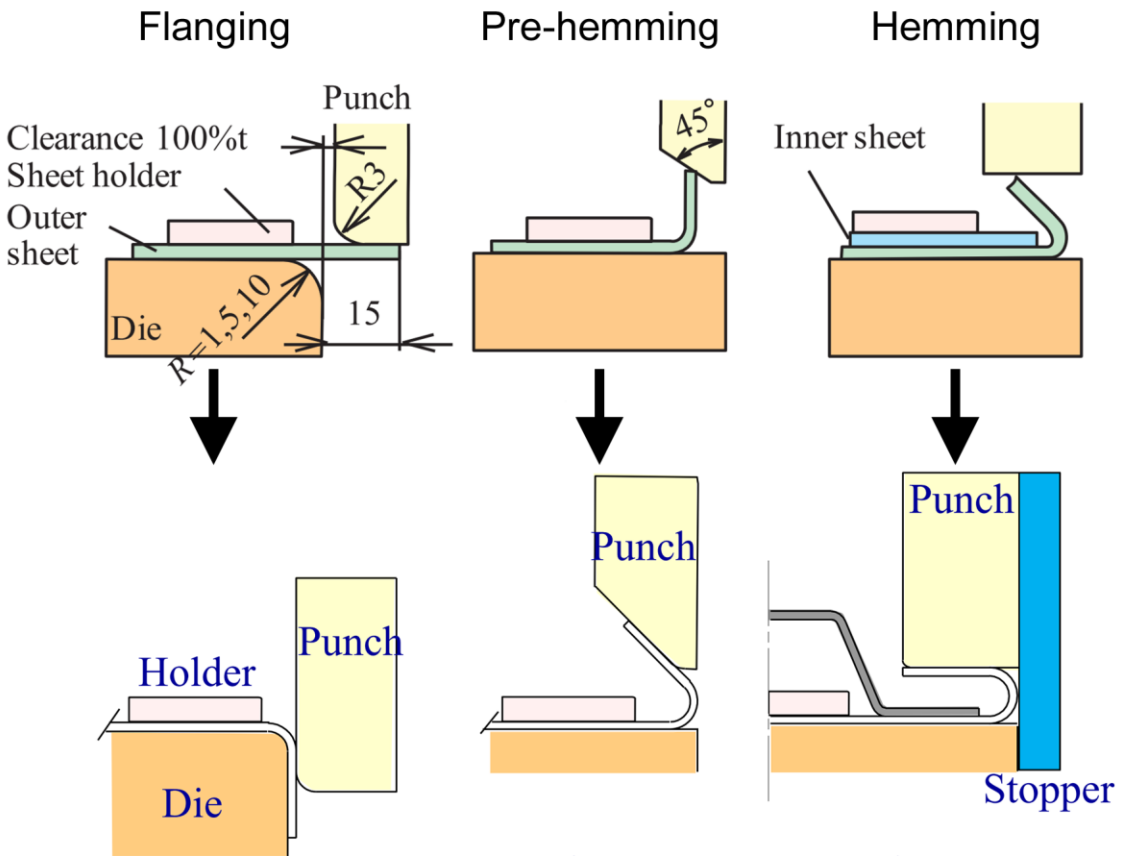

Figure 2. Illustration of the three steps in hemming: 1) flanging, 2) pre-hemming, and 3) hemming [15, 19]. Reprinted with permission from Elsevier.

As illustrated in **Figure 2**, conventional hemming joins the aluminum body panels to steel door frames in three major steps [14, 15, 19, 20]. First, the edge of the aluminum part is bent 90° during the flanging (or bending) stage. This is followed by the pre-hemming stage where the aluminum sheet is turned over and bent further to 135°. The bent sheet is then aligned with the steel door frame and finally hemmed together as it wraps around the edge of the steel frame. The two parts are essentially clamped together at the edges by plastic deformation. Another hemming method, called rolling hemming, involves a cylindrical roller that continually folds the aluminum sheet instead of in discrete steps [21].

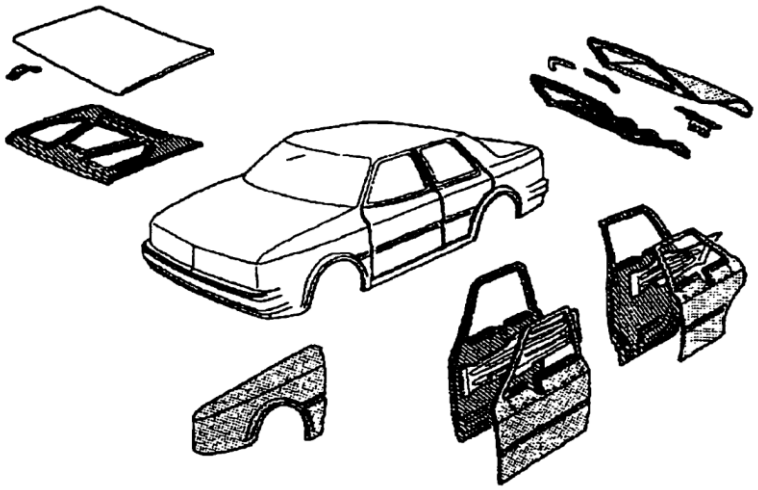

Figure 3. Flanged and hemmed parts on a car [22]. Courtesy of Dr. Haydar Livatyali.

As shown in **Figure 3**, hemming is used to join a wide variety of parts because it is material-agnostic, meaning that it is applicable to different materials because it does not involve phase changes. This versatile process, however, is limited by the level of plastic deformation that the materials must undergo. The hemmed alloy must have sufficiently high ductility to withstand the level of plastic deformation.

2.1.2 Challenges in Hemming

Since hemming is one of the last steps that the body panels undergo, it has considerable influence on the quality of the final product [20, 23-25]. **Figure 4** shows several common defects of the hemming process. Roll-in (creep) and roll-out (growing) are changes in the dimensions of the final product as a result of the flanging and pre-hemming. Although they are not necessarily considered as "defective" because they do not change the overall appearance of the part. However, their values must be uniform along the edges to ensure the visual quality and to maintain quality control. Recoil and warp are

swelling and collapsing, respectively, of the hemmed component. They are reported to be caused by misalignment of the supporting dies and holders during the hemming process and require additional post-hem finishing processes. The hemmed edge must follow the curves of the car part that it wraps around. As a result, there are segments along the perimeter where the local strain exceeds the critical tensile and compressive values, resulting in splitting at concave and wrinkling at convex edges, respectively. The segmentation has an added implication of producing hem-out, which refers to the production of unwanted corners as a result of segmentation of curved edges. Many of these problems can be mitigated by optimizing the manufacturing parameters such as flange corner radius, edge geometry, and hemming load.

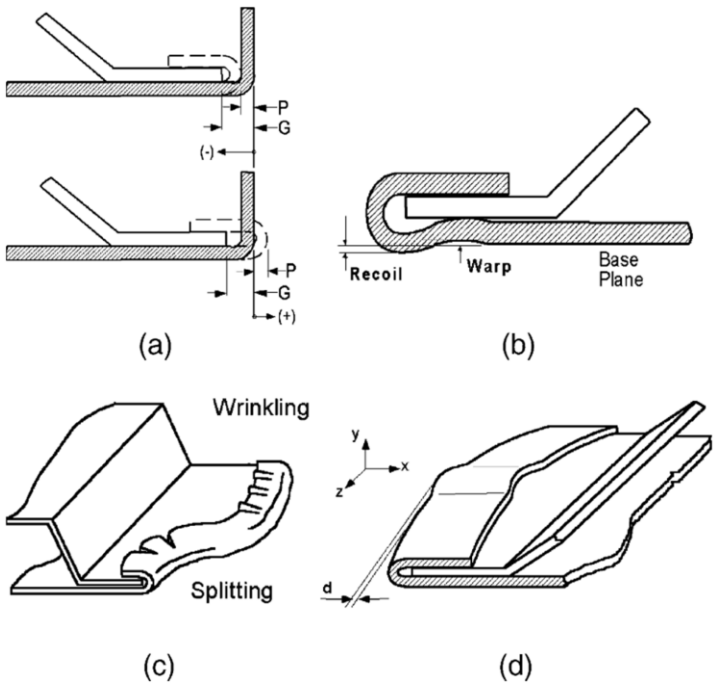

Figure 4. Common hemming defects: a) roll-in (-) and roll-out (+); b) recoil and warp; c) wrinkling and splitting; and hem-out [23]. Reprinted with permission from Elsevier.

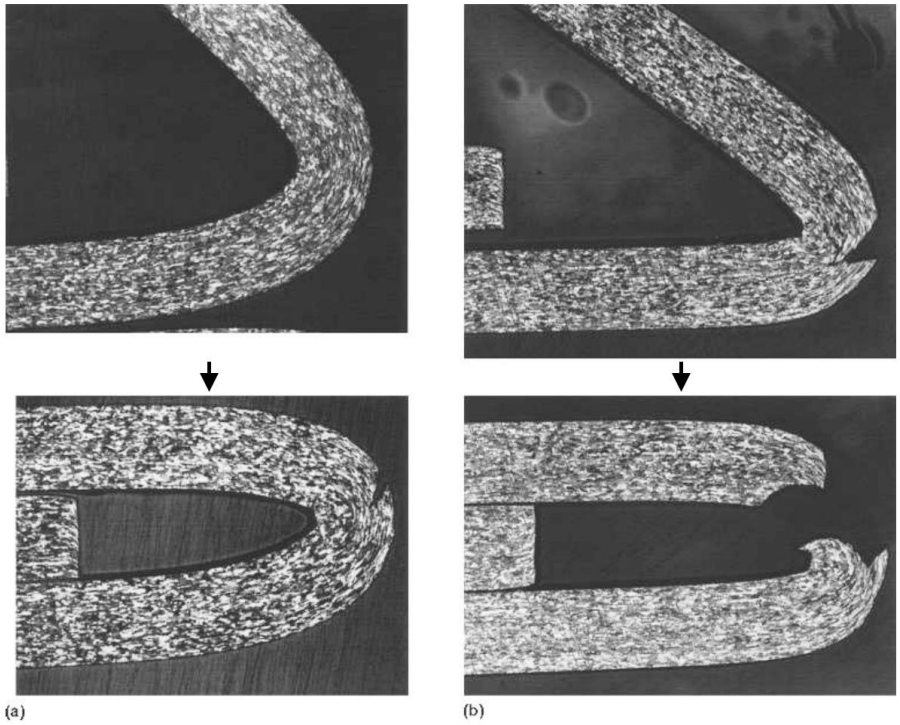

Figure 5. Examples of cracks forming during a) hemming and b) pre-hemming [26]. Reprinted with permission from Springer Nature.

There are more specific problems that arise from using aluminum. Although renowned for its ductility, aluminum is a difficult alloy to hem because of strain localization, which leads to cracking in the outer plane (**Figure 5**), where the aluminum component experiences the highest tensile stress [14, 21]. Moreover, stamped aluminum parts have exhibit enhanced spring-back than conventional steel because of its high strength-to-Young's modulus ratio [14]. Therefore, it is crucial that AA6xxx is ductile enough to be hemmed without significant cracking while strong enough for safety standards. The challenge lies in balancing the two mechanical properties to optimize the manufacturing process and decrease the defect rate by controlling the second phase particles, such as strengthening precipitates and strain-homogenizing dispersoids.

2.2 Deep Drawing and Ironing Aluminum for Beverage Containers

2.2.1 Aluminum Cans and Bottles

Hosford and Duncan chronicled the history of aluminum beverage cans in [27]. The history of beverage cans begins with three-piece steel cans first produced by Kreuger Brewing Company in 1935 as food containers. The three pieces consisted of a rolled and seamed cylinder with two flat end pieces.

Then came the two-piece aluminum can, composed of the body and the lid, developed by Adolph Coors Company in 1958. Coors used the impact-extrusion process, where the base and the wall of the can was produced by punching an aluminum sheet with a circular slug equal to the diameter of the can, and the top piece was added after filling the bottom piece with its contents. Unfortunately, the impact-extrusion process was unfit for mass production because of its slow speed and tooling problems. The final product required the base to be at least 0.03 inches thick while limited to storing 7 ounces of beverages.

A critical breakthrough for widespread commercialization of aluminum cans came in 1963, when Reynolds Metals Company (of aluminum cooking foil fame) developed a more economical and robust manufacturing method. An aluminum alloy containing the appropriate amounts of alloying elements is cast into an ingot, which is then flattened into sheets using rolling mills. For the can's body, the sheets are then cut into circular blanks and deep drawn to take the shape of a cup, as shown in **Figure 6**.

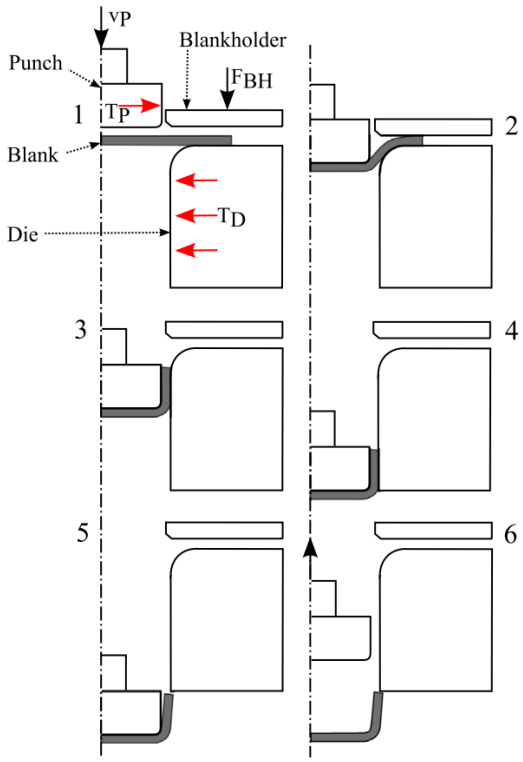

Figure 6. Schematic of a deep drawing process [28]. Reprinted with permission from Elsevier.

Illustrated in **Figure 7**, the following procedures subject each cup to three different forming processes in one continuous stroke of a punch. The first of the three is redrawing the cup to a final interior diameter, which increases the height of the wall of the can body. The redrawn cup is then passed through several ironing dies with subsequently smaller diameters, which increases the height while thinning the wall. The can body then hits a metal dome that give the bottom of the can a concave bulge. This bulge is designed not only to keep the can's bottom from bulging outward from the internal pressure, but also to distribute the internal pressure from the contents evenly to minimize rupturing. The bottom of the wall where it meets the base is designed to be thicker to achieve better structural

integrity. During the deep drawing and ironing (D&I) processes, the can bodies experience high level of mechanical deformation within a short amount of time—approximately one-fifth of a second—and therefore it is imperative that the alloy can withstand such a rigorous process without exhibiting critical failure.

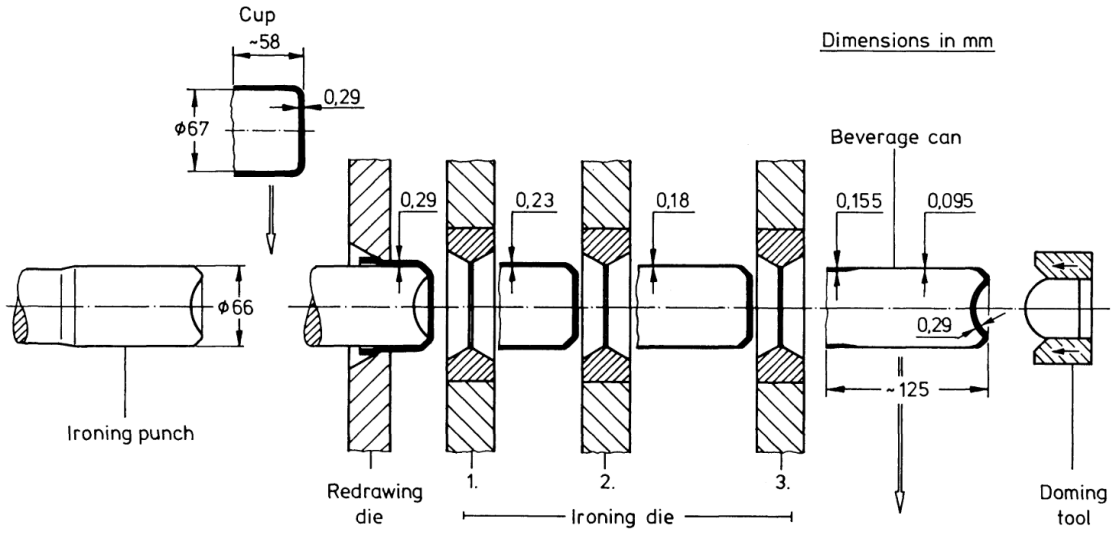

Figure 7. Redrawing and ironing [29]. Courtesy of The Iron and Steel Institute of Japan.

The top of the side wall is trimmed to remove the wavy "eared" edges to conform to having the same height before being decorated. The interior side wall is cleaned and coated to protect the can from its acidic contents while keeping the aluminum from dissolving into the beverage. Before being filled with its liquid contents, the opening diameter of the can body is reduced by necking. The tapered neck of the can body serves a dual role of reducing the diameter to meet the lid while avoiding strain concentration at the seam that joins the two pieces. The lid, which is made with a stronger aluminum with less Mn and more Mg, is thicker than the side walls and constitutes about a quarter of the can's

weight. As a measure to save material and cost, its diameter is made smaller than that of the can body. A can is ready for transport and consumption once it is filled and seamed.

Similarly, the production of aluminum bottles involves drawing, D&I, and necking manufacturing sequence [30, 31]. One notable difference for the bottle production aside from higher wall height is that it has additional necking processes that tapers the top of the side walls and creates threads for the bottle cap, which exerts more strain on AA3xxx [32].

After five decades of innovation, the aluminum cans have all but replaced their steel predecessors by the 1980s. Currently, 3000-series aluminum alloys (AA3xxx) is a widely used alloy for aluminum cans and bottles. 3000-series aluminum alloy is a class of non-heat treatable Al alloys whose principal alloying element is Mn [3-5, 16, 33]. It was chosen as the optimal alloy for beverage containers because of its strength and corrosion resistance. AA3xxx has been used in a variety of applications including architecture [2-5].

The improvements that made the aluminum can manufacturing a cost-effective and reliable process involves not only precise dies and intelligent design, but also microstructure control of the aluminum sheets [27]. Over the years, in order to save material and reduce production cost, the deep drawing processes were optimized to produce thinner can walls while being able to withstand the internal pressure. The key challenge is to design aluminum sheets that were strong enough to withstand the extreme strain from the deep drawing and ironing processes while ductile enough to be easily shaped and resistant to cracking.

2.2.2 Challenges of Deep Drawing and Ironing

As mentioned previously, D&I are sheet metal forming processes that can quickly mass-produce cans and bottles for the beverage packaging industry [34, 35]. They are critical steps in aluminum can and bottle production that combines aspects of bending, stretching, compression, and shearing [34]. Due to the severity of the deformation process, the materials can fail during production. The following gives a brief description of the origin of several common defects (**Figure 8**) and solutions for mitigation.

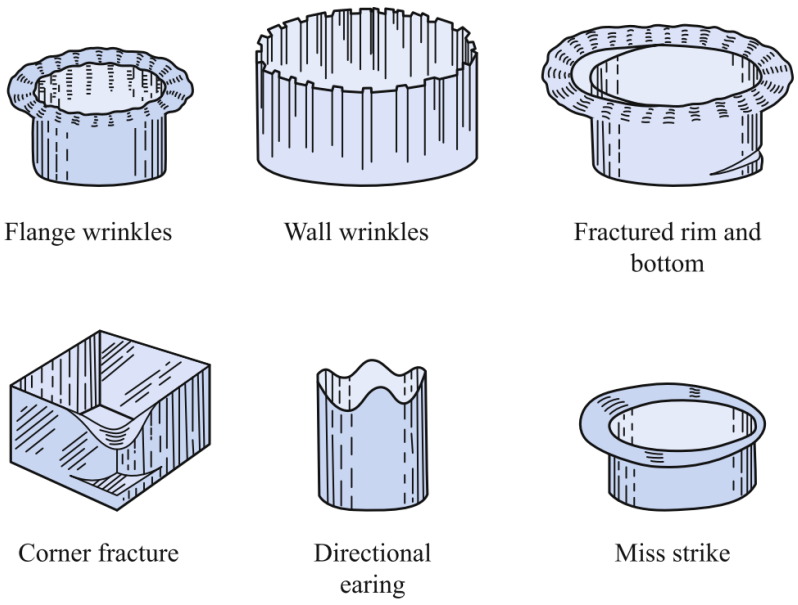

Figure 8. Various types of common deep drawing defects [36]. Reprinted with permission from Springer Nature.

Tearing is the separation of the base and the wall caused by excessive stress and thinning from the punch radius [36]. This can be mitigated by decreasing the punch load and black holder pressure while minimizing thinning. Wrinkles are series of ridges

resulting from compressive hoop stresses buckling the blank sheet. This occurs as a result of high punch loads that induce compressive hoop stress above the critical threshold at the flange of the cup. Wrinkles at the flanges can extend to the wall if the blank holder does not exert enough hold-down pressure. However, excessive hold-down pressure and blank holder friction can cause fracture at the rim, bottom, and corner of the can body. Miss strike occurs when a blank is not placed properly over the drawing die, resulting in asymmetrical flanges. These challenges are usually overcome by optimizing the processing design and parameters to avoid defective can bodies.

Some problems require material science expertise for solutions. For example, earing refers to the uneven wavy height of the top of the can body after D&I. The anisotropic nature of polycrystalline sheets causes varying levels of plastic strain [36]. Smaller ears can be achieved by controlling the two predominant textures that arise from hot rolling ingots and cold rolling sheets [27]. The two textures complement each other so that the trough in the wavy pattern that would be caused by one texture is filled by the crest of the other, essentially canceling out the “wave”. In addition, the defect rate from radial cracking can be decreased by engineering an alloy with higher ductility that can endure the large geometry change [36].

Improving the production of aluminum cans and bottles is of keen interest to materials engineers, and the key is to tailor the microstructure to produce more ductile and resilient aluminum alloys that can withstand the harsh processing conditions. One aspect of the microstructure that has significant influence on their mechanical properties is the presence of second phase particles.

2.3 Effects of Secondary Phase Particles on Localized Deformation

The mechanical properties of aluminum alloys are engineered by controlling the microstructural features. This is achieved by optimizing the composition and the thermomechanical processes. The variety of alloying elements and post-processes produce complex microstructures that deform heterogeneously under different mechanical loading conditions. Therefore, it is important to understand the influence of various microstructural features on the localized deformation behavior of alloys. The most commonly observed second phase particles that affect the mechanical properties are constituent particles, dispersoids, and precipitates. Each of these three particles serve different roles in failure initiation. This section will elaborate on their roles in microstructure control and mechanical properties.

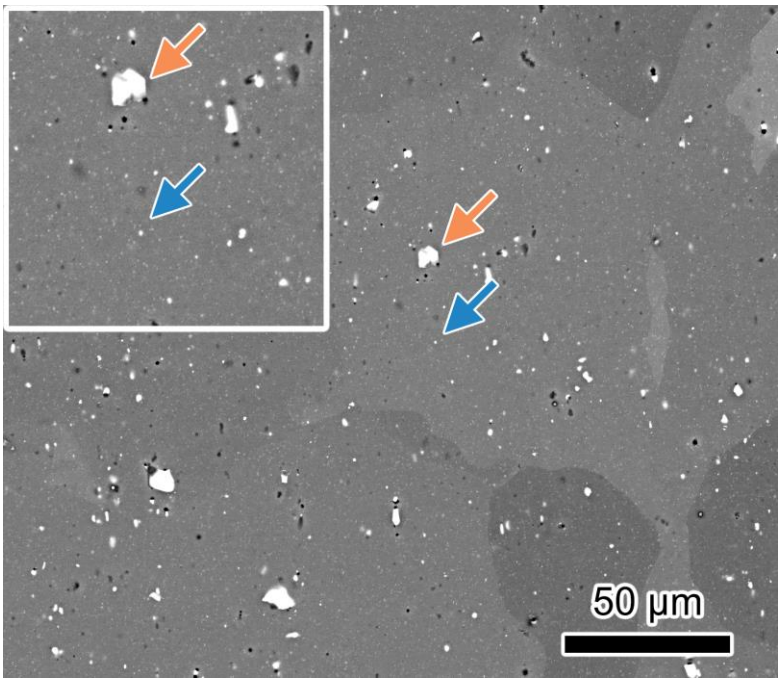

Figure 9. A scanning electron microscopy image showing constituent particles (orange arrows) and dispersoids (blue arrows). The arrows point to the same particles in the inset.

2.3.1 Constituent Particles

2.3.1.1 Constituent Particle Nucleation

AA6xxx typically contain approximately 1 vol% of constituent particles—a type of secondary phase particles—ranging from 1 to 10 μm [37]. The two most common species of constituent particles are plate-like monoclinic β-AlFeSi and spherical cubic α-Al(Fe, Mn)Si particles with slight variations in stoichiometry [16, 37]. These particles are intermetallic compounds that form as a product of various unavoidable alloying elements: during initial solidification, the impurity elements are precipitated out of the Al matrix and coalesced into various intermetallic compounds [16]. The constituent particles are thermally stable, meaning that they do not dissolve once precipitated in the alloy. The formation of constituent particles is largely inevitable due to the leftover impurities in the refinement process or the excess alloying elements to ensure the necessary density of desired second phase particles (*e.g.* dispersoids and hardening precipitates).

Constituent particles are generally undesirable for several reasons. First, they leach the alloying elements required for precipitate hardening [16]. Pitting corrosion have been reported to preferentially form around constituent particles, and the pits act as strain concentration sites that facilitate fatigue crack nucleation [38-41]. More importantly, constituent particles are responsible for dislocation pileup and slip concentration during mechanical tests that ultimately nucleate voids that can cause failure, which will be discussed in further detail in the next subsection. Normally, the only way to reduce these problems is to reduce the Fe and Si content to increase interparticle spacing [16].

2.3.1.2 Constituent Particles and Failure Initiation

This subsection has been adapted from a previous publication by the author [42].

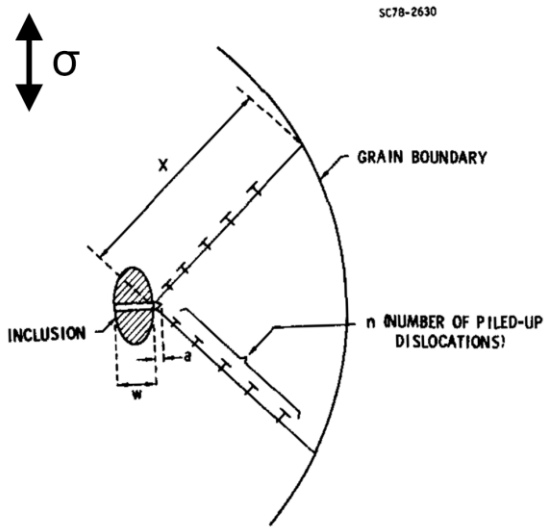

Figure 10. Schematic of dislocation pileup at a constituent particle (inclusion) in a grain [43]. Reprinted with permission from Elsevier.

There is an abundance of previous studies that studied the influence of second phase particles on the failure initiation process of AA6xxx alloys [6, 37, 42, 44-46]. These studies have shown that crack formation occurs preferentially at intermetallic particles, either via particle decohesion from the matrix or by a crack forming in brittle particles and extending into the surrounding matrix [42]. Ghahremaninezhad and Ravi-Chandar combined scanning electron microscopy (SEM) imaging and digital image correlation (DIC) to investigate strain localization and crack formation processes [44, 45]. They found that crack formation initiates late in the deformation process and is driven by decohesion and cracking of Fe-rich intermetallic particles. In addition, they observed that damage accumulation was almost exclusively localized to roughly within one grain diameter from

the crack location. Lassance et al. investigated the influence of intermetallic particle orientation on the local void formation mechanisms in AA6060 and AA6002 [37]. They found that void formation near particles with their long axis oriented at an angle smaller than 45° with respect to the loading axis were more likely to form via particle fracture, while those with long axis oriented greater than 45° formed voids via decohesion mechanisms. The voids then grew under applied strain conditions, eventually coalescing and leading to fracture. *Post mortem* fractography confirmed that void formation was strongly correlated with the presence of intermetallic particles. Therefore, the resistance to damage and fracture depends thus directly on the nature, shape, distribution and volume fraction of the second phase particles [37].

While a correlative understanding between intermetallic particle location, size, and orientation now exists, little is known of the dislocation processes and microstructural evolution preceding and accompanying the void formation process. Much of the understanding of void formation processes is driven by the local stress and state and elastic energy conditions [46-50]. Early models by Stroh and Ashby attributed particle crack formation to stresses associated with dislocation pileup formation at the particle/matrix interface, illustrated in **Figure 10** [51, 52]. Chang et al. proposed a 2-stage dislocation-based model for crack formation at intermetallic particles during cyclic loading involving first the particle cracking, initiated when the combined influence of global applied stresses and local stresses due to pileup dislocations reached a critical level, followed by crack propagation into the surrounding matrix [43]. Particle cracking occurs when the following relationship is satisfied:

$$k_1 w^3 S' n \geq W_c \tag{1}$$

where k_1 is a material parameter, w is the approximate width of the particle, S' is an effective stress that incorporates the applied and internal stress, n is the number of dislocations piling up at the particle, and W_c is a critical internal elastic strain energy leading to crack formation. Once formed, the particle crack acts as an embryo for a crack extending into the surrounding matrix. The crack extension can again be understood in terms of local stored elastic strain energy, dependent on the local stress state (arising from applied stresses and the dislocation pileup at the boundary) and the size of the crack embryo or size of the cracked particle. While the relationship in equation (1) was developed with applications for fatigue failure in mind, it was based on available theoretical work using Eshelby's approach to determine matrix-particle interaction under plastic deformation in uniaxial extension, making it also relevant to ductile crack nucleation [53]. In addition, it has been observed that while larger particles tend to fracture, smaller particles lead to void nucleation through particle-matrix debonding [54] and the mechanism may be dependent on particle shape and particle clustering orientation relative to loading direction [55, 56]. Brown and Stobbs developed a stress-based nucleation criterion for debonding where the stress at the particle-matrix interface is given by [57, 58]:

$$\sigma_c = \frac{\mu b \sqrt{\rho}}{2\pi} \tag{2}$$

where σ_c is the interfacial strength, μ is the shear modulus, b is the Burger's vector, and ρ is the local dislocation density. These proposed mechanisms highlight both the role of

dislocation accumulation and generation in the void formation process as well as the influence that the surrounding microstructure can have.

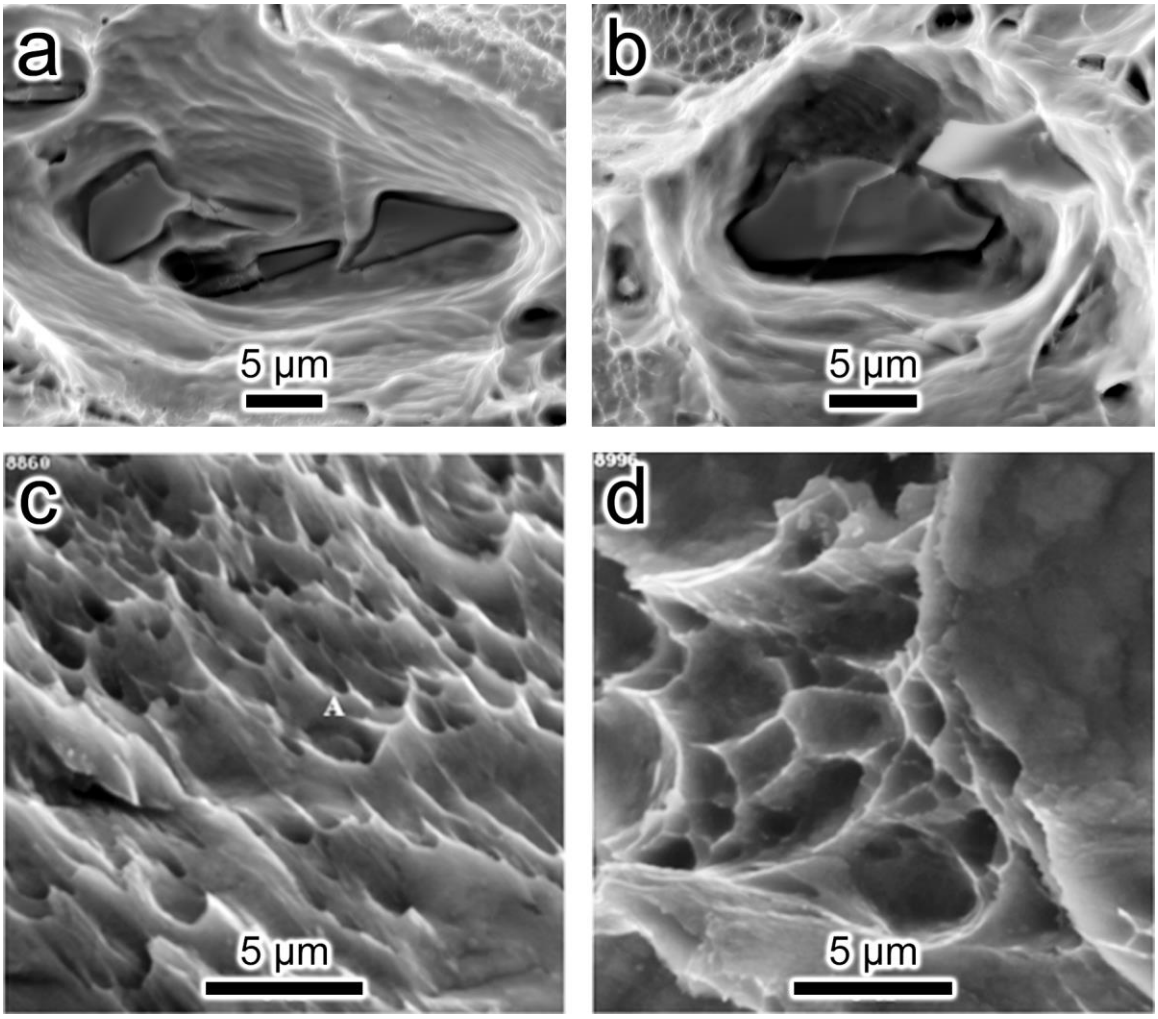

Figure 11. a-b) SEM images of fracture surfaces of tensile tested AA6451-T6 showing dimples and cracked constituent particles at their centers. The black arrows show smaller dimples. Fracture surface SEM images of c) AA6061-T6 and d) overaged AA6061 [59]. The white "A" highlights a dimple with a precipitate at the center. Reprinted with permission from John Wiley and Sons.

2.3.2 Dispersoids

2.3.2.1 Dispersoid Nucleation and Microstructure Control

Dispersoids are intermetallic compounds with diameters ranging from 20 to several hundred nanometers [60]. In alloys with Mn and Cr alloying elements, the dispersoid composition is α-Al(Mn, Fe/Cr)Si [61]. There is strong evidence that the crystal structure is dictated by the ratio between Fe and Mn, where a high Mn:Fe ratio yields simple cubic while a low ratio produces body centered cubic [3, 4, 61].

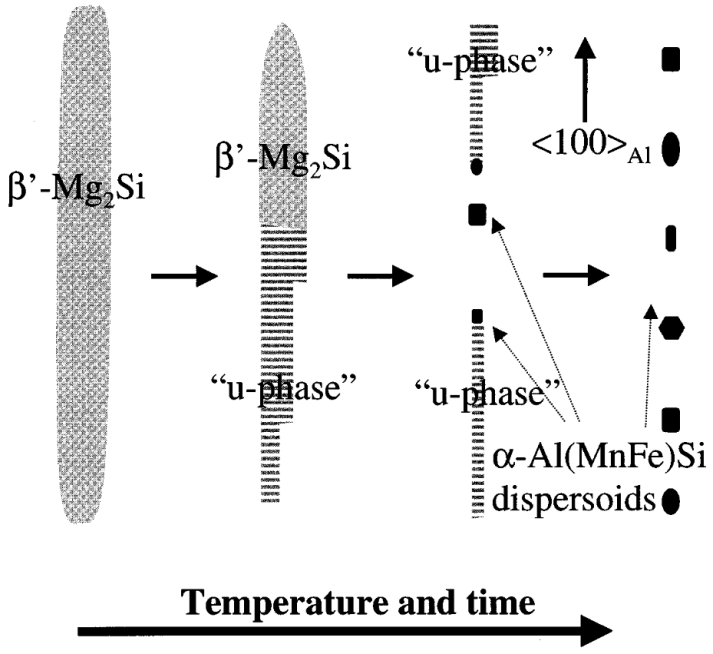

Figure 12. Dispersoid nucleation mechanism in AA6xxx with an intermediate "u-phase" [61]. Reprinted with permission from Elsevier.

Dispersoids are precipitated out of the matrix during the homogenization, a critical heat treatment process where microsegregation of Mg and Si are reduced [62]. For alloys

that contain Mg_2Si precipitates (**Figure 12**), such as AA6451-T6, the precipitates nucleate first along the $<100>_{Al}$ direction in the matrix and once dispersoids are nucleated preferentially at the precipitate interface, and Mg_2Si is slowly consumed as it turns into an intermediate "u-phase" that leads to dispersoid nucleation [60, 61, 63, 64]. Therefore, the distribution of Mg_2Si precipitates have a direct influence on the inter-dispersoid spacing and dispersoid density. For AA3xxx, the precipitation mechanism is slightly different: Kamat *et al*. reported that dispersoids nucleated on large Al_6(Mn, Fe) primary particles that formed during initial solidification [65].

There are several factors that impact the formation of dispersoids. The composition of dispersoids depends on the chemistry, where Fe and Si drastically decrease the Mn solubility and accelerates the precipitation of dispersoids [4, 66]. Dispersoid size increases with higher homogenization temperatures and holding times [4]. The distribution of dispersoids is correlated with heating rate and distribution of Si, where slow heating rate and uniform distribution of Si (possibly in the form of Mg_2Si) promotes uniform distribution [61]. Uniform distribution of dispersoids is an important quality for controlling the microstructure evolution because of their role in the process.

Dispersoids have a significant influence on recrystallization, recovery, texture, and grain size that affects the mechanical properties of aluminum [4, 67-69]. Alloys with dispersoids contain smaller grains as a result of dispersoids pinning grain boundaries during recrystallization and preventing subsequent grain growth [60, 70]. An even distribution of dispersoids translates to relatively homogenous grain sizes throughout the microstructure, resulting in less strain localization that can induce failure.

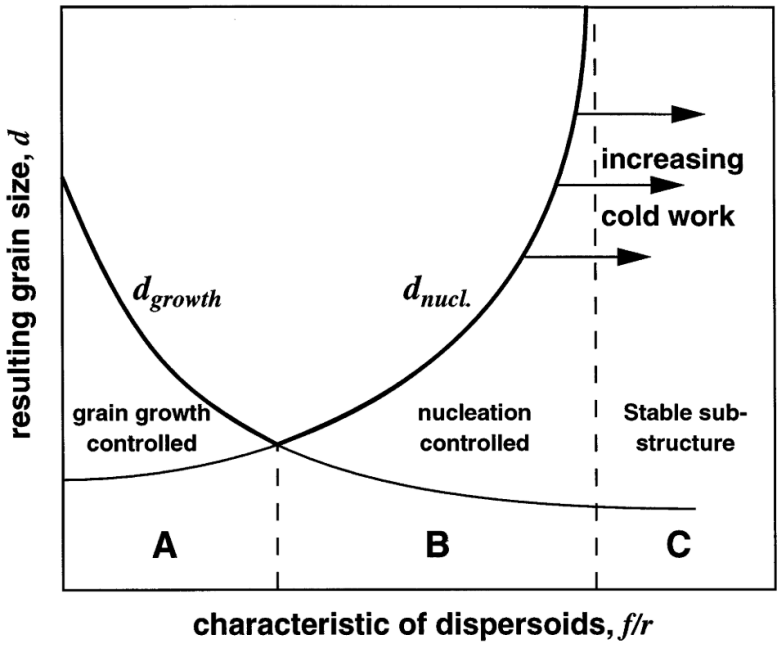

Figure 13. Grain size after recrystallization as a function of dispersoid characteristic [70]. Reprinted with permission from Elsevier.

An example of microstructure control with second phase particles is discussed by Eschbach *et al.*, where constituent particles drive nucleation of recrystallization and dispersoids inhibit grain growth [70]. In this model, dispersoids exert Zener pinning pressure, which depends on the volume fraction (f) and mean radius (r) of dispersoids, that dictates the resultant recrystallized grain size (d). Constituent particles serve as nucleation sites for recrystallization. The driving force for grain growth—reduction of surface energy—is counterbalanced by the Zener pressure. High Zener pressure increases the critical particle size for nucleation and thereby decreases the number of potential nucleation sites. These relationships ultimately affect the grain size, which is summarized in **Figure 13**. Therefore, grain size can be controlled by tailoring the dispersoid character (f/r) with thermomechanical processes.

2.3.2.2 Dispersoid Effects on Mechanical Behavior

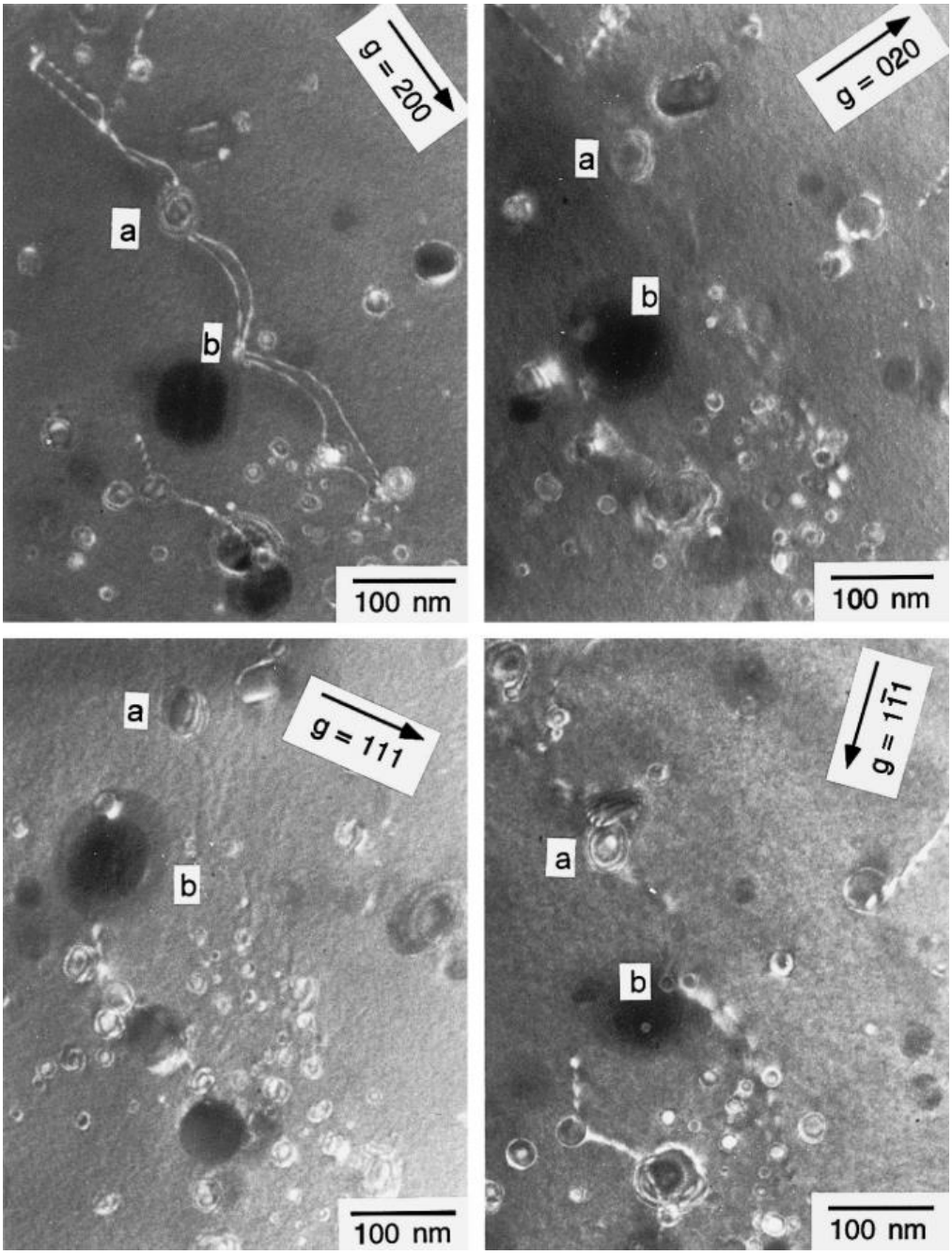

Figure 14. Weak-beam dark field transmission electron microscopy (TEM) images of dislocations around di at various diffraction conditions in an oxide-dispersion strengthened Ni_3Al alloy [71]. The image on the top left shows Orowan bowing around dispersion particles. Reprinted with permission from Elsevier.

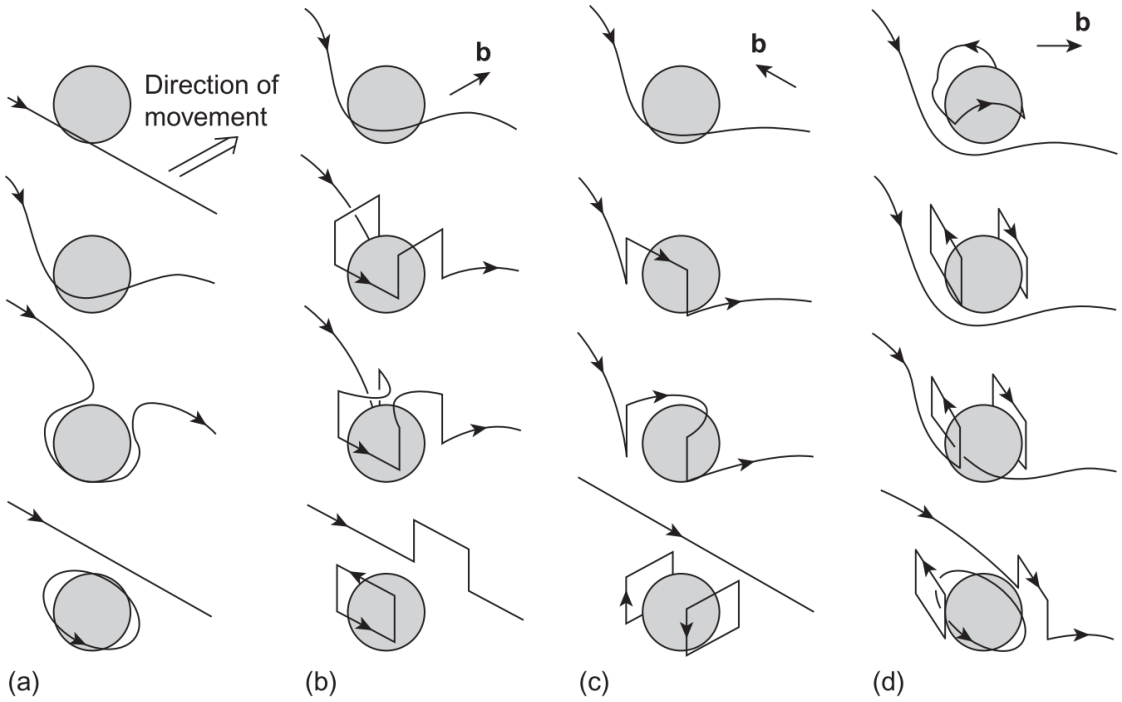

Figure 15. Dislocation motion past a dispersoid a) without and b-d) with cross slip leaving behind an a) Orowan (prismatic) loop, b-c) shear loops, or d) a combination of both [72]. From Hirsch and Humphreys (1969), *Physics of Strength and Plasticity*, p. 189, M.I.T. Press. Reprinted with permission from Elsevier.

Numerous case studies reported attributed increase in tensile strength [6-8], toughness [7, 9], and ductility [10] to dispersoids. Dispersoid influence on the mechanical properties largely stems from strain homogenization, sometimes also referred to as slip homogenization [7, 9-11]. Dispersoids are unshearable largely because of the incoherent particle-matrix [4, 11, 12, 61, 62]. The motions of dislocations are inherently tied to the crystal planes, and dislocations cannot transmit through the particle-matrix interface. As a result, the dispersoids pin dislocations, resulting in Orowan bowing (**Figure 14**, top left) and dislocation accumulation [10]. As shown in **Figure 15**, dislocations require additional energy to form cross slip or prismatic loops to pass through dispersoids [7, 73]. In the end,

dislocations tend to accumulate around dispersoids as the alloy deforms under mechanical loads.

Strain homogenization occurs around dispersoids when the accumulated dislocations initially strain harden the active slip plane and promote dislocation glide on a different slip system [11]. Essentially, dispersoids promote cross slip as applied strain increases, and plastic strain is distributed evenly across multiple active slip systems [7].

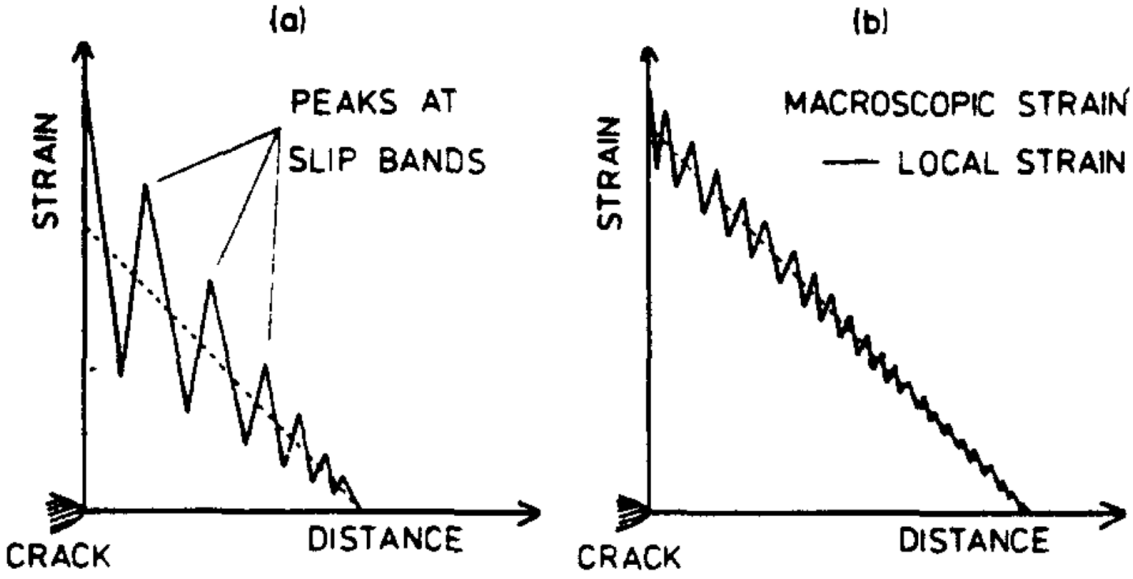

Figure 16. Strain profile ahead of crack tip in alloys with a) few and b) numerous dispersoids [9]. Both alloys reach the same maximum local strain, but the former has higher strain concentration. Reprinted with permission from Elsevier.

The ability to disperse plastic strain has a direct impact on the overall mechanical properties of aluminum alloys. Dowling and Martin illustrated that the strain homogenization is reflected by the increase in slip band spacing [11]. In other words, slip bands that are few and far in between will exhibit higher strain concentration than slip bands that are closely and evenly spaced in the matrix. Lee and Nam concluded that

dispersoid-induced dispersion hardening was responsible for higher work hardening exponents in aluminum alloys, which combined with strain homogenization, leads to increased fracture toughness [7]. Prince and Martin noted that increase in toughness with increase in dispersoid density is due to the decrease in strain concentration ahead of the crack tip [9]. They noted that the fluctuation in the strain profile ahead of crack tip can be dampened by the presence of dispersoids by strain homogenization, thus requiring higher applied strain to increase the local strain ahead of the crack tip for incremental crack growth (**Figure 16**). Dispersoids have also been found to be correlated with delaying fatigue crack nucleation during low cycle fatigue of Al-Mg-Si alloys [74]. Davidson and Lankford observed that the increase in dispersoid mean free path is directly related to decreases in local strain amplitude and delays fatigue crack propagation, ultimately increasing the fatigue life of AA7xxx [75]. They also concluded that the mean free path between dispersoids affects fatigue crack growth rate than other factors, such as grain size, hardening precipitates, and composition. Therefore, dispersoids facilitate even distribution of plastic strain and slip that reduces strain concentration, thereby delaying failure initiation.

Dispersoids can exert indirect influence on the mechanical properties as well. Alloys are deliberately designed with dispersoids because the Zener drag imposed on the recrystallized grains reduce the final grain size [13, 70] that increases their strength according to the Hall-Petch relationship [76]. Dispersoids have also been reported to influence the microstructure texture [77].

2.3.3 Hardening Precipitates and Precipitate Free Zones

2.3.3.1 Mg_2Si Precipitation and Formation of Precipitate Free Zones

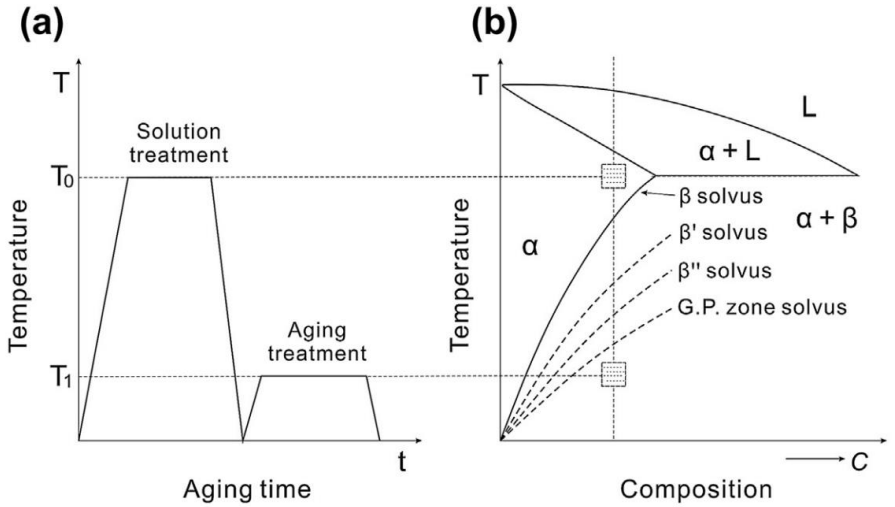

Figure 17. a) Heat treatment scheme for T6 and b) part of a binary phase diagram for precipitation hardenable alloys [78]. Reprinted with permission from Elsevier.

The strength of heat-treatable aluminum alloys—such as AA6451—can be modified by aging after solution heat treatment [16]. The tempering conditions are designated to produce wrought aluminum alloys that satisfy the specifications necessary for different applications. In this dissertation, AA6451 subjected to T4 and T6 tempers were three-point bend tested. T4 temper aluminum is solution heat treated and naturally aged to a stable temper whereas T6 aluminum is solution heat treated and artificially aged at an elevated temperature (225 ± 3 °C for 30 min for AA6451-T6), as shown in **Figure 17**. The temperature range of the aging process promotes the nucleation of β-Mg_2Si hardening precipitates (**Figure 18a**). Constituent particles and dispersoids are stable at aging temperatures, and the tempering process does not affect their size and density [16].

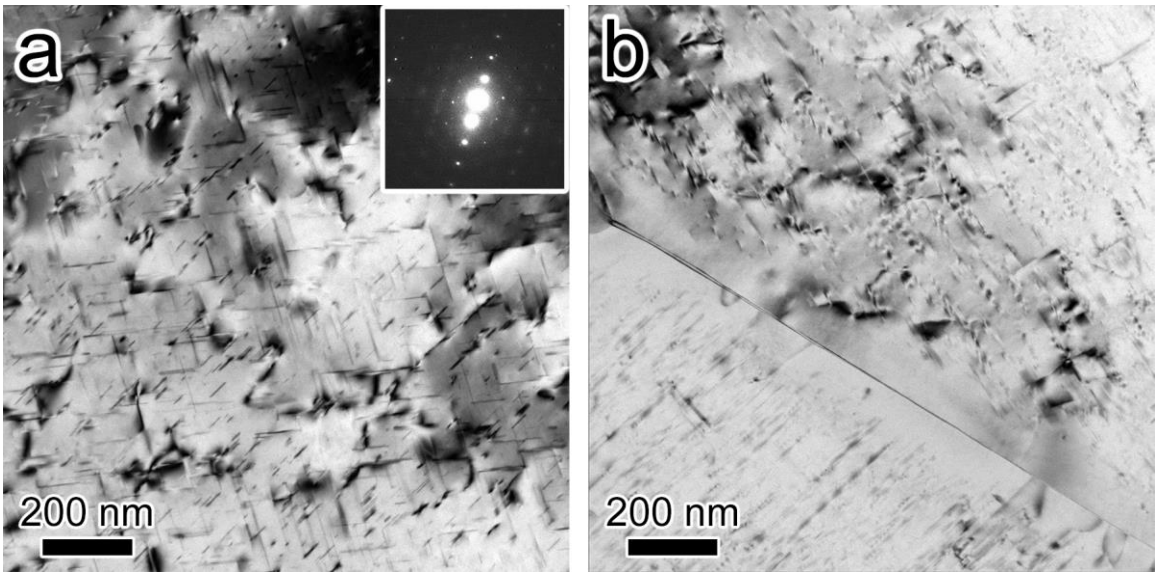

Figure 18. Bright field transmission electron microscopy images of a) precipitates and b) a precipitate free zone in AA6451-T6.

The β-Mg_2Si precipitation process can be summarized as:

$$\text{SSSS} \rightarrow \text{solute clusters} \rightarrow \text{GP zones} \rightarrow \beta'' \rightarrow \beta', \text{A(U1)}, \text{B(U2)}, \text{C} \rightarrow \beta \qquad (3)$$

where GP zones is Guinier-Preston zones [78-80]. Although Mg has high solubility in Al, precipitation of Mg_2Si is thermodynamically favorable because Si has a limited solubility in Al and tends to form the Mg_2Si equilibrium phase [78]. As a result, according to the Al-Mg_2Si pseudo-binary phase diagram, Mg_2Si has limited solubility in the Al matrix. At elevated temperatures, thermal energy to facilitate Mg-Si solute clusters once Si precipitates out of the substitutional sites in the supersaturated solid solution (SSSS) [78, 79]. The solute clusters produce GP zones along the $<100>_{Al}$ direction of the Al matrix. Murayama and Hono noted that the Mg:Si ratio and number density of GP zones depend on the number of Si atoms available for formation of solute clusters [81]. With longer age

time, GP zones grow into a β″ phase before transforming into a metastable β′ all the while growing parallel to $<100>_{Al}$. The intermediate A, B, and C phases form as a byproduct with various stoichiometries of Mg-Si compounds, depending on the number of excess Si atoms available.

Finally, the plate-like β-Mg_2Si is produced with the broad surface on the $(001)_{Al}$-family planes. The phase transformation kinetics are summarized in **Figure 19**. The crystal structure of the Mg_2Si precipitate is face-centered cubic and forms a coherent interface with the surrounding matrix [78, 79, 82]. The orientation relationship between Mg_2Si and Al matrix is reported to be either $(001)_{\beta}//(001)_{Al}$ with $[110]_{\beta}//[100]_{Al}$ [83] or $(001)_{\beta}//(001)_{Al}$ with $[100]_{\beta}//[100]_{Al}$ [84]. Because of this strong connection to $<100>_{Al}$, the precipitate hardened matrix exhibits crisscross Widmanstätten patterns, as shown in **Figure 18a**.

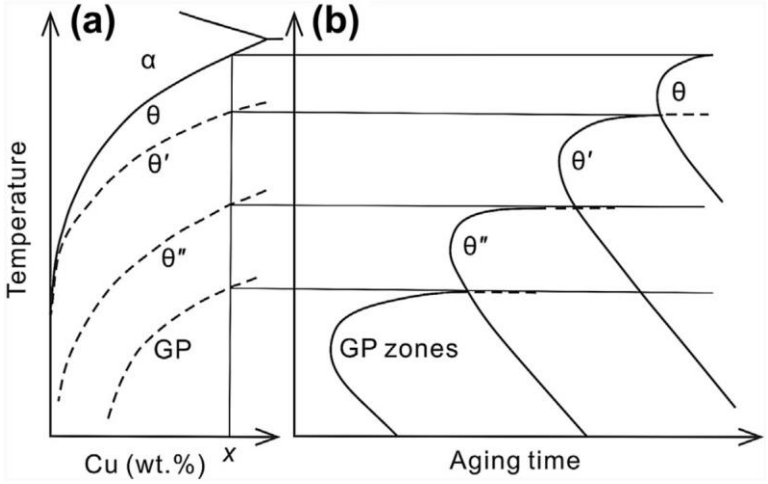

Figure 19. Time-temperature-transformation (TTT) diagram of various precipitation phases in binary Al-Cu [78]. The TTT diagram is applicable even when the intermediate phases (θ' and θ") and precipitate (θ) are replaced by their corresponding phases in β- Mg_2Si precipitation process. Adapted from Porter, D.A., Easterling, K.E., 1992. Phase Transformations in Metals and Alloy, 2nd Ed., Chapman & Hall, London. Reprinted with permission from Elsevier.

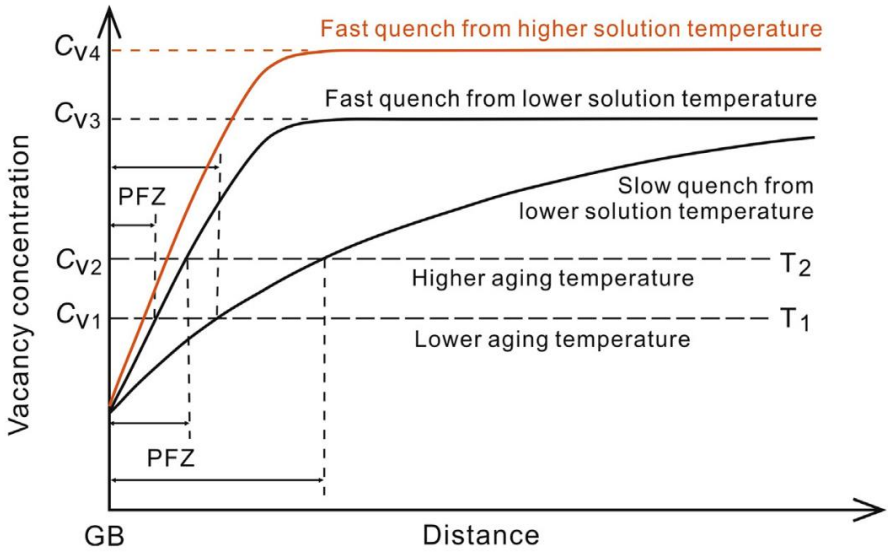

Figure 20. Effects of solution heat treatment temperature, quench rate, and aging temperature on the precipitate free zone width [78]. "GB" represents grain boundary. Reprinted with permission from Elsevier.

As shown in **Figure 18b**, precipitate free zones (PFZ) are areas around the grain boundary where Mg_2Si precipitates are absent [16]. This occurs due to either the lack of critical vacancy density to nucleate precipitates or the depletion of solutes near the grain boundaries as a result of grain boundary precipitation during cooling from solution heat treatment [78]. Critical vacancy supersaturation is necessary to nucleate precipitates, and many vacancies migrate to grain boundaries at elevated temperatures, resulting in PFZ around both sides of grain boundaries. Additionally, grain boundary inclusions have been observed in AA6451 with transmission electron microscopy, which may have been conducive to PFZ formation. Since dispersoids contain Si, it is also possible that small PFZ can exist around them as well. It was reported that the width of PFZ depends on the quench rate and precipitate size (**Figure 20**): faster quench rate produced finer precipitates with narrow PFZ, while a slow cooling rate produced coarse Mg_2Si and wider PFZ [78, 85].

2.3.3.2 Precipitation Hardened Matrix and Soft Precipitate Free Zone

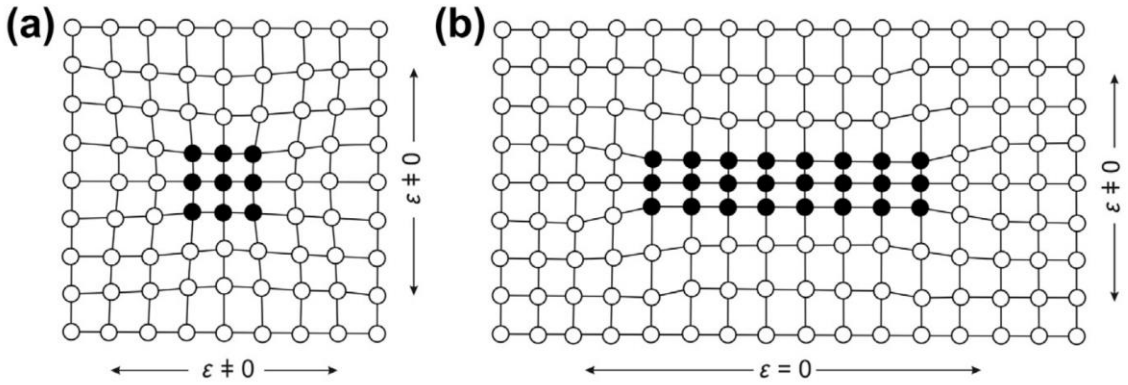

Figure 21. Misfit between coherent a) spherical and b) plate-like precipitates and its surrounding matrix [78]. Adapted from Porter, D.A., Easterling, K.E., 1992. Phase Transformations in Metals and Alloy, 2nd Ed., Chapman & Hall, London. Reprinted with permission from Elsevier.

Mg_2Si strengthens the matrix via precipitation hardening (or precipitation strengthening) [78]. Maintaining coherency at the particle-matrix interface requires local lattice distortion, as illustrated in **Figure 21b**. This induces elastic strain field around precipitates that can hinder dislocation movement through them. Additionally, from a thermodynamic perspective, shearing a particle involves increasing its surface area, which increases the activation energy for dislocation movement. Finally, the stiffer precipitates have higher modulus than the soft aluminum matrix, which makes shearing more difficult. As a result, Mg_2Si initially inhibit dislocation glide and facilitate dislocation accumulation. The combination of these factors contributes to the higher modulus, yield stress, and tensile strength of precipitate hardened T6 compared to those of T4, which does not contain strengthening precipitates.

However, precipitates are conducive to strain localization. Dowling and Martin noted that unlike the unshearable dispersoids, Mg_2Si precipitates are shearable due to the coherent interface with the Al matrix [11]. A precipitate is inevitably sheared when the accumulated dislocations exert sufficient strain, and the shear plane experiences local softening, where subsequent dislocations glide preferentially. This provides a slip plane where a narrow slip band can form to produce strain concentration leading to failure. As a result, precipitation hardened alloys without dispersoids showed higher strain concentration due to wide slip band spacing than those with dispersoids that produced evenly distributed slip bands. Budzakoska *et al*. noted that the submicron dimples (*e.g.* point A in **Figure 11c**) found on fracture surfaces suggest void nucleation at precipitates create secondary microcracks [59].

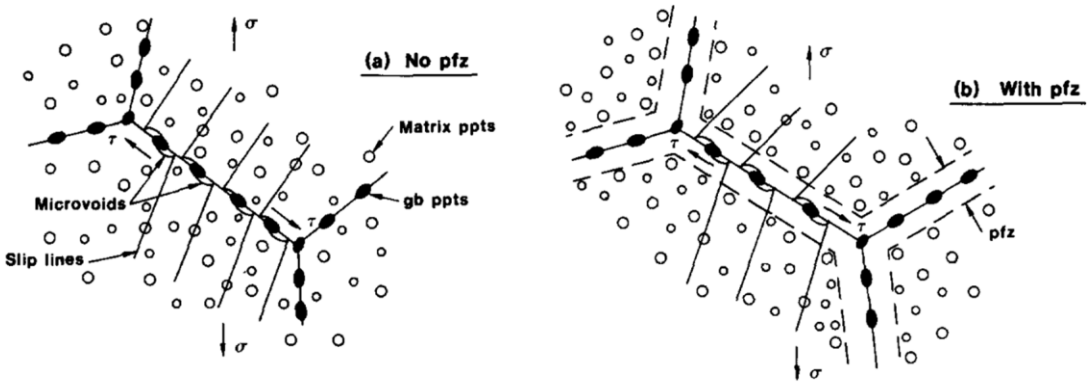

Figure 22. Illustration showing the deformation process of a precipitation hardened alloy a) without and b) with PFZ [86]. Reprinted with permission from Elsevier.

The PFZ can also significantly impact the mechanical behavior. As the name suggests, PFZ near grain boundaries are devoid of hardening precipitates and are therefore softer than the grain's precipitate hardened core. As a result, deformation is localized at the

softer PFZ than the strengthened matrix. As illustrated in **Figure 22**, for alloys with grain boundary precipitates where microvoids preferentially nucleate, those with PFZ nucleate voids at a lower applied strain than those without PFZ [86]. For these alloys, when intergranular fracture occurs, secondary cracks formed by growth of microvoids that coalesce with the primary crack, resulting in grain boundary ductile fracture. One method to resolve this problem is to use alloys with less impurities to reduce the number of grain boundary precipitates and PFZ to increase fracture resistance without compromising the yield strength [16].

CHAPTER 3. EXPERIMENTAL METHODS

The objective of this work is to study the effects of interactions between secondary particles—dispersoids, in particular—and their surrounding microstructure on the deformation behavior of aluminum alloys. To study these effects, two different loading conditions were used to induce plastic deformation: three-point bending with AA6451 and deep drawing with AA3xxx.

3.1 Sample Preparation

3.1.1 AA6451-T6 and -T4

AA6451 was produced in the same manner as described by Das, *et al.* in [87] by Novelis Inc. First, industrial-scale full-size AA6451 ingots were produced with three different Mn and Cr contents. The amount of alloying elements in composition A, which is the baseline control group, is described in **Table 1**. Composition B contains more Mn than A, and composition C has more Mn and Cr than A. "Alloy A", "Alloy B", and "Alloy C" will be used as shorthand for samples containing composition A, B, and C, respectively. Unless otherwise stated, all micrographs shown in the AA6451 chapter are from composition C. The ingots scalped, homogenized, hot rolled, cold rolled, and solution heat treated. AA6451-T4 was naturally aged while AA6451-T6 was artificially aged at 225 ± 3°C for 30 minutes. "T6" and "T4" will be used as shorthand for samples based on their aging conditions.

Table 1. Chemical composition of AA6451 in wt%. "+" indicates higher minor alloying element content than composition A.

	Si	Fe	Cu	Mn	Mg	Cr
A	0.60-1.0	0.20-0.30	0.10-0.25	0.05-0.20	0.40-0.80	0.01-0.10
B				+		
C				+		+

The bulk samples used for the three-point bend tests were 50 mm × 50 mm × 2 mm T6 and T4 sheets produced by Novelis Inc. The samples needed to be cut into smaller pieces in order to fit into an *in-situ* three-point bend test rig. The sheets were cut parallel to the rolling direction (RD) using wire electrical discharge machining and trimmed perpendicular to the RD using Struers Minitom to produce approximately 31 mm × 10 mm × 2 mm samples, where the 31-mm long edges were parallel to the RD.

The samples were mounted onto 1.25-inch diameter T6 cylindrical pucks with Ted Pella Inc. Crystalbond™ 590 for mechanical polishing. First, the pucks were heated on a hot plate set to 180°C, and the Crystalbond™ bar was chipped into small flakes using a razor blade and sprinkled on top of the heated pucks. Once the flakes melted, a sample was centered onto each puck by applying pressure with wooden Popsicle sticks. Once the samples were secure flat on the puck's top surface, the pucks were immediately removed from the hot plate to prevent changes to the microstructure and quenched in cold water.

Once the pucks were cooled to room temperature, they were loaded onto Struers RotoPol-15-RotoForce-1 and mechanically polished according to the conditions specified in **Table 2**. The samples were carefully separated from the pucks by melting the

Crystalbond™ at 180°C. The remaining Crystalbond™ was removed by soaking the samples in a methanol bath for 24 hours and washing off the methanol with ethanol. The samples were then electropolished using Struers LectroPol-5 cooled with PolyScience® MX07R-20L11B to -10°C. The polishing parameters are described in **Table 3**. The electrolyte for electropolishing was comprised 78 ml perchloric acid; 90 ml distilled water; 100 ml ethylene glycol monobutyl ether; and 730 ml ethanol.

Table 2. Conditions for mechanical polishing. (* adjusted as needed)

Abrasive	Struers Pad	Force (N)	Duration (minutes)
P1200	N/A	5	1
P2500	N/A	5	3.5*
P4000	N/A	10	5*
9 μm diamond paste	Dac	10	3*
3 μm diamond paste	Mol	10	5
1 μm diamond paste	Nap	10	3

Table 3. Conditions for electropolishing. (* adjusted as needed)

Parameter	Condition
Mode	Polishing Only
Temperature	External Cooling
Area	2 cm^2
Electrolyte	A2
Voltage	18 V
Flow rate	9
Duration (seconds)	20-30 seconds*

3.1.2 Jet polishing

Jet polishing was used to prepare T6 and T4 samples for two reasons: the former to measure the precipitate free zone (PFZ) and the latter to quantify the dispersoid density in the matrix as a function of compositional variation. 2 mm thick T6 and T4 sheets with three different compositions A, B, and C were received from Novelis Inc. The sheets were cut into smaller pieces using the Struers Minitom and secured onto AA6061 pucks.

The samples were then ground into thickness of less than 150 μm using progressively finer SiC paper (P800, P1200, P2500, and P4000) with 5 N loads. The thicknesses of the samples were verified with a caliper. 3-mm disc transmission electron microscopy (TEM) specimens were produced from the thinned samples using a disc puncher. The samples were jet polished using Struers TenuPol-5 set to 9 V with a 30% nitric acid, 70% methanol electrolyte cooled to -25°C with a methanol bath.

3.1.3 Ga-embrittlement

In order to quantify the dispersoid density at grain boundaries as a function of composition, T4 samples of compositions A, B, and C were embrittled with Ga to expose the dispersoids on grain boundaries. Ga was placed on a hot plate set to 40°C allowed to melt. After the Ga melted, a razor blade was used to scratch the surface of a sample to remove the oxide layer and expose fresh Al surface. Liquid Ga was immediately applied to the scratches with a wooden toothpick and excess Ga was removed with Kimwipe. After waiting for a few seconds, a razor blade was anchored to the scratch and hammered to

induce brittle fracture. The broken pieces of the sample were attached to SEM stubs using adhesive carbon tape to be analyzed in Hitachi SU8230 SEM.

3.1.4 AA3xxx

In order to observe the effects of dispersoids on the crack propagation behavior, three samples have been collected at various stages of the deep drawing process at Novelis Inc. The details of the processes that each sample underwent is shown in **Table 4**.

Table 4. AA3xxx sample conditions.

Sample Name	Condition
Ironed sample	Ironed after internal baking above 190°C for several minutes
Necked-1 sample	Approximately midway through the necking sequence
Necked-2 sample	After more than double the number of passes than necked-1

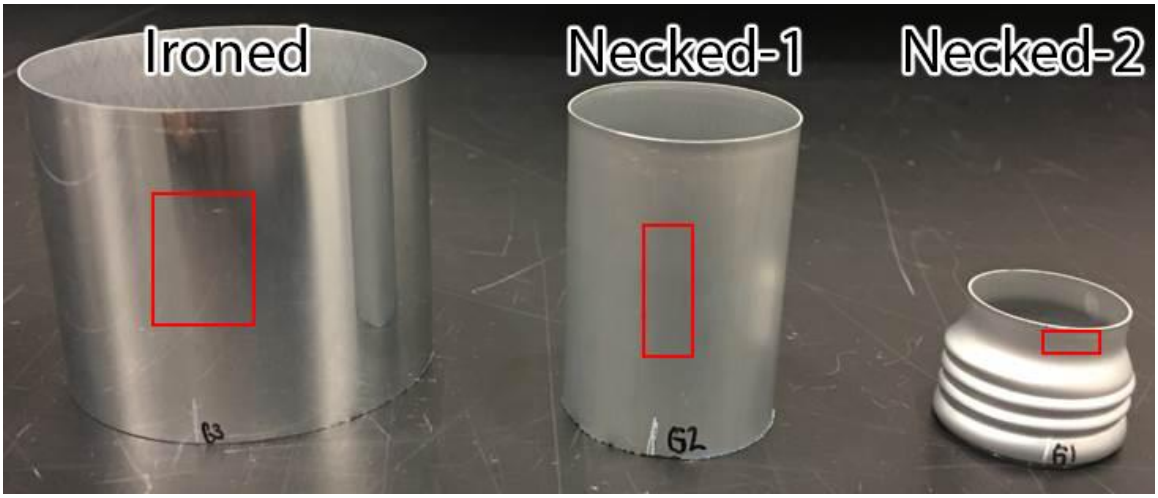

Figure 23. As-received AA3xxx samples. The red rectangles highlight regions of interest.

The as-received samples (**Figure 23**) were cut using metal shears to fit into a scanning electron microscope (SEM) chamber. The trimmed samples were then secured

onto scanning electron microscopy (SEM) stubs using Ted Pella Inc. Crystalbond™ in a similar manner as described in *Section 3.1.1*.

3.1.5 Focused Ion Beam TEM Specimen Preparation

After mechanical testing, focused ion beam (FIB) was used to prepare site-specific TEM specimens using FEI Nova Nanolab 200 FIB/SEM. The samples were secured onto SEM stubs with Crystalbond™ in the same manner as described in *Section 3.1.1*. The stub and a Cu Omniprobe® Lift-out TEM grid were secured onto a PELCO® 1" FIB Sample and Grid Holder (Ted Pella Inc. product number 15465) and loaded into the FIB/SEM chamber.

The various steps of the FIB lift-out process are outlined in **Figure 24**. Once a bulk sample and the TEM grid were loaded into the FIB/SEM chamber, the electron beam is set to acceleration voltage of 5 kV and beam current of 0.40 nA, and the ion beam is set to 30 kV and 30 pA. Once the sample achieved eucentric height and the electron beam correctly focused, region of interest (ROI) was found by moving the sample stage. Then the sample was tilted to 52° to check if the ion beam was correctly centered at the ROI. The ion beam current was increased to 5.0 nA before running "Runscript.exe", an automated FIB lift-out program. Because the script often runs into problems with focusing, the ion beam focus and stigmators were readjusted every time the beam current is changed. Furthermore, Runscript.exe was only be used for making trenches for the same reason.

Trench cuts were made by executing Runscript.exe with the following settings: 20 "finalwidth" (specimen width); 10 "finaldepth" (sample depth); and 3 "depositionz" (thickness of Pt layer) while keeping all the other preset parameters. The Runscript.exe will

make fiducial markers (**Figure 24a**), deposit a protective Pt layer (**Figure 24b**), and make trenches around the ROI (**Figure 24c**). Once the trenches are finished, Runscript.exe was manually aborted and a U-cut was made at 0° sample tilt using 0.30 nA ion beam current (**Figure 24d**). The lamella was then welded onto the Omniprobe needle with Pt deposition and the remaining connection with the bulk sample was severed. After lowering the Z-coordinate of the sample stage to move the bulk sample away from the lamella, the sample stage was moved in X- and Y-coordinates to transport the lamella to the TEM grid, where it was welded and separated from the needle. The sample was thinned to electron transparency by progressively lowering the ion beam acceleration voltage from 30 to 10 kV and tilting the sample between 50° and 54°.

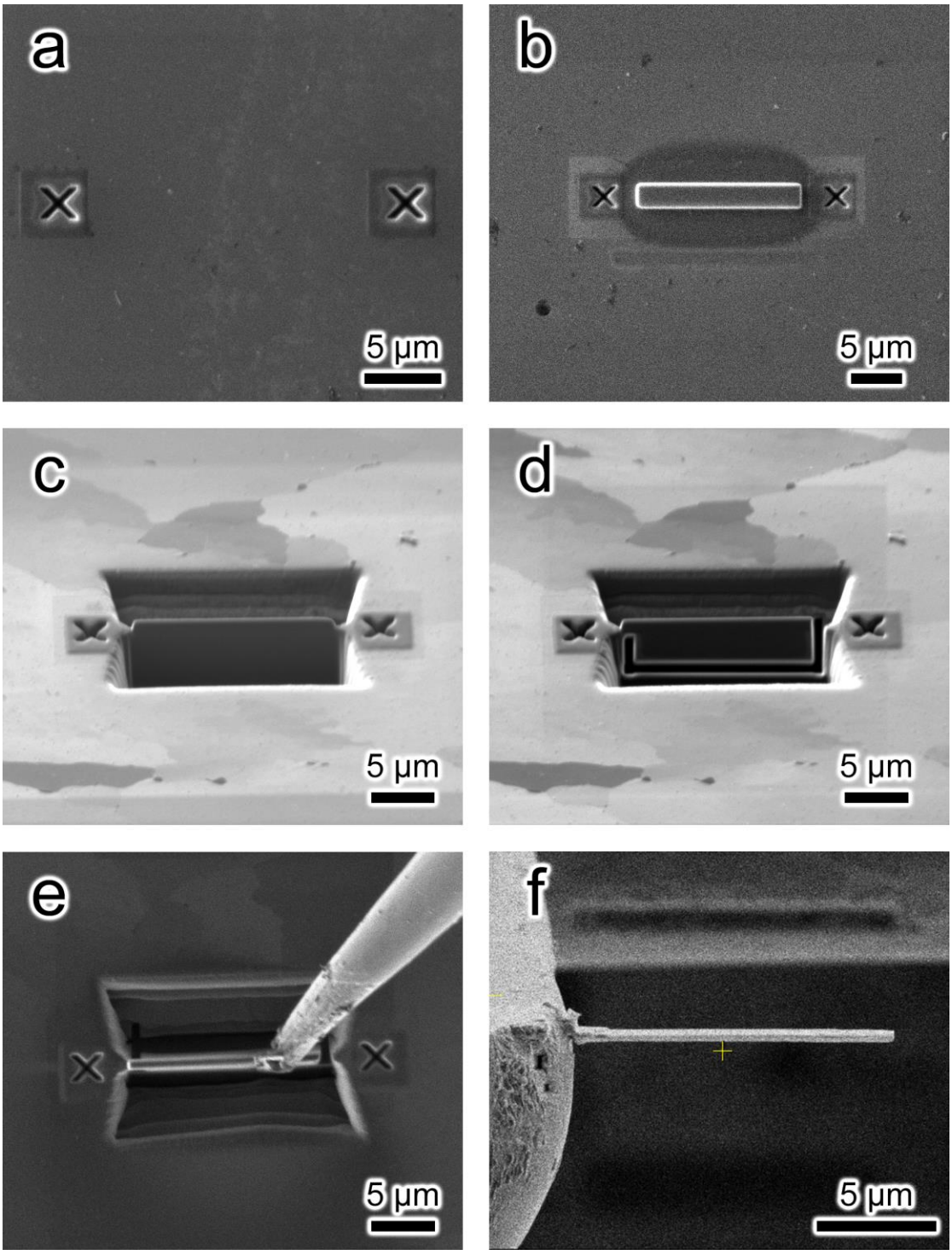

Figure 24. Ion beam (a-e) and electron beam (f) images showing the FIB lift-out process: a) fiducial marking; b) protective Pt layer deposition; c) trench cut; d) U-cut; e) attaching the lamella to an Omniprobe needle; and f) attaching the lamella to a TEM grid.

3.2 Mechanical Testing

The AA6451-T6 and -T4 samples were subjected to three-point bend tests to simulate the hemming process. Three-point bend testing was performed *ex-situ* using an *in-situ* SEM tensile stage, MTI Instruments 1000 lb Tensile Stage modified with a three-point bending fixture (**Figure 25**). The three-point bending fixture is set up so that two of the contact points are fixed in position while the load is placed via a movable pin with a bend radius of 1.6 mm. The two fixed contact points did not have a rounded surface and consequently scraped the sample as the load was applied, which may have affected the load measurement. The samples were loaded so that the polished surface was on the opposite side of the movable pin. The tensile stress experienced by the polished surface (front plane) was naturally oriented parallel to the RD of the sample.

All the three-point bend tests were displacement-controlled with a displacement rate of 0.02 mm/s—which is equivalent to a strain rate of 0.001 s^{-1}. During the preliminary tests for both T6 and T4 samples, load, displacement, and time were recorded while applying maximum displacement of 8 mm. More in-depth microscopy analyses were performed after applying 1 mm- or 3 mm-displacements on T6 and 8 mm-displacement on T4 samples. These displacement levels correspond to different levels of inner bend angles (**Figure 25**): 166° for 1 mm, 136° for 3 mm, and 90° for 8 mm displacements. The high ductility of the T4 variant required significantly higher displacement to show signs of crack initiation in the microstructure.

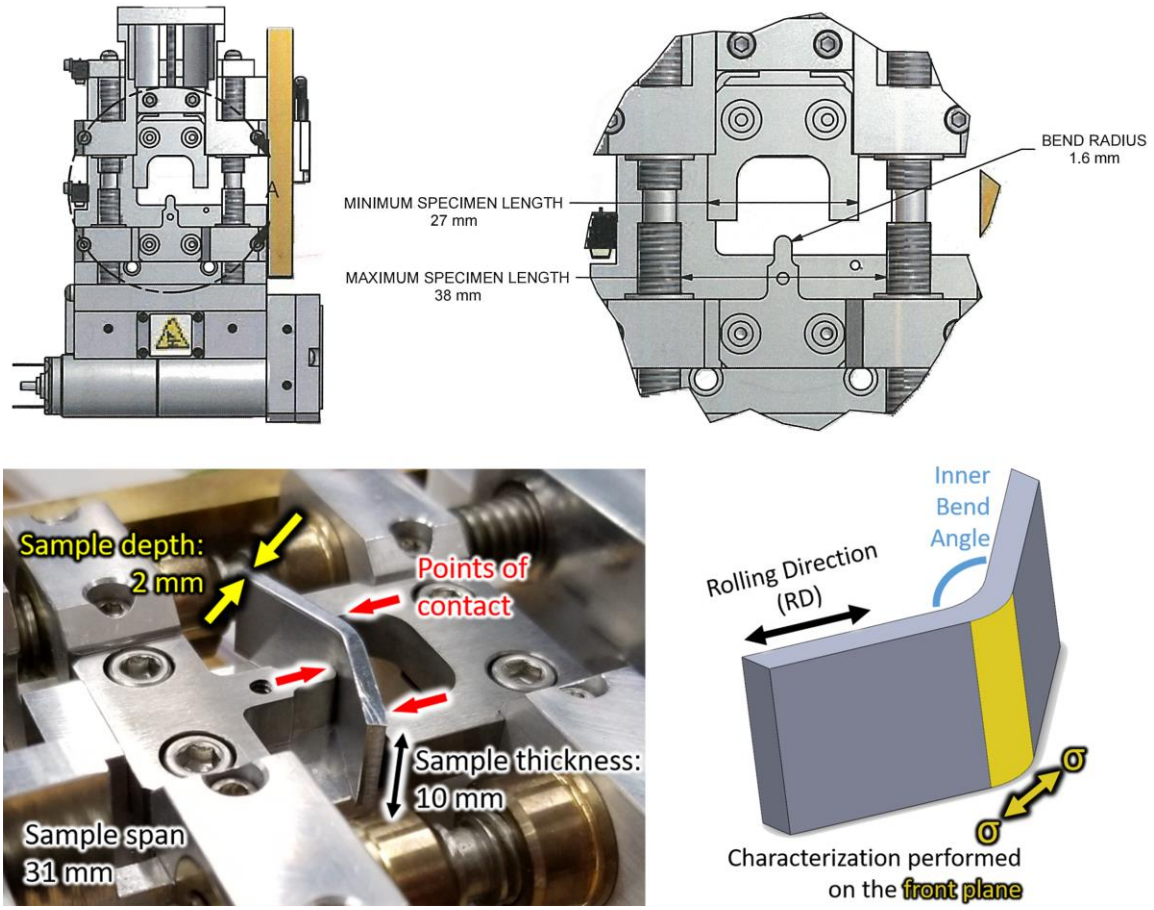

Figure 25. (Top) Schematic of MTI Instruments Tensile Stage with three-point bending fixture. The sample dimensions, sheet rolling direction (RD), and inner bend angles are shown in the bottom images.

3.3 Characterization Methods

Multiscale electron microscopy was used to characterize the microstructure of deformed alloys. Multiscale electron microscopy is a workflow that involves using various mesoscale and microscale microscopy techniques to characterize and quantify the effects of various microstructural defects on the deformation behavior. Mesoscale microscopy techniques employ SEM and electron backscatter diffraction (EBSD) to survey and analyze the samples to get a statistically representative understanding of the microstructure. In addition, it is used to identify key microstructural features of interest that are conducive to localized deformation behavior for a more in-depth study with microscale electron microscopy techniques. The microscale electron microscopy uses microscopes capable of characterizing the individual defect interactions with its surroundings. This involves TEM, STEM, and EBSD analysis on a small ROI. This latter set of technique aims to get a mechanistic understanding of how defects such as second phase particles and grain boundaries synergistically influence the deformation behavior of metals. The information from microscale analysis is then fed back into the mesoscale analysis to verify the findings and infer how microscale interactions manifest themselves as features on a larger length scale.

3.3.1 Scanning Electron Microscopy

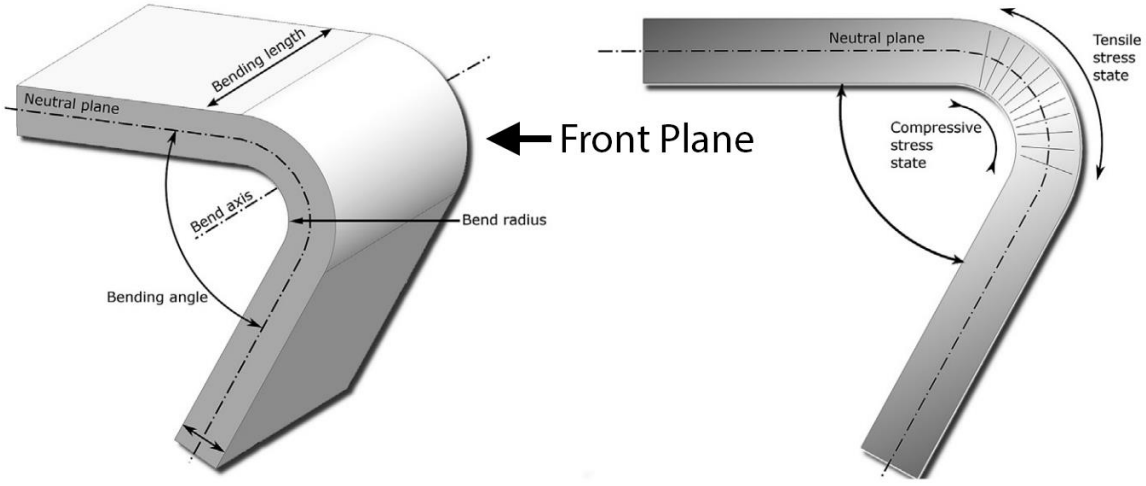

Figure 26. Sheet metal during a three-point bending test [34]. Reprinted with permission from Elsevier.

After securing them on stubs with Crystalbond™, the surfaces of deformed AA6451 and AA3xxx samples were studied with TESCAN MIRA3 SEM and Hitachi SU8230 SEM with acceleration voltage of 10 kV. For bend tested AA6451 samples, all the microscopy analyses were performed on the polished front planes of the samples, where they experienced the highest level of tensile stress, unless otherwise stated. The focus of this analysis was to identify artifacts of localized plastic strain (*i.e.* cracks and slip traces) and to examine the surrounding microstructure for possible correlations that may have facilitated the localized damage, since only when the features and regions of interest have been distinguished can site-specific analyses be performed.

3.3.1.1 Correcting for Grain Boundary Tilt for Measuring Grain Boundary Area

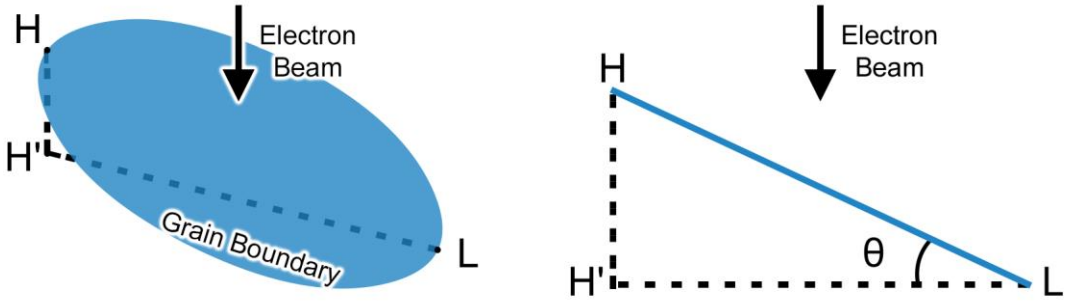

Figure 27. Schematic of a grain boundary from different points of view. Points H and L denote the closest and furthest points from the SEM pole piece, respectively: *i.e.* lowest and highest working distances, respectively.

SEM images of grain boundaries were used to measure the grain boundary dispersoid density in order to estimate the area of grain boundary surfaces, their areas in the SEM images must be corrected for their tilts. Grain boundaries are assumed to be planar without curvatures to simplify the approximation. The vertical distance between the highest (H) and lowest (L) points on the grain boundary (*i.e.* $\overline{HH'}$) are identified by adjusting the SEM focus and noting the changes in the working distance (WD). In the SEM image, the z-direction information is lost, and point H is displayed as point H'. The difference in z-coordinates between points H and L (*i.e.* length of $\overline{HH'}$) was measured by calculating the difference in WD when focusing on each point (ΔWD). Image J was used to measure the length of $\overline{H'L}$ in the SEM image. The grain boundary tilt (θ) can be calculated as:

$$\tan\theta = \frac{\Delta WD}{\overline{H'L}} \tag{4}$$

The area of the grain boundary (A') in the SEM image was measured by coloring it black on a transparent layer in Photoshop and counting the number of black pixels using MATLAB. The area of grain boundaries (A) were corrected for their tilts with the following formula:

$$A = \frac{A'}{\cos\theta} = A'\sqrt{1 + (\tan\theta)^2} \tag{5}$$

3.3.2 Cross-Section Analysis

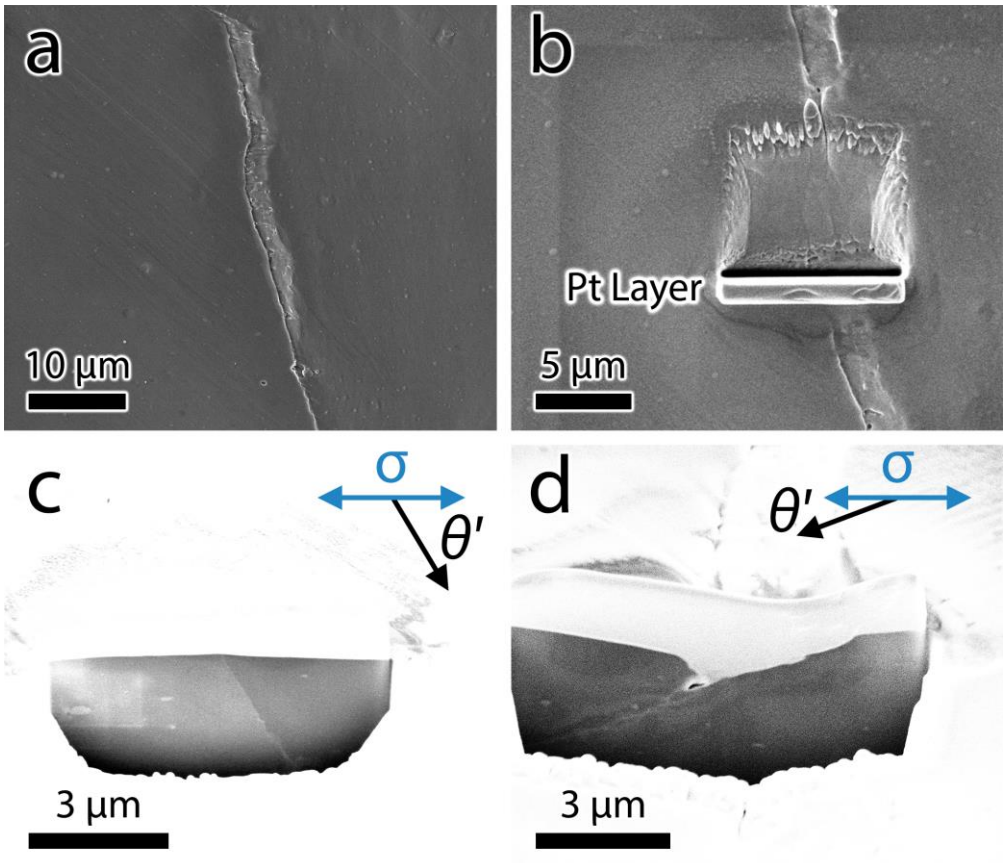

Figure 28. Cross-section procedure involving a) locating a region of interest and b) making a trench with the FIB. The angle between the grain boundary and the tensile load axis (blue arrows) is measured at 52° sample tilt.

Cross-section analysis was performed on the T6 samples after three-point bending to examine the influence of grain boundary orientation on their susceptibility to localized deformation. **Figure 28** shows the cross-section analysis procedure. FEI Nova Nanolab FIB/SEM was used for cross-sectioning and imaging. Fifteen grain boundaries with and without features of localized deformation were arbitrarily selected. The sample was rotated so that the tensile load direction was horizontal on the electron beam image when the sample stage is set at 0°. Once an ROI was identified, the stage was tilted to 52° and a protective Pt layer (~2 µm thick) was deposited to protect the subsurface microstructure and to prevent curtaining. Then a rectangular trench (~10 µm in length and ~5 µm deep) was made using the "cleaning cross-section" function of the ion beam at 30 kV and 3.0 nA to expose the grain boundary underneath the Pt layer. Then part of the Pt layer was also etched away at 0.5 nA to polish the exposed grain boundary. The cross-sections of the grain boundaries were imaged with the electron beam in "immersion mode" using various suction tube voltages with the thermoluminescent dosimeter at 52° sample tilt. The angle of the grain boundary orientation with respect to the horizontal loading axis (θ') was measured using ImageJ. The measured angle was corrected for sample tilt by using the following formula:

$$\theta = \tan^{-1}\left(\frac{\tan\theta'}{\sin 52°}\right) \tag{6}$$

Where the actual orientation of the grain boundary is represented with θ.

3.3.3 Electron Backscatter Diffraction and Transmission Kikuchi Diffraction

Electron backscatter diffraction (EBSD) is a versatile characterization technique that can quickly survey the mesoscale microstructure and thoroughly probe the microscale dislocation structures. When an electron beam in an SEM is concentrated onto a surface of a crystalline sample, the electrons that interact with the lattices in a way that satisfies the Bragg's law produce backscattered electrons whose constructive interference manifests itself as bands of high intensity signals on electron backscatter patterns (EBSP), called Kikuchi bands. Identifying which crystallographic plane is represented by each Kikuchi band is called indexing, and the information it carries can elucidate many aspects about the crystallographic and strain state of the probed region of the sample surface: from the phase and the crystallographic orientation to the elastic strain and dislocation density. Collection of EBSP over a large enough area will yield a useful information such as grain boundary maps, pole figure maps, and kernel average misorientation maps. The local texture and the speed at which this information can be collected makes EBSD an extremely powerful and useful tool for microstructural characterization.

One of the biggest limitations of this technique is that the quality of EBSP and therefore the reliability of the data is heavily dependent on time-consuming sample preparation. Abrasives that are used to polish the samples damage and distort the crystal lattice near the sample surface, thereby lowering the pattern quality. Soft metals such as Al are much more susceptible to damage than most commercial alloys, which is why electropolishing after mechanical polishing is a requirement for EBSD sample preparation. The wealth of information, however, and the speed of the microstructural survey outweighs

the labor cost, making EBSD a standard characterization tool for a wide variety of industries and laboratories.

In order to look for any microstructural differences that may arise from compositional differences, EBSD scans were performed on undeformed AA6451-T4 for compositions A, B, and C, previously mentioned in *Section 3.1.2*. The samples were secured on a 70° pre-tilt so that the RD is horizontal in the EBSD scans. The scans were performed using the TESCAN MIRA3 SEM with EDAX Hikari EBSD detector, with acceleration voltage of 20 kV.

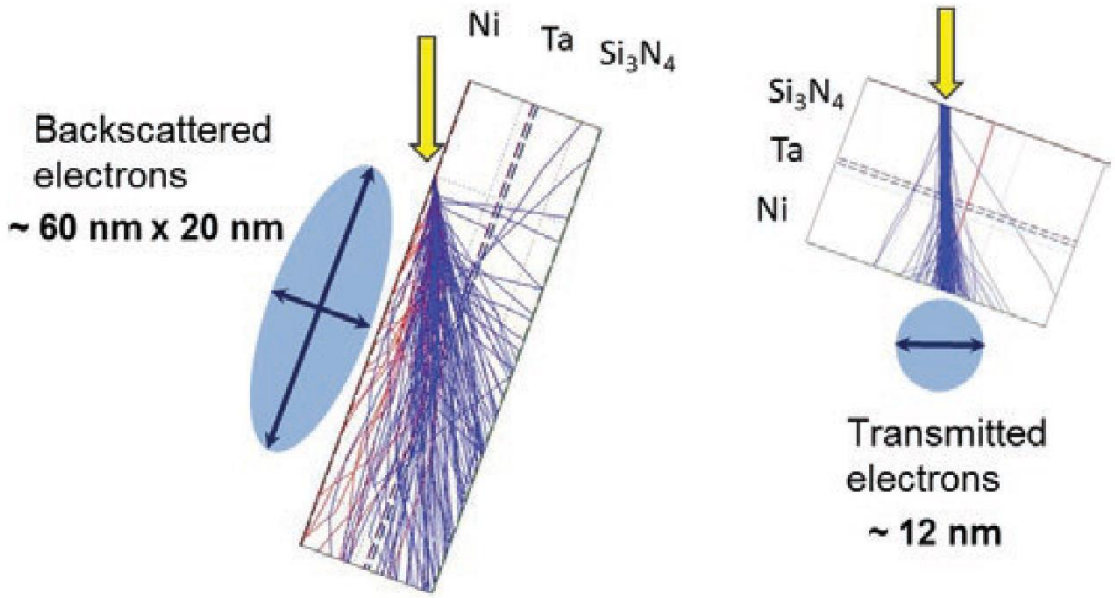

Figure 29 Monte Carlo simulations of electron scattering trajectories in an 82.5 nm-thick specimen at beam energy of 28 keV [88]. The red lines indicate the electrons that backscattered out to the incident beam entrance surface. The interaction volume in TKD configuration (right) is significantly smaller than that of conventional EBSD (left). Reprinted with permission from Cambridge University Press.

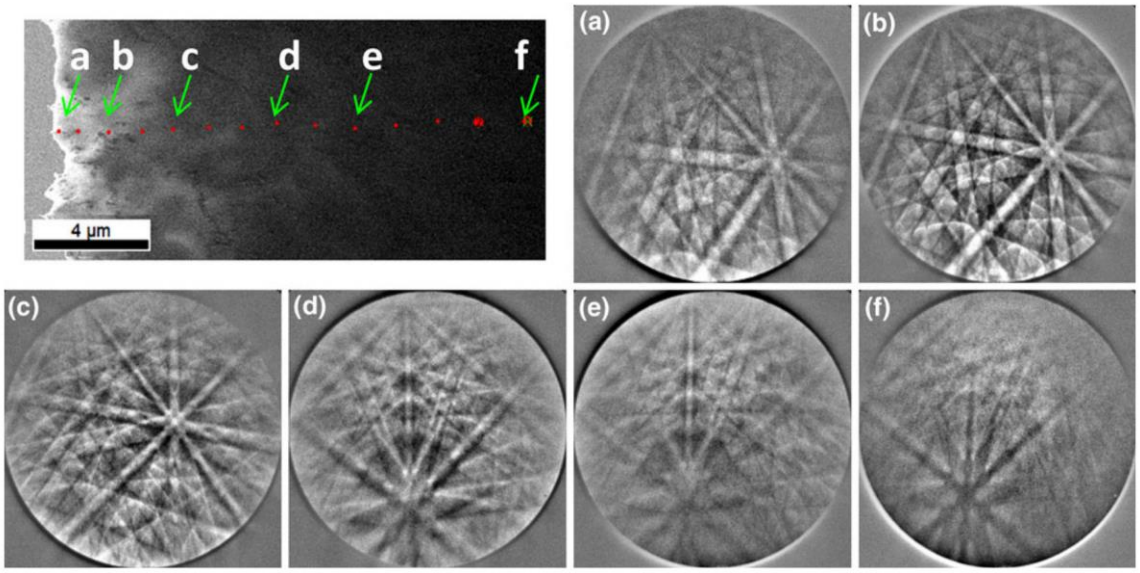

Figure 30. TKD pattern quality as a function of specimen thickness [89]. Copyright 2013 reprinted with permission from Springer Nature.

Transmission Kikuchi diffraction (TKD) is a relatively new method of collecting diffraction patterns by collecting forward scattered electrons that have transmitted through a thin specimen, such as jet polished and FIB lift-out specimens. With conventional EBSD, it can be difficult to obtain high quality EBSP when the sample dimension is considerably smaller than the backscattered electron interaction volume for bulk materials since there may be insufficient number of detectable backscattered electrons to carry crystallographic information (note the scarcity of red backscattered electrons in **Figure 29**, left) [90, 91]. In contrast, TKD utilizes forward scattered electrons (blue lines in **Figure 29**, right) whose coherency is a result of scattering events in the specimen leading to signals with better contrast in the diffraction patterns [90]. Furthermore, it has been shown that the significantly smaller interaction volume (**Figure 29**) and the narrower spread of transmitted electron energy in TKD compared to that of backscattered electrons in conventional EBSD

is indicative of fewer scattering events and thereby reducing the lateral spread of the electron beam, conducive to improved spatial resolution of TKD [90, 92-94]. As a tradeoff for enhanced spatial resolution, the TKD pattern quality depends greatly on the specimen thickness (**Figure 30**) [89, 95]. If the sample is too thick, electrons lose their energy from inelastic collision with the sample and blurs the patterns. Spatial resolution may also decrease when the beam broadens from the increased interaction volume from dynamic scattering. For Al, although indexable TKD patterns have been collected from a sample as thick as 3 μm [96], patterns of the highest quality were collected when the thickness was between 75 and 200 nm [97]. Since its inception, TKD has been used to study ultrafine grains [97-101]; nano-sized secondary phases [92]; and twin boundaries in atom probe tomography samples [102].

To capitalize on its improved spatial resolution over traditional EBSD, TKD was employed to characterize the microstructure of FIB lift-out specimens from bend tested AA6451 and deep drawn AA3xxx samples. The TKD configuration requires that the specimen be positioned nearly flat (foil plane normal parallel to the optical axis) and as close to the pole piece as possible without touching it. In order to achieve this, one side the sample holder—PELCO® Small FIB Grid Holder (Ted Pella Inc. product number 15464)—was ground down using P300 SiC paper. The samples were secured with the holder and loaded into the TESCAN MIRA3 SEM on a 45° pre-tilt. The stage was tilted additional 45° to position the lift-out specimen flat and moved as close to the pole piece as possible before closing the chamber. After the chamber achieved operating pressure, the position of

the specimen was adjusted so that the WD is approximately 5-6 mm. The SEM was set to 30 kV and 25 kV for AA6451 and AA3xxx specimens, respectively.

All the EBSD and TKD data were cleaned on the OIM Analysis software using Grain CI Standardization (10° tolerance angle and minimum grain size of 5) and filtering out points with confidence index less than 0.1. All the inverse pole figure (IPF) maps shown in the following chapters are [001] IPF maps.

3.3.4 Dictionary Approach

One way to overcome the limitation of conventional EBSD technique mentioned in *Section 3.3.3* is using the dictionary approach to index the Kikuchi patterns. The traditional Hough-based method utilizes Hough transforms of EBSP to identify and index Kikuchi bands. The challenge that a highly deformed sample presents for EBSD is that the Kikuchi bands are smeared and distorted to the point where indexing via Hough transformation is no longer reliable. The dictionary approach tries to overcome this problem by simulating a dictionary of EBSP of a given material using a physics-based model [103] and comparing it to the collected patterns using a pattern similarity metric. For the AA3xxx study, the dot product between normalized patterns was used to determine the matching patterns. The dictionary is computed for a uniform sampling of orientation space [104], and the crystallographic orientation of the electron beam location is determined by the best matching pattern in the dictionary. The method is the EBSD analog of searching for the best possible word to the definition in a dictionary, hence its name.

The deep drawn AA3xxx samples were plastically deformed to the point where the Hough-based method failed to index many data points, especially those around grain boundaries where deformation was more localized. The collaborators, Professor Marc De Graef and Dr. Saransh Singh at Carnegie Mellon University, analyzed the AA3xxx EBSD data using the dictionary approach to index many of the missing data points. Their contribution was instrumental in characterizing dispersoid effects in crack propagation behavior in AA3xxx.

3.3.5 Scanning Transmission Electron Microscopy

Transmission electron microscopy (TEM) and scanning transmission electron microscopy (STEM) were used to study microstructural features whose sizes are too small to be resolved by other characterization means. More specifically, they were used to analyze dispersoid density, dislocation structures, and grain refinement. The dislocation imaging conditions required both α- and β-tilts to align the diffraction spots into two beam conditions. Therefore, the TEM specimen were loaded into FEI double tilt sample holder before performing STEM analysis using FEI Tecnai F30 TEM with 300 kV acceleration voltage. For bright field (BF) and dark field (DF) TEM imaging, α and β were adjusted to obtain two beam conditions. For annular dark field (ADF) and BF STEM images, camera lengths of 250 and 2000 mm were used, respectively, unless otherwise stated.

3.3.6 MATLAB Image Processing

Approximately 40 STEM images were taken for each AA6451-T4 composition (A, B, and C from *Section 3.1.2*) to measure the dispersoid number density (μm^{-2}) in the matrix. To expedite the analysis, a MATLAB code was written to process large numbers of STEM images.

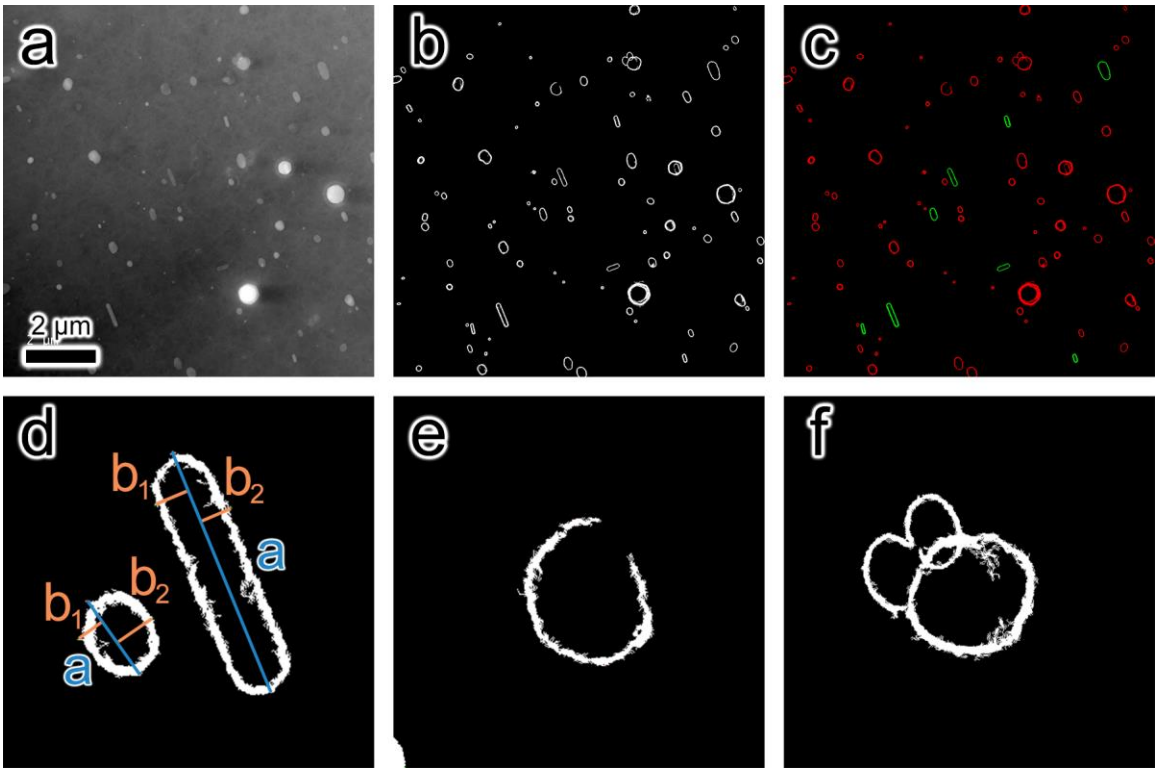

Figure 31. a) Original ADF STEM image; b) outlines of detected dispersoids; and c) color-coded outlines based on the aspect ratio. d) Major and minor axes used to calculate the aspect ratio; e) a dispersoid with an open outline; and f) outlines of overlapped dispersoids.

The code not only accounts for the α- and β-tilts, but also reduces noise and excludes features that may not be dispersoids. The noise in the original image (**Figure 31a**) is suppressed using a Gaussian filter. The outlines of the dispersoids are highlighted by

calculating the difference in grayscale values of each pixel with its first-order neighbors (gradient filter). As shown in **Figure 31d**, the diameter (a) is determined based on the furthest two points on each outline and the minor axes (b_1 and b_2) are calculated based on two furthest points on either side of the diameter line. The features on the image are filtered based on size: those with a diameter greater than 1 μm or less than a certain size are ruled out as constituents or noise, respectively. The remaining features that have open outlines (**Figure 31e**) are excluded as well unless the gap is small enough—usually less than 60° from the centroid—to approximate the diameter. The features are then filtered again based on their sizes, and the final product (**Figure 31b**) contains the outlines of dispersoids. Based on the aspect ratio (AR), each outline is classified as either a spherical or cylindrical dispersoid.

$$AR = \frac{a}{b_1 + b_2} \tag{7}$$

Because the code did not produce consistent results when using fixed critical filter values, they were manually customized for each image to produce the most faithful representation of dispersoids in the original image.

Although the code saved days, if not weeks, of labor, the code has some drawbacks. Due to the nature of STEM images, some particles overlap, and their outlines are counted as one feature because of the contiguity of the outlines. This also affects the diameter and aspect ratio calculations, but these features constitute a very small fraction of dispersoids, and some of them were excluded from the analysis by size filtering. There remains a bigger

challenge of identifying dispersoids whose grayscale values blend well with the surrounding matrix. Automated image processing is a necessity for statistical analyses of microstructures, and this code is a prototype for future characterization toolsets.

CHAPTER 4. DISPERSOID AND MICROSTRUCTURE EFFECTS ON CRACK INITIATION PROCESS OF AA6451-T6 AND -T4 DURING THREE-POINT BENDING

4.1 Introduction

The objective of this study is to investigate the effects of dispersoids on the deformation behavior and crack initiation mechanism of AA6451-T6 and -T4 during three-point bend tests. AA6451 is commonly used for automotive body panel applications—hood outers, door panels, and fenders—for its light density and excellent formability [1]. The aluminum parts are joined to structural steel components by hemming, a method of joining two thin metal parts by wrapping one over and around the other (**Figure 32a**). Because of the loading configuration, this study will focus on three-point bending to emulate the loading condition during hemming. Although hemming is an attractive method because of its simplicity and low cost, it is unfortunately limited by the aluminum's capability to withstand high plastic deformation, a property known as "bendability".

While there are many defects that arise from the suboptimal processing parameters (*Section 2.1.2*), the cracking in the outer plane (**Figure 5** and **Figure 32c**) requires aluminum with improved bendability, which is a material-related challenge. Therefore, it is important to understand the structure-property relationships that arise from the complex AA6451 microstructure and how different microstructural defects interact during failure initiation processes to design more ductile and resilient aluminum alloys.

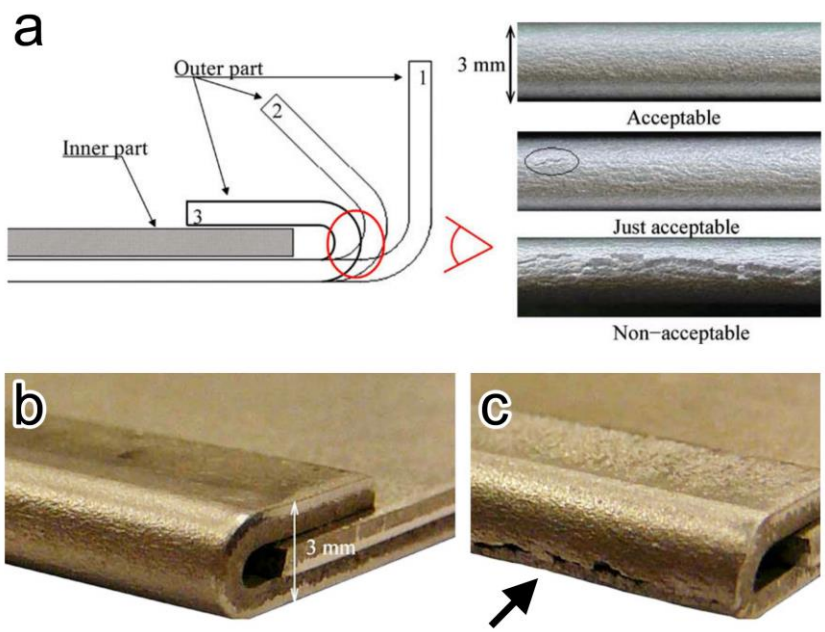

Figure 32. a) Schematic of the hemming process involving 1) flanging, 2) pre-hemming, and 3) hemming [14]. The images on the right show varying degrees of damage evolution resulting in orange peel (top), localized (middle) and macroscopic cracking (bottom). The red eye indicates the point of view. Examples of b) successful and c) defective hemming are also shown, with black arrow highlighting a macrocrack visible to the naked eye. Reprinted with permission from Elsevier.

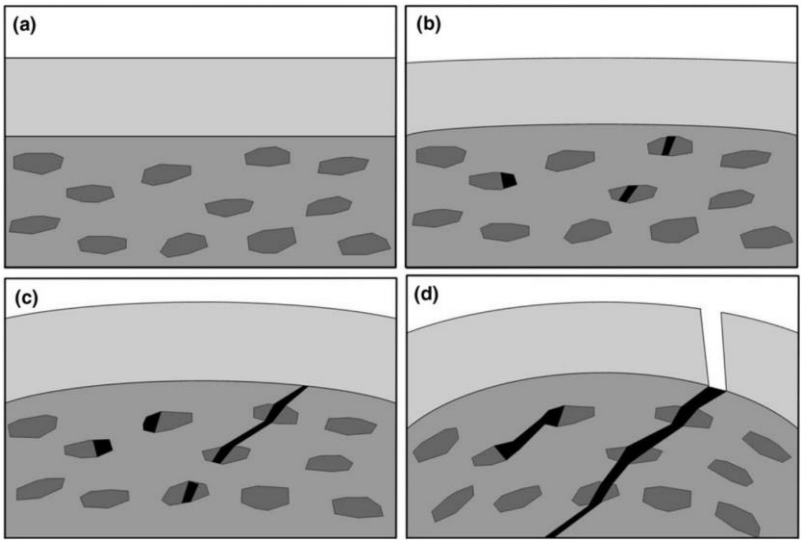

Figure 33. Schematic of shear localization leading to intermetallic particle cracking and coalescence into a microcrack [105]. Reprinted with permission from Springer Nature.

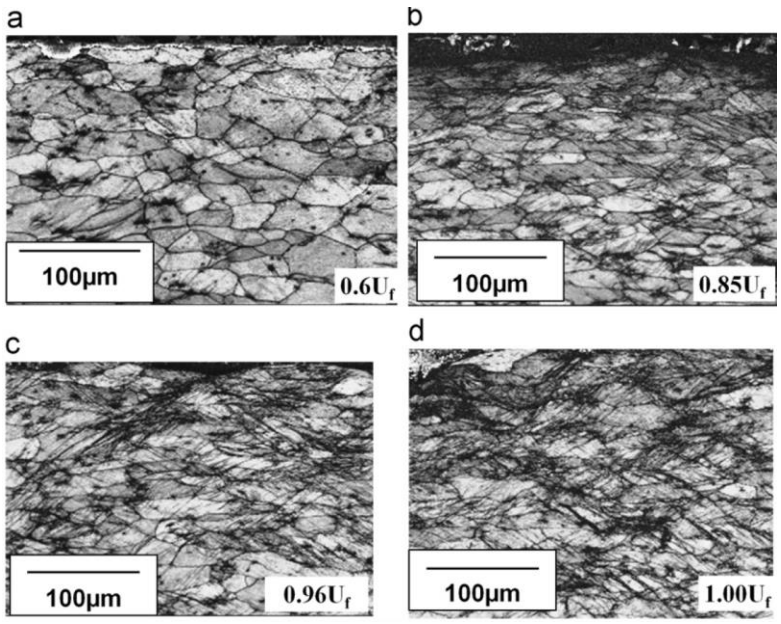

Figure 34. Evolution of shear bands via strain localization at various levels of displacement (normalized by critical displacement) [106]. Reprinted with permission from Elsevier.

Previous studies on failure of aluminum during three-point bending identified intermetallic particle cracking resulting from shear localization as a likely source of crack nucleation (**Figure 33**) [105, 107, 108]. The rationale is very similar to particle-driven void nucleation-growth-coalescence process described in Subsection 2.3.1.2, where dislocation accumulation around intermetallic particles induce particle cracking when critical strain is achieved. There have been reports of different crack initiation mechanisms: Davidkov *et al*. found that high concentration of Mg_2Si and $Al_{1.9}CuMg_{4.1}Si_{3.3}$ (Q-phase) at grain boundaries reduced the bendability considerably by promoting microvoid nucleation and facilitating ductile intergranular fracture in age hardened AA6016 [109]. Lloyd *et al.* concluded that cracks may be nucleated at the surface, where shear bands produce surface roughness that serve as stress concentrations [110]. Similarly, Mattei *et al*. observed that strain localization produces shear bands that neck selective surface grains and facilitate

intergranular ductile fracture in naturally aged AA6016 [106]. These different phenomena arise from variations in microstructure and show that understanding the effects of microstructural defects are needed.

One way to improve the bendability of aluminum and mitigate problems from strain localization is by controlling dispersoids, second phase particles can homogenize strain and reduce strain localization [7, 9-11]. Previous studies noted that the increase in ductility of dispersoid-containing alloys is attributed to the delay in dislocation structure evolution that accompanies failure initiation. In one study, Das *et al*. observed that increase in dispersoid number density correlated with a significant increase in bendability without noticeable compromise in tensile strength, yield strength, and ductility [87]. However, the micromechanical processes of how dispersoids affect the crack initiation process and the dislocation structure evolution during three-point bending is still not yet fully understood.

In this chapter, AA6451-T6 and -T4 samples were subjected to three-point bend tests to simulate hemming. Multiscale electron microscopy-approach involving SEM, EBSD, TKD, TEM and STEM was employed to study the crack initiation mechanism and to study the effects of dispersoids on the localized deformation behavior. Mesoscale electron microscopy was used to study the microstructure for features leading to crack initiation and grain boundary character facilitating localized deformation. Microscale characterization was performed to conduct in-depth investigations into the defect interactions and dislocation structures that develop during crack initiation. In addition, composition effects on the texture, PFZ size, and dispersoid density were explored.

4.2 Experimental Procedures

Industrial-scale AA6451 ingots with three different compositions were produced by Novelis Inc. to change the dispersoid density in the matrix. Composition A contained alloying elements specified in **Table 1**, serving as the control group. Composition B contained more Mn than A, and C contained more Mn and Cr than A. The ingots were scalped, homogenized, hot rolled, cold rolled, and solution heat treated. AA6451-T4 was naturally aged while AA6451-T6 was artificially aged at 225 ± 3 °C for 30 minutes. In the end, 50 mm × 50 mm × 2 mm sheets were produced by Novelis Inc. The samples were then cut with wire EDM and trimmed with Struers Minitom to produce 31 mm × 10 mm × 2 mm samples, where the 31-mm long edges were parallel to the rolling direction (RD).

Samples were mechanically polished with progressively finer SiC paper and diamond paste with Struers RotoPol-15-RotoForce-1 setup. They were then electropolished with Struers LectroPol-5 using a perchloric-ethanol based electrolyte.

A preliminary microstructure characterization was performed on the undeformed T6 and T4 samples of all compositions. Large electron backscatter diffraction (EBSD) scans were taken with TESCAN MIRA3 scanning electron microscope (SEM) set to 20 kV acceleration voltage and EDAX Hikari EBSD detector to study the texture and grain size differences. Bright field (BF) transmission electron microscopy (TEM) images of jet polished AA6451-T6 TEM specimens were taken with FEI Tecnai F30 TEM with 300 kV acceleration voltage to measure the widths of precipitate free zones (PFZ). To measure the dispersoid density in the matrix, annular dark field (ADF) scanning electron microscopy

(STEM) images of jet polished AA6451-T4 TEM specimens were taken with the same instrument and analyzed using the image processing MATLAB script. For measuring the dispersoid density on grain boundaries, SEM images of Ga-embrittled AA6451-T4 were taken with Hitachi SU8230 SEM at 10 kV acceleration voltage. Only AA6451-T4 was used to measure the dispersoid densities to avoid errors from counting Mg_2Si in AA6451-T6.

Three-point bend tests were performed on polished AA6451-T6 and -T4 samples using MTI Instruments 1000 lb Tensile Stage modified with a three-point bending fixture. The experiments were displacement controlled with displacement rate of 0.02 mm/s, which is equivalent to a strain rate of 0.001 s^{-1} on the front plane where the tensile stress is the highest. For AA6451-T6, the bulk samples were loaded up to 1 or 3 mm, while 8 mm—the maximum displacement—was applied to induce plastic deformation in AA6451-T4.

All characterization was performed on the front plane of the bend-tested samples. Preliminary characterization of the undeformed samples were performed using EBSD for texture and grain size; TEM for PFZ width; STEM for matrix dispersoid density; and SEM for grain boundary dispersoid density analyses. After deformation, surface characterization was performed using SEM with 10 kV acceleration voltage. EBSD scans of the deformed AA6451-T6 were collected using 20 kV acceleration voltage with EDAX Hikari EBSD detector to investigate the relationship between grain boundary misorientation angle and deformation features. Cross-section analysis of grain boundaries in AA6451-T6 was performed using FEI Nova Nanolab 200 FIB/SEM to study the effects of grain boundary orientation on the formation deformation features. Once ROI were identified from the mesoscale characterization, FEI Nova Nanolab 200 FIB/SEM was used to prepare TEM

specimens. Microscale characterization employed TEM and STEM characterization using FEI Tecnai F30 TEM with 300 kV. BF and dark field (DF) TEM images were taken by tilting the α and β to two beam conditions. Unless otherwise stated, camera lengths of 250 and 2000 mm were used to take ADF and BF STEM images, respectively.

More specific details can be found in the following sections: *3.1.1 AA6451-T6 and -T4*; *3.1.2 Jet polishing*; *3.1.3 Ga-embrittlement*; *3.1.5 Focused Ion Beam* ; *3.2 Mechanical Testing; 3.3.1 Scanning Electron Microscopy*; *3.3.2 Cross-Section Analysis*; *3.3.3 Electron Backscatter Diffraction and Transmission Kikuchi Diffraction*; *3.3.5 Scanning Transmission Electron Microscopy*; and *3.3.6 MATLAB Image Processing*. For reference, tensile properties of AA6451-T6 and -T4 are given in **Table 5** and **Table 6**.

Table 5. Mechanical properties of AA6451-T6. The orientation of the rolling direction (RD) with respect to the tensile loading axis is indicated in the second column. The acronyms are as follows: yield strength (YS); ultimate tensile strength (UTS); uniform elongation (UE); total elongation (TE); Young's modulus (E).

Composition	Load Axis vs RD	YS (MPa)	UTS (MPa)	UE (%)	TE (%)	E (GPa)
A	0°	271.24	295.53	7.85	12.88	59.94
	90°	267.46	294.42	7.95	12.42	58.42
B	0°	275.80	298.25	7.58	12.52	58.86
	90°	271.59	297.26	8.00	12.57	58.82
C	0°	269.59	292.61	7.57	12.33	56.66
	90°	264.64	290.33	7.84	12.89	57.77

Table 6. Mechanical properties of AA6451-T4. The orientation of the rolling direction (RD) with respect to the tensile loading axis is indicated in the second column. The acronyms are as follows: yield strength (YS); ultimate tensile strength (UTS); uniform elongation (UE); total elongation (TE); Young's modulus (E).

Composition	Load Axis vs RD	YS (MPa)	UTS (MPa)	UE (%)	TE (%)	E (GPa)
A	0°	147.68	252.24	19.93	25.07	55.51
	90°	142.87	248.25	20.75	26.09	58.45
B	0°	143.05	248.79	20.02	24.47	62.68
	90°	138.55	244.68	20.53	26.09	61.58
C	0°	141.94	246.99	19.75	24.25	60.41
	90°	137.44	240.99	19.56	24.98	57.13

4.3 Results

The sample variable matrix contains two tempers (T6 and T4) and three compositions (A, B, and C). The results for both T6 and T4 will be shown in tandem in each subsection, one after another for better comparisons. AA6451-T6 and -T4 will be respectively referred to as "T6" and "T4", and samples with compositions A, B, and C will be mentioned as "Alloy A", "Alloy B", and "Alloy C", respectively. Unless otherwise mentioned in the figure captions, the microscopy images will show images taken from Alloy C. The influence of Mn and Cr content will only be presented in *Section 4.3.1*, and every microscopy image shown after *Section 4.3.1* are taken from samples with composition C, unless otherwise mentioned.

4.3.1 Microstructure Variation from Composition Difference

4.3.1.1 Texture Variation

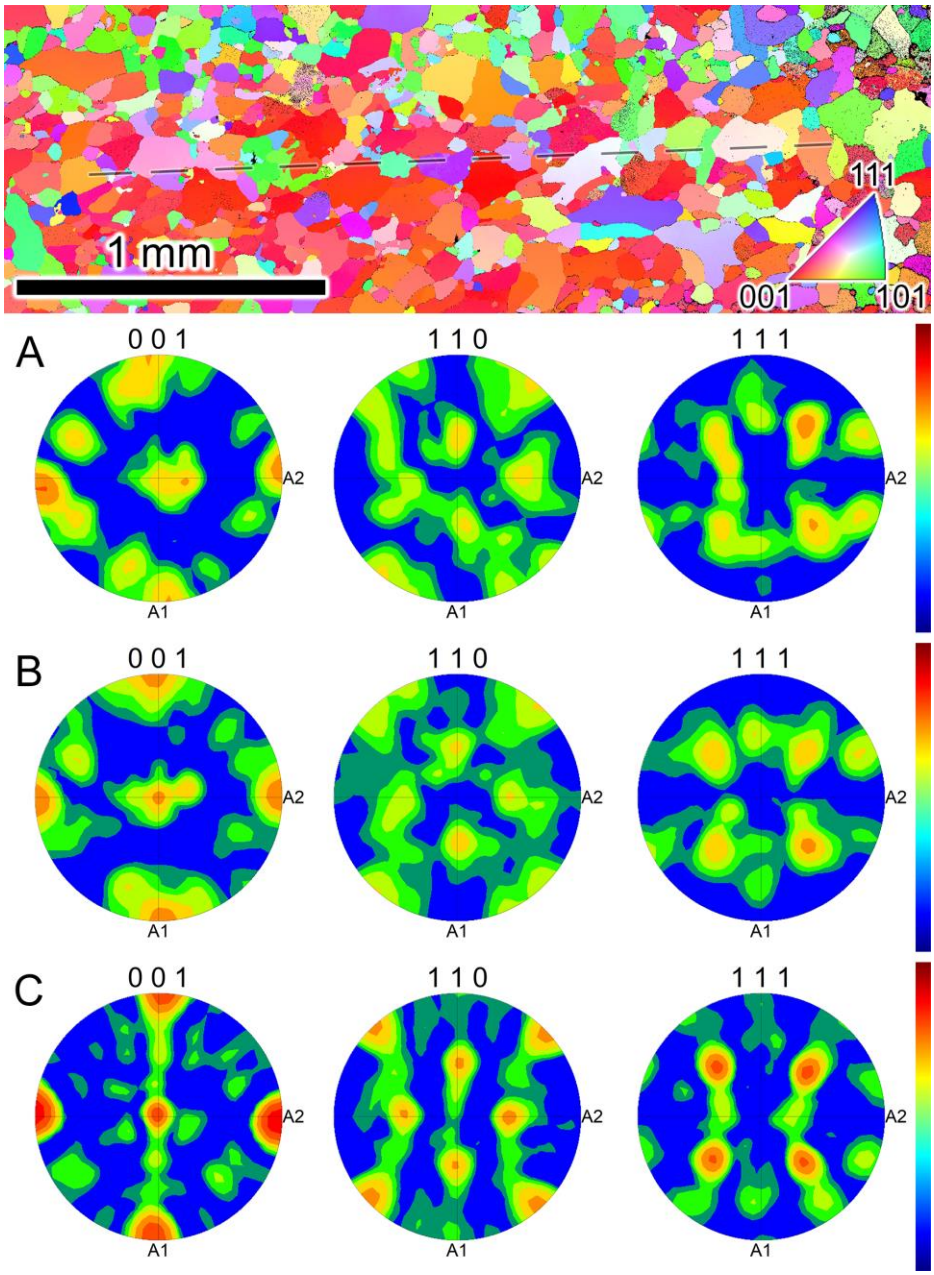

Figure 35. (Top) An IPF map generated from an EBSD scan on a T6 sample with composition C. The faint dashed line shows a boundary between areas with a strong <001> texture and a random texture. Color legend is in logarithmic scale 1-10 times random.

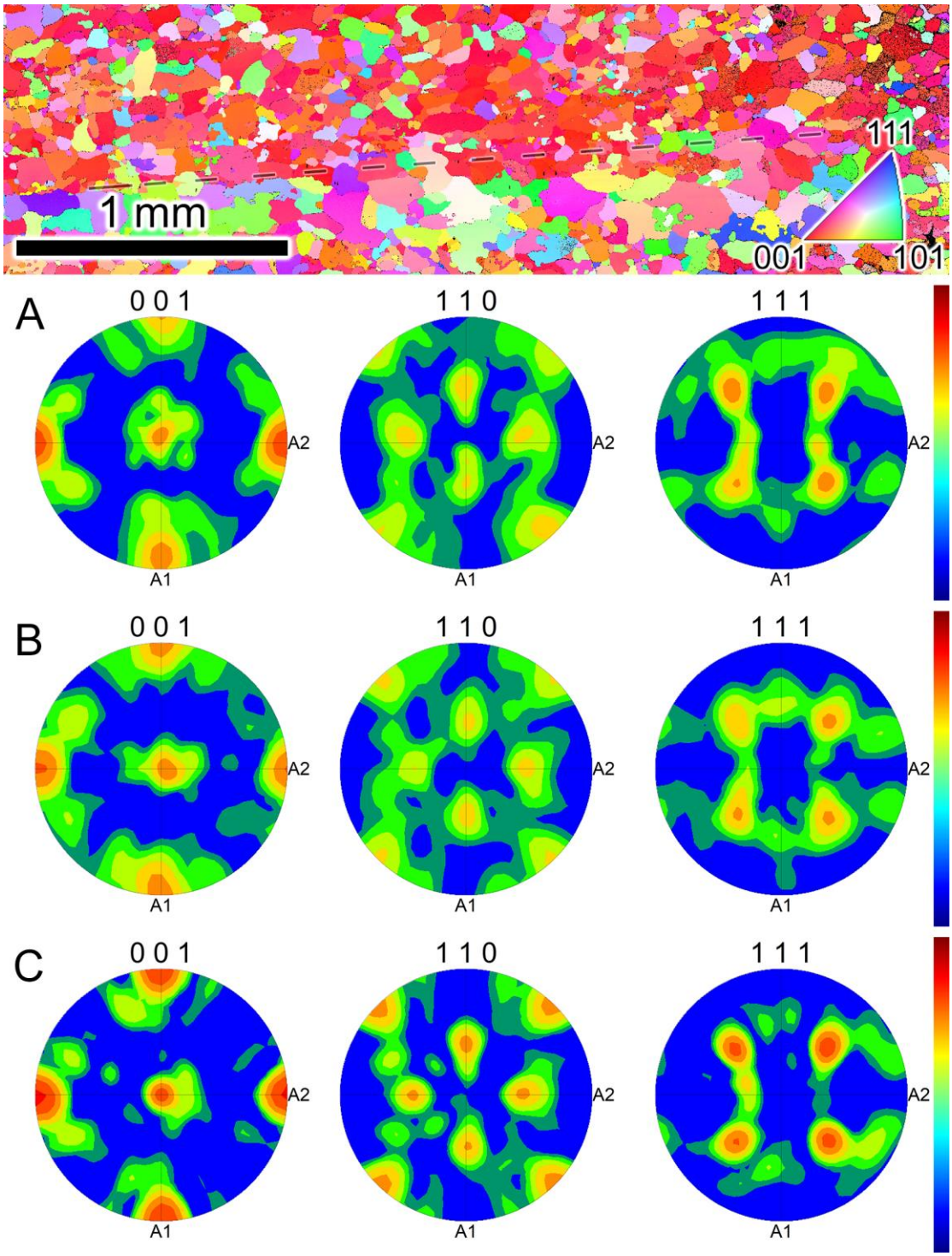

Figure 36. (Top) An IPF map generated from an EBSD scan on a T4 sample with composition C. The faint dashed line shows a boundary between areas with a strong <001> texture and a random texture. Color legend is in logarithmic scale 1-10 times random.

Before the bending tests, texture of T6 (**Figure 35**) and T4 (**Figure 36**) microstructures were investigated with EBSD. The scan parameters are as follows: all T6 samples were scanned over 3,000 × 1,000 μm using 1.5 μm step size. 2 μm step size was used for all T4 samples, but the scan areas varied depending on the composition: 3,500 × 1,000 μm for Alloy A; 3,000 × 1,200 μm for Alloy B; and 3,000 × 1,000 μm for Alloy C. Each scan contained over 850 grains and 1000 grains for T6 and T4, respectively.

The inverse pole figure (IPF) maps of the representative T6 and T4 textures are shown at the top of the corresponding figures. Both tempers contained noticeably large numbers of <001> oriented grains. This is reflected on the pole figure maps, where all the alloys exhibited strong cube texture (**Figure 37**), although there seemed to be areas that showed random texture between bands of strong <001> textured grains represented by faint dashed lines in **Figure 35** and **Figure 36**. The orientation of the bands appears to coincide with the RD. Comparing each pole figures among different compositions, composition C exhibited the strongest level of cube texture.

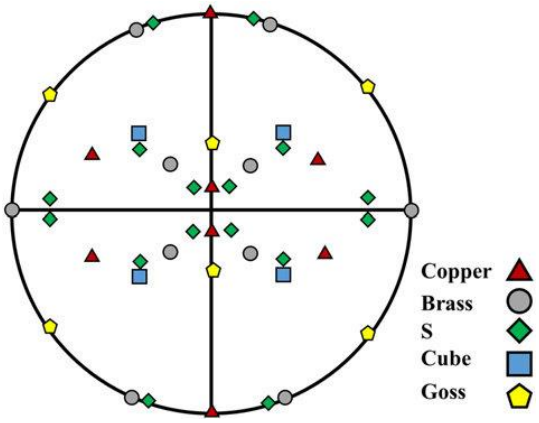

Figure 37. Major ideal crystal orientations and textures of FCC metals on a (111) pole figure [111]. Reprinted with permission from Elsevier.

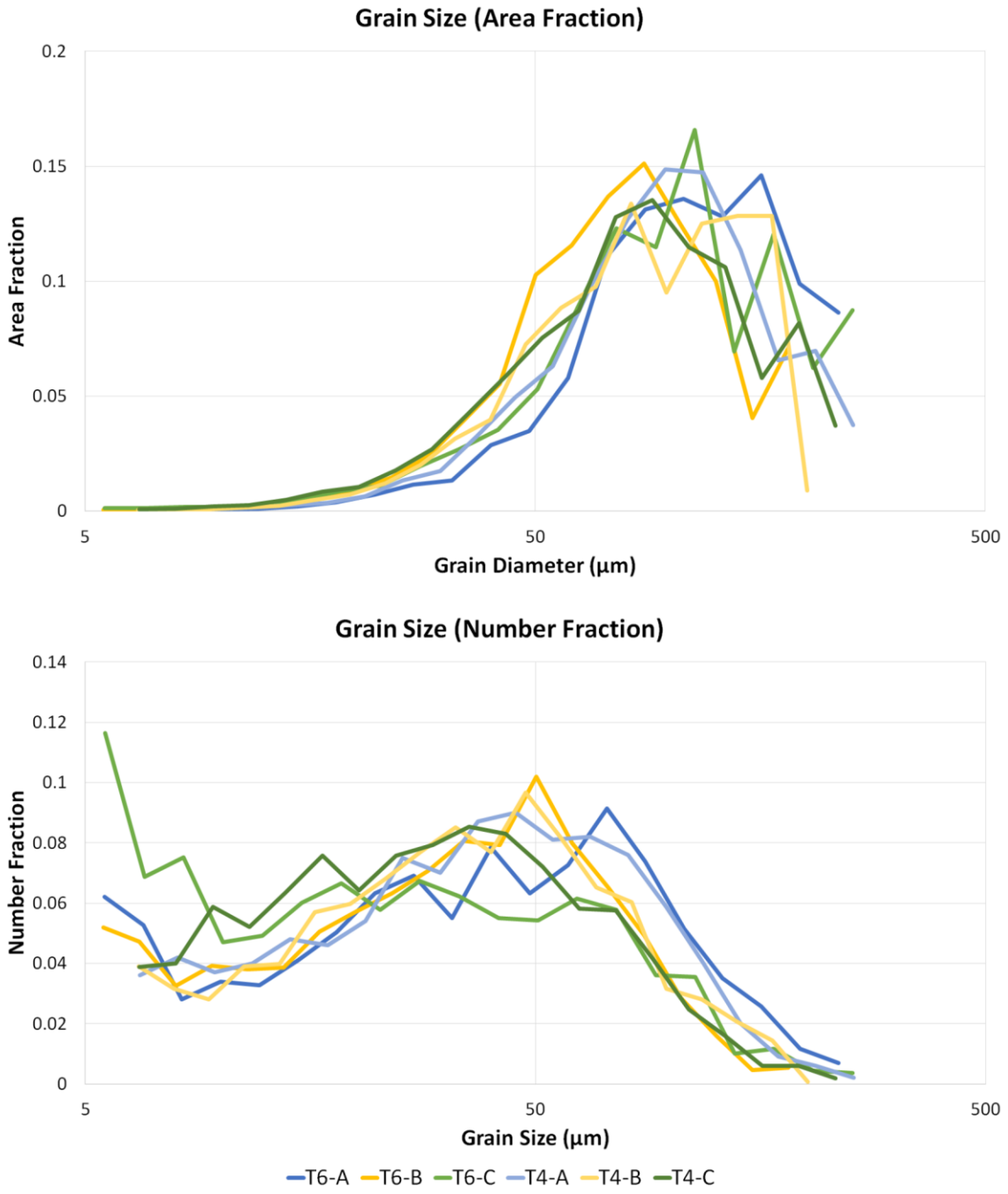

Figure 38. Grain size distribution plotted against area fraction (top) and number fraction (bottom). Grains whose diameters were less than 5 and 6 µm in the T6 and T4 EBSD scans, respectively, were excluded from the analysis. Blue, yellow, and green represent samples with compositions A, B, and C, respectively.

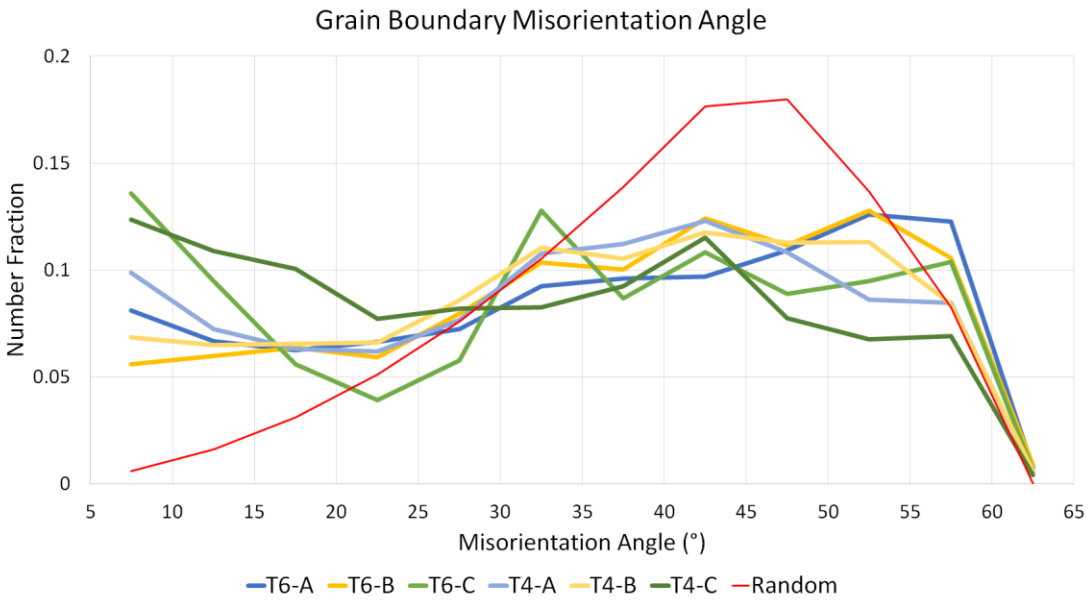

Figure 39. Grain boundary misorientation angle histogram represented with lines to avoid data overlap. The red line represents the random distribution of misorientation angle, known as the Mackenzie distribution [112]. The color legend is the same as that in **Figure 38**.

Figure 38 shows the area fraction and the number fraction of grains were analyzed using the large-area EBSD scan data from **Figure 35** and **Figure 36**. The composition variation revealed no significant difference in grain size and population. Most of the grains are 50 μm in diameter on average and fall within the 10-100 μm range.

As shown in **Figure 39**, the grain boundary misorientation angle histograms showed significant deviation from the Mackenzie distribution, a misorientation angle histogram of a random texture [112]. This is presumed to be caused by large number of relatively lower angle grain boundaries arising from significantly large number of <001> oriented grains as shown in **Figure 35** and **Figure 36**.

4.3.1.2 Precipitate Free Zone

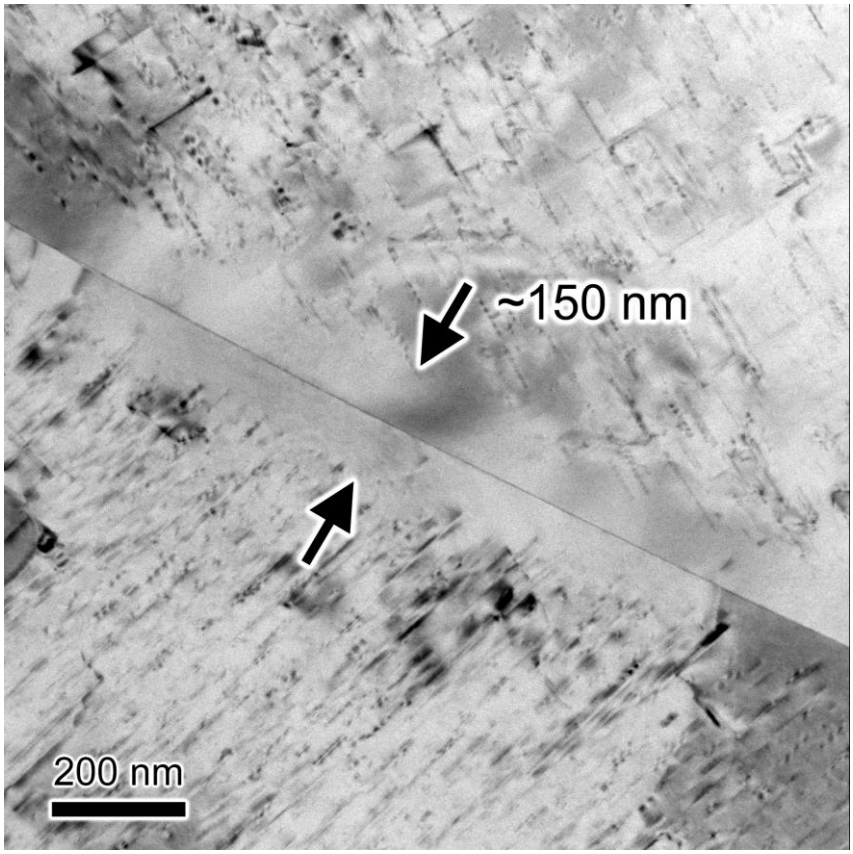

Figure 40. BF TEM image of a PFZ around a grain boundary in a T6 Alloy C.

BF TEM images of jet polished T6 samples were used to estimate the width of the PFZ as a function of composition. When both α and β are tilted to certain two beam conditions, the BF images reveal needle-like Mg_2Si hardening precipitates, as shown in **Figure 40**. In order to measure the PFZ widths correctly, the grain boundaries must be tilted so that the boundary plane normal vector is perpendicular to the electron beam. Due to this limitation, the PFZ widths could not be measured with a large sample size. However, from observations in the TEM, they were estimated to range from 130-300 nm, and variation in composition did not reveal any noticeable changes in PFZ widths.

4.3.1.3 Dispersoid Density

To compare dispersoid number densities as a function of composition, they were measured from the matrix and grain boundaries. The former was done by taking ADF STEM images and feeding them into the MATLAB image processing code described in *Section 3.3.6*. The latter was performed by taking SEM images of Ga-embrittled samples and manually counting the features and dips on the grain boundary surface.

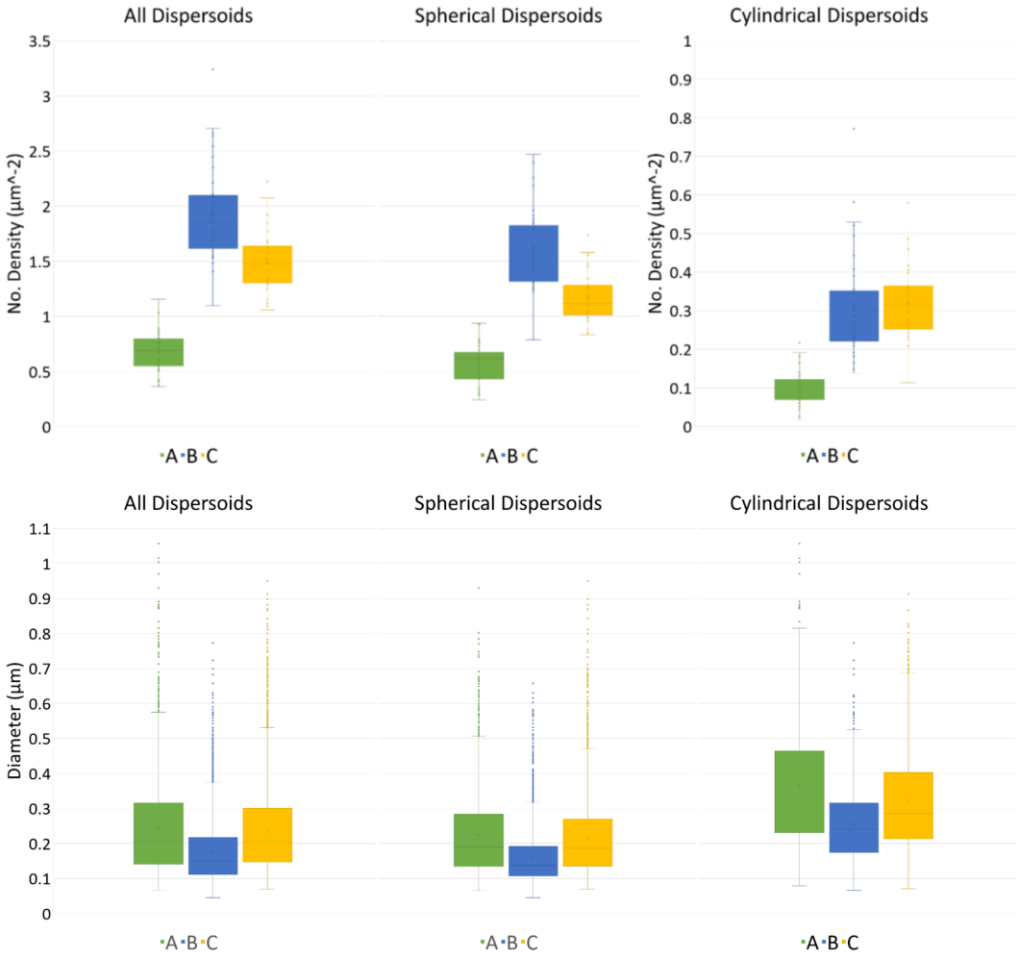

Figure 41. Dispersoid number densities (top) and diameters (bottom) measured from jet polished T4 samples of three different compositions. Different species of dispersoids (spherical or cylindrical) are distinguished based on their aspect ratios.

The results of the ADF STEM image analysis are shown in **Figure 41**. The dispersoid densities and diameters were analysed for 40, 41, and 38 images for Alloys A, B, and C, respectively. Each image was taken at the same magnification and covered an area of 10.73 × 10.73 μm. The overall dispersoid densities for B and C were higher than that of A: the average dispersoid densities for Alloys A, B, and C were 0.68, 1.93, and 1.49 μm^{-2}, respectively. Analysis of variance on three number density data sets (all dispersoids, spherical dispersoids, and cylindrical dispersoids) was conducted on 38 randomly selected STEM images. The p-values of the analysis were sufficiently low—1.58801×10^{-33}, 3.10834×10^{-32}, 5.44819×10^{-19}, respectively—suggesting that there are quantifiable differences among number densities of dispersoids in samples A, B, and C. The cylindrical dispersoids were noticeably longer and less populous than their spherical counterparts, possibly as a result of different nucleation mechanisms. The particles did not exhibit strong clustering and were uniformly distributed throughout the matrix.

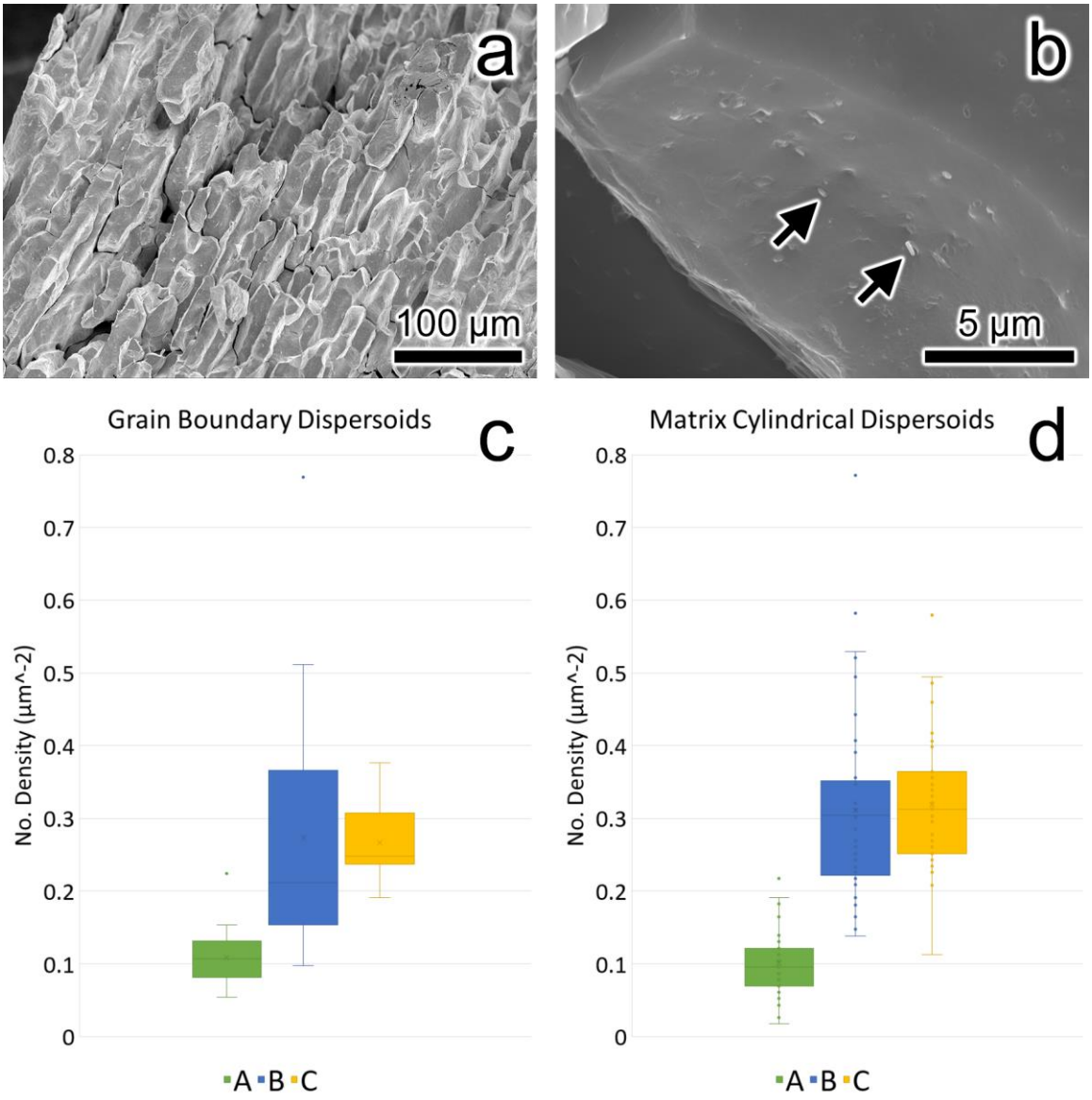

Figure 42. a-b) SEM images of Ga-embrittled Alloy C. The number of features (black arrows) were assumed to be locations where dispersoids fell out during the Ga-embrittlement. c) The corrected area of the grain boundary was used to calculate the dispersoid number density on grain boundaries. d) For comparison, cylindrical dispersoid density measured from the matrix (**Figure 41**, top right) is also shown.

Figure 42 shows the results from measuring grain boundary dispersoid densities on Ga-embrittled T4 samples. SEM images (**Figure 42a**) showed that grains retained their morphologies after Ga-embrittlement. As shown in **Figure 42b**, the grain boundary surfaces had pockets and other features that matched the dimensions of dispersoids, suggesting that dispersoids were once present but fell out during the embrittlement process. The features were counted and normalized by the estimated area of the grain boundary (Subsection 0) to calculate the grain boundary dispersoid density. Because leftover Ga covered many of the grain boundaries, only 15, 15, and 10 grain boundaries from Alloys A, B, and C, respectively, were viable candidates for calculating dispersoid densities.

The average grain boundary dispersoid densities for Alloys A, B, and C were 0.109 ± 0.0411, 0.274 ± 0.1745, and 0.267 ± 0.0537 μm^{-2}, respectively. Consistent with dispersoid density measurements from the matrix, B and C contained more dispersoids than A. The average dispersoid densities of B and C are comparable to each other, making it difficult to differentiate them solely based on dispersoid densities. Since B and C contain more Mn than A, addition of Mn appears to significantly increase dispersoid densities while addition of Cr has little to no effect.

4.3.2 Three-Point Bend Test Results

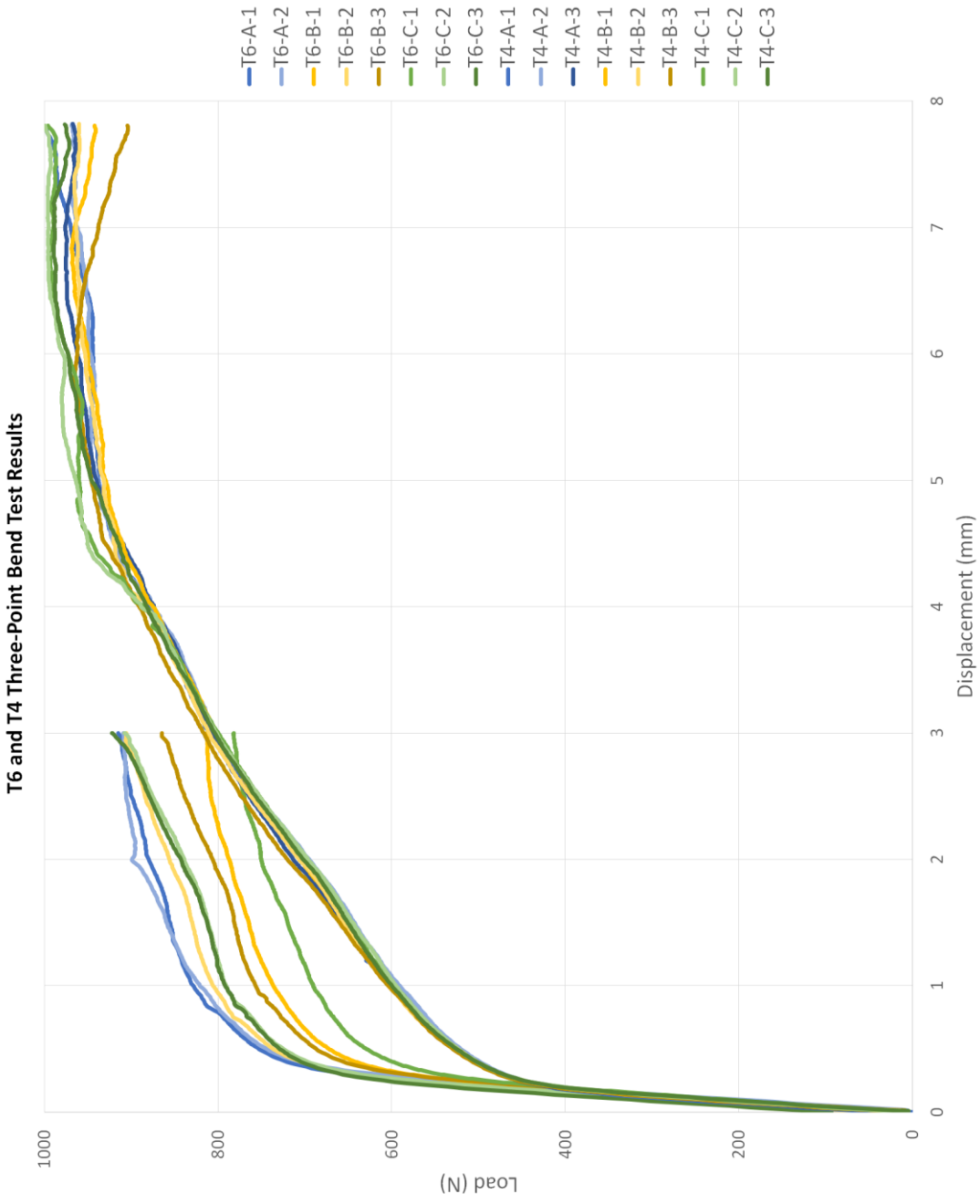

Figure 43. Three-point bend test results for T6 and T4. Applied displacements are 3 mm and 8 mm for T6 and T4, respectively. Blue, yellow, and green represent samples with compositions A, B, and C, respectively. To avoid clutter, T6 samples displaced to 1 mm are not shown.

Figure 43 shows the load-displacement results from the three-point bending tests. Estimations of the nominal strains in the deformed region were about 15% and 24% for 3 mm and 8 mm displacements, respectively. The nominal strain in the deformed region was calculated by measuring the arc of the plastically deformed front plane (as highlighted in **Figure 26**) and comparing the equivalent arc in the neutral plane, which is assumed to be the middle of the sample thickness. This assumption was used because Struers Minitom did not produce sample lengths that were consistently 31 mm in length.

As expected, the precipitate hardened T6 samples exhibited higher yield strength and flow stress than the T4 samples. However, the load-displacement curves for the T6 were more scattered than those for the T4. This disparity is thought to be a consequence of the difference in localized deformation behavior. As will be shown in subsequent sections, plasticity is primarily accommodated at the grain boundaries in T6 while T4 can form slip in the matrix as well. The limited capacity for plastic deformation in T6 will result in scattered mechanical responses due to their reliance on the stochastic nature of grain boundaries. In contrast, plastic deformation occurs in the matrix as well as grain boundaries, and having more channels of accommodating plasticity decreases the influence of randomness of grain boundary character.

Comparisons among different compositions revealed no clear trends in the load-displacement curves. It appears the maximum displacement limit of 8 mm was insufficient to see significant load drops indicative of mesoscale cracking. Only one of the T4 curves (T4-B-3) showed the load drop after achieving maximum load at around 6 mm displacement.

4.3.3 SEM Surface Characterization

4.3.3.1 AA6451-T6 Surface

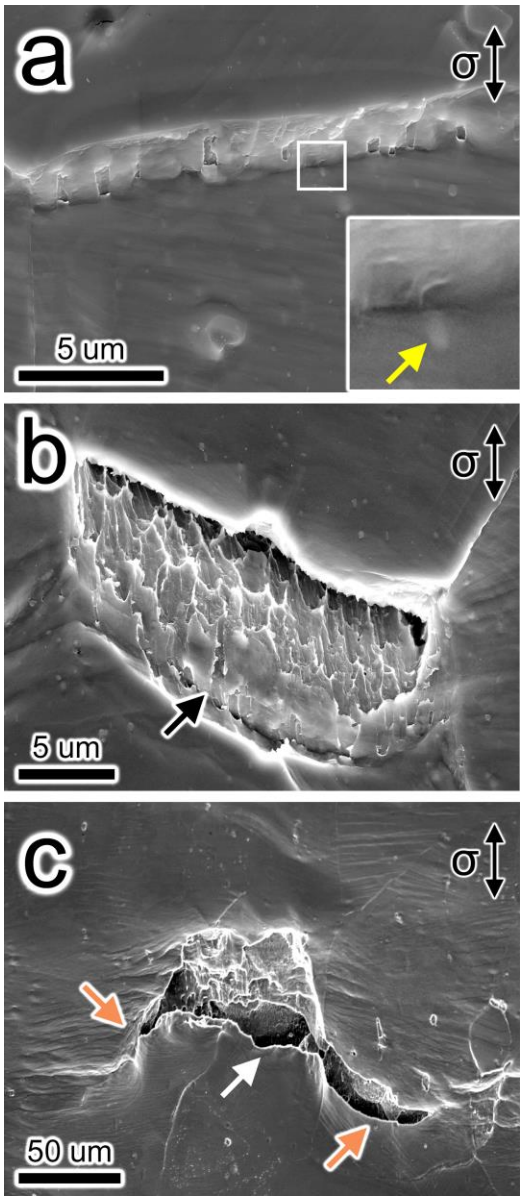

Figure 44. SEM images of a bend tested T6 sample showing a) a grain boundary ledge (GBL); b) crack initiation at a GBL; and c) a crack initiated at a grain boundary (white arrow) growing into neighboring grains (orange arrows). The yellow arrow highlights a sub-surface dispersoid under the hole. The black arrow indicates a streak caused by a dispersoid during ledge formation.

In AA6451-T6, cracks initiated almost exclusively at grain boundaries. Crack initiation is preceded by formation of grain boundary ledges (GBL), where the surfaces of adjacent grains "elevate" relative to one another, forming a smooth surface at the grain boundaries (**Figure 44a**). This behavior is likely caused by the precipitate-hardened matrix of T6 alloys, making it energetically favorable to accommodate plasticity at the softer PFZ with grain boundary deformation rather than in the harder matrix with slip, which Davidkov *et al*. also observed in age hardened AA6016 [109]. However, they did not report GBL formation but instead found grain boundary decohesion. This is likely due to higher Mg_2Si density at grain boundaries and smaller PFZ width due to different processing parameters that made AA6016 more brittle. Although slip traces were observed on the surface, they were not very prominent and none of them appeared to be associated with crack formation. GBL exhibit smooth surfaces with occasional holes and streaks (**Figure 44a**), presumably artifacts of dispersoid particles lodged at the grain boundary during GBL formation. The inset in **Figure 44a** shows a dispersoid underneath the hole at a GBL.

A close observation of the crack (**Figure 44b**) shows that it undergoes ductile fracture where smooth GBL was formed. Close to the surface of the sample, the crack surface is smooth from GBL formation, which implies that all cracks initiate near grain boundaries. The streak in this smooth region (**Figure 44b**, black arrow) is possibly an artifact left by a dispersoid during GBL formation. The dimpled crack surface deeper into the sample suggests that once the localized grain boundary deformation induces GBL formation, the initiated crack undergoes ductile fracture. As the crack grows, it can transition to a transgranular crack (**Figure 44c**).

4.3.3.2 AA6451-T4 Surface

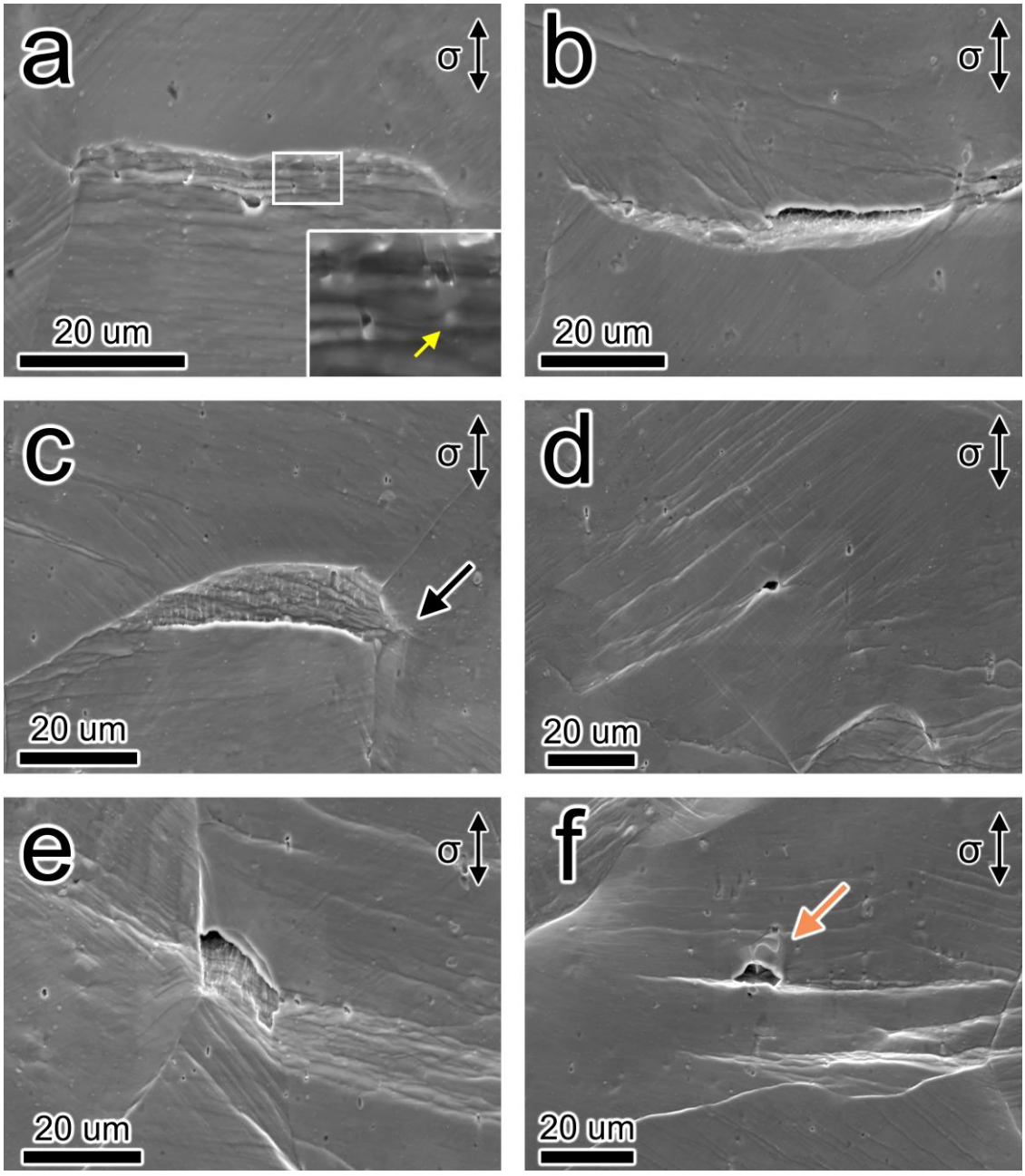

Figure 45. SEM images of a bend tested T4 sample showing a) a grain boundary ledge (GBL); b) crack at a GBL; and c) transition into a transgranular crack (black arrow). A magnified image of a dispersoid (yellow arrow) under a GBL is shown in the inset. Cracks were also observed where slip interacted with d) other slip bands in the matrix; e) a grain boundary; and f) a constituent particle (orange arrow).

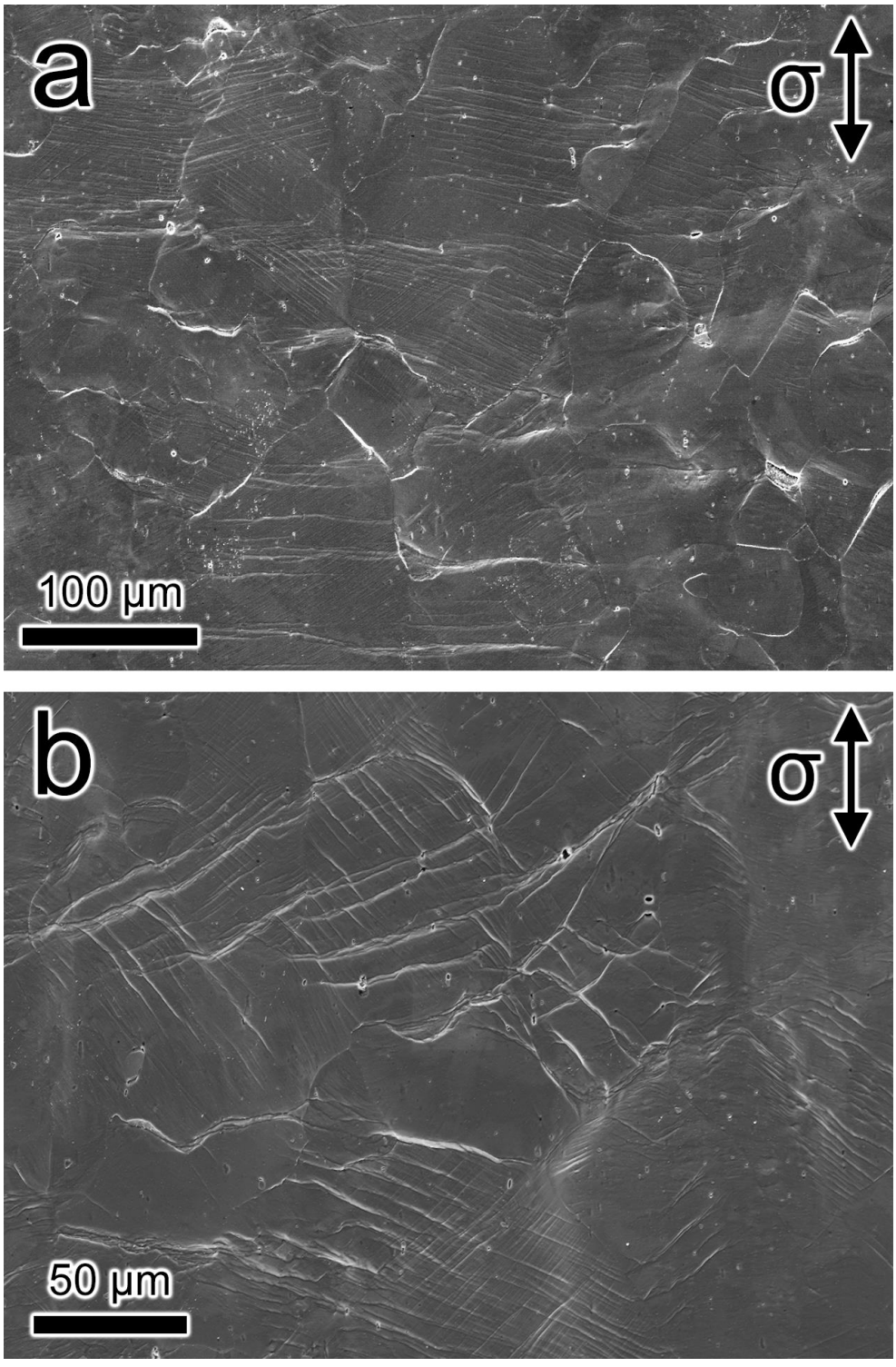

Figure 46. SEM images of bend tested a) T6 and b) T4 sample surfaces showing significantly more pronounced slip activity in T4.

Cracks originating from grain boundaries in T4 exhibit a similar crack initiation process as T6. Smooth GBL are formed along grain boundaries that experienced high levels of localized deformation. Some ledges have holes that are presumably artifacts of dispersoids dragging along grain boundaries during their formation (**Figure 45a**, inset). Cracks are formed at GBL (**Figure 45b**) with dimpled fracture surfaces indicative of subsurface ductile fracture. **Figure 45c** shows that cracks in T4 can also propagate into the adjacent grain and transition into a transgranular crack (**Figure 45c**, black arrow).

Most of the cracks are located at the grain boundaries, suggesting that grain boundaries remain as a major outlet for stress relief. In addition to localized grain boundary deformation, the T4 matrix can also plastically deform. Unlike T6, T4 does not contain hardening precipitates, allowing slip bands to form in the matrix for plastic deformation. As shown in **Figure 46**, the slip traces in the matrix is much more pronounced in T4 than in T6. Consequently, surface cracks can form when the strain buildup exceeds critical thresholds when slip interacts with various microstructural defects. **Figure 45d-f** show cracks resulting from multiple active slip systems (**Figure 45d**); slip band formation at a grain boundary (**Figure 45f**); and dislocation accumulation at a constituent particle interface (**Figure 45f**). The variety of means of plastic deformation increases the capacity for dislocation generation and glide, requiring more energy to reach critical failure and making T4 much more ductile than T6.

4.3.3.3 Constituent Particle Cracking

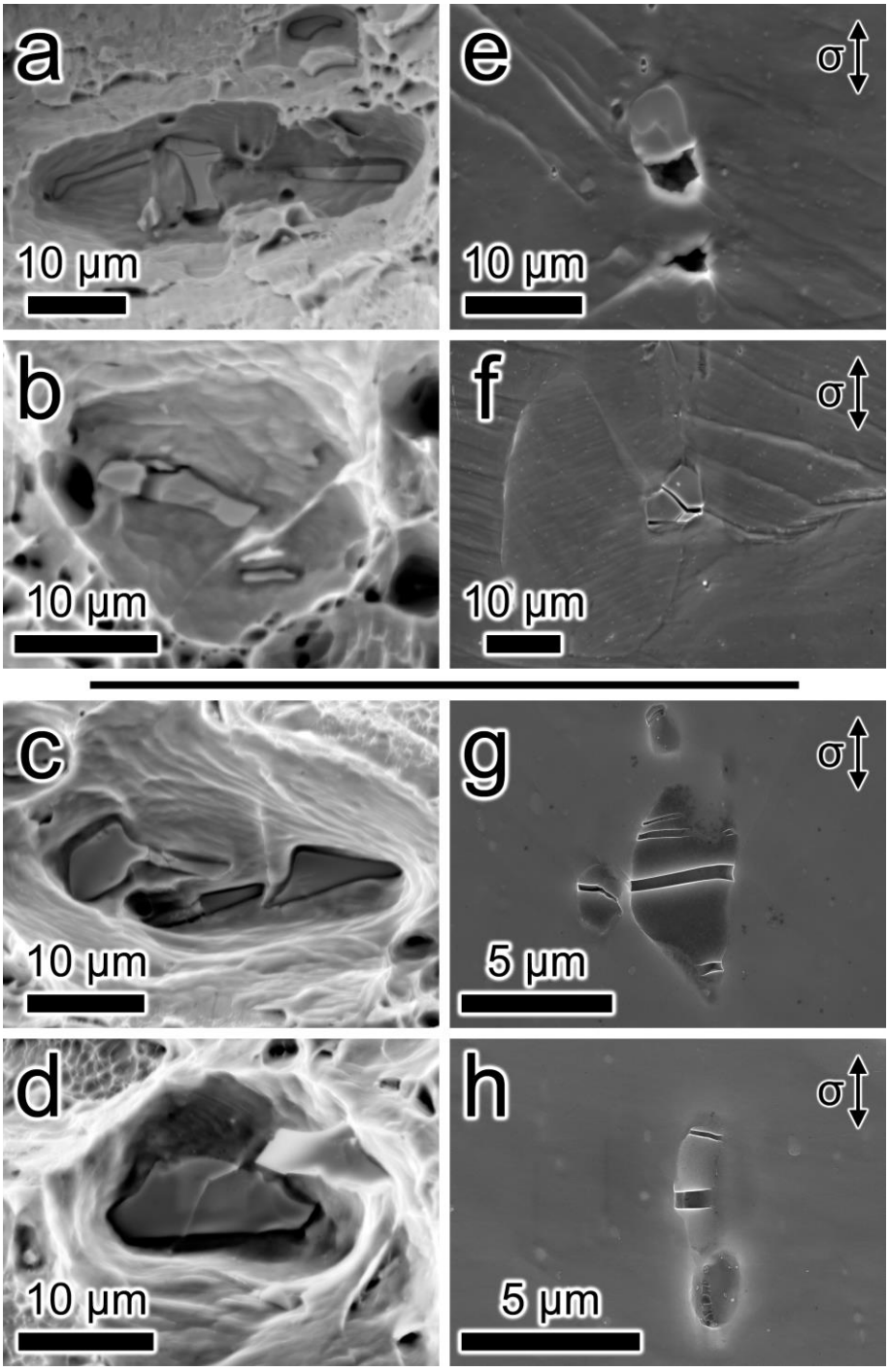

Figure 47. Constituent particles found on fracture surfaces of tensile tested (left) and front planes of three-point bend tested (right) AA6451-T4 (top four) and -T6 (bottom four).

Constituent particles from bend tests were compared with those from fracture surfaces after tensile tests. While failure initiation in tension is a particle-driven process as discussed in Section 2.3.1.2, the constituent particles from bend tested samples revealed that they are not primary crack nucleation sites during three-point bending. The fractography images (**Figure 47a-d**) showed cracked constituent particles at the center of dimples, indicating that constituent particles serve as crack nucleation sites during ductile failure. Constituent particles in both bend tested T6 and T4 were also found cracked (**Figure 47e-h**). Contrary to some previous findings [105, 107], however, none of the cracks extended beyond the particle-matrix interface and propagated into the matrix, suggesting that constituent particles are not active crack nucleation sites. This is likely caused by the difference in stress states imposed on the particles as a result of their proximity to the sample surface.

4.3.4 FIB Cross-Section Analysis

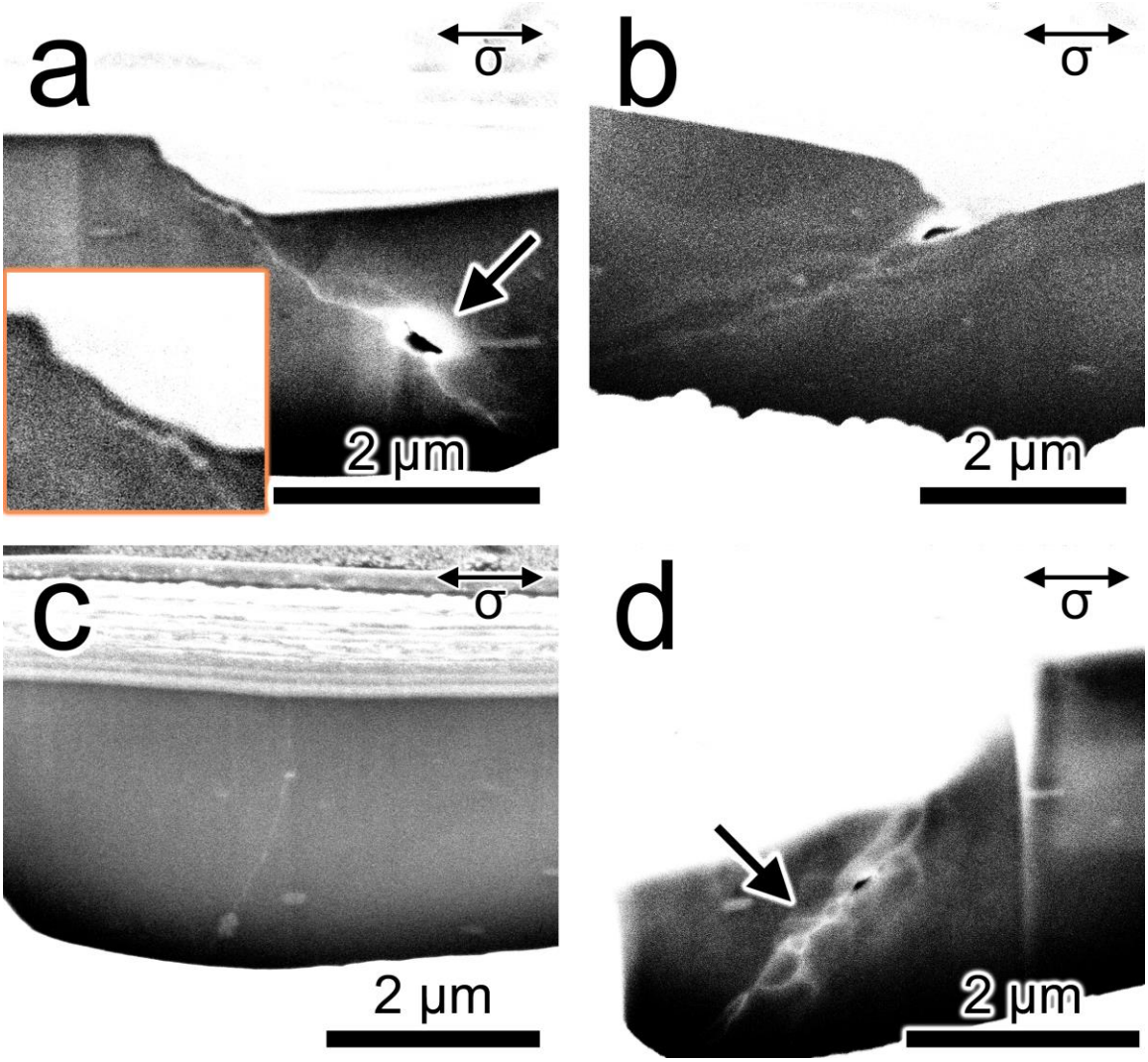

Figure 48. Immersion mode images from FIB cross-sectioned areas with a) GBL with subsurface void (black arrow); b) cracked grain boundary where faint white lines indicate grain boundaries; c) no GBL; and d) grain refinement (black arrow) associated with a GBL (taken from Alloy A). The orange inset shows that the native grain boundary does not coincide with the GBL. The orientations of grain boundaries are captured on cross-sectioned surfaces at a 52° sample tilt. The tensile load direction is horizontal in the plane of the page, shown with black arrows.

Table 7. Corrected angles of grain boundary orientations measured from cross-section analysis. Sixteen grain boundaries with or without grain boundary ledges and cracks have been chosen at random.

θ	Minimum	Maximum	Average	Median
No GBL	70.0°	86.4°	78.2°	78.2°
GBL	13.9°	69.3°	38.1°	34.2°
Small Cracks	23.4°	69.3°	45.1°	37.8°
Large Cracks	47.2°	52.1°	49.6°	49.6°

In order to study the microstructural factors that influence GBL formation, cross-section analyses were performed on sixteen grain boundaries in a T6 samples. More specifically, the orientation of grain boundaries with respect to the tensile load axis was measured, and each region of interest (ROI) was categorized as either with or without a GBL. The former was further categorized based on the sizes of cracks. The ROI were chosen from areas that experienced the highest tensile stress, and the tensile load axis is approximated to be parallel to the surface in cross-sectioned images. The angle between the loading axis and grain boundary was measured at the surface, and corrections for the 52° sample tilt are described in *Section 3.3.2*. Examples of angle measurements are shown in **Figure 28c-d**. The results are summarized in **Table 7**. It was found that the grain boundary orientation played a significant role determining which boundaries form ledges. The grain boundaries that are oriented close to 90° (above 70°) from the tensile load axis were more resistant to GBL formation (**Figure 48c**). The boundaries with ledges were oriented 13-70°, and no clear trend was found that influenced the sizes of cracks.

Dependence on grain boundary orientation is likely a result of deformation occurring almost exclusively at grain boundaries. It serves as an equivalent to the orientation of slip planes in a classic illustration of calculating resolved shear stress (RSS) in a single crystal. When the slip plane normal is parallel to the tensile load axis (*i.e.* oriented 90°), the resolved shear stress is zero, and slip should not occur. In the case of AA6451-T6, GBL a sign of plastic deformation near grain boundaries, possibly within the relatively softer PFZ. If the grain boundaries are oriented 70-90°, dislocation mobility is limited to the area between the boundary and the hardened matrix. However, when the grain boundaries are oriented 13-70°, the dislocations can glide relatively easily in the PFZ to the surface of the sample, creating an observable feature of slip activity: GBL.

The images also revealed that subsurface voids can form along grain boundaries (**Figure 48a**), possibly as a result of concentrated plastic strain at triple junctions or where slip meets the boundary. The inset in **Figure 48a** shows that GBL does not coincide with the grain boundary, suggesting that accumulation of plastic deformation in the PFZ is responsible for GBL formation, not the movement of grains themselves. **Figure 48b** shows an example of a small surface crack forming at the GBL. Small grains were also observed around native grain boundaries (**Figure 48d**). This type of small grains was not observed in TEM studies of the undeformed jet polished T6 specimens and was likely a result of the bend tests. This grain refinement behavior will be further discussed in later sections.

4.3.5 EBSD Analysis

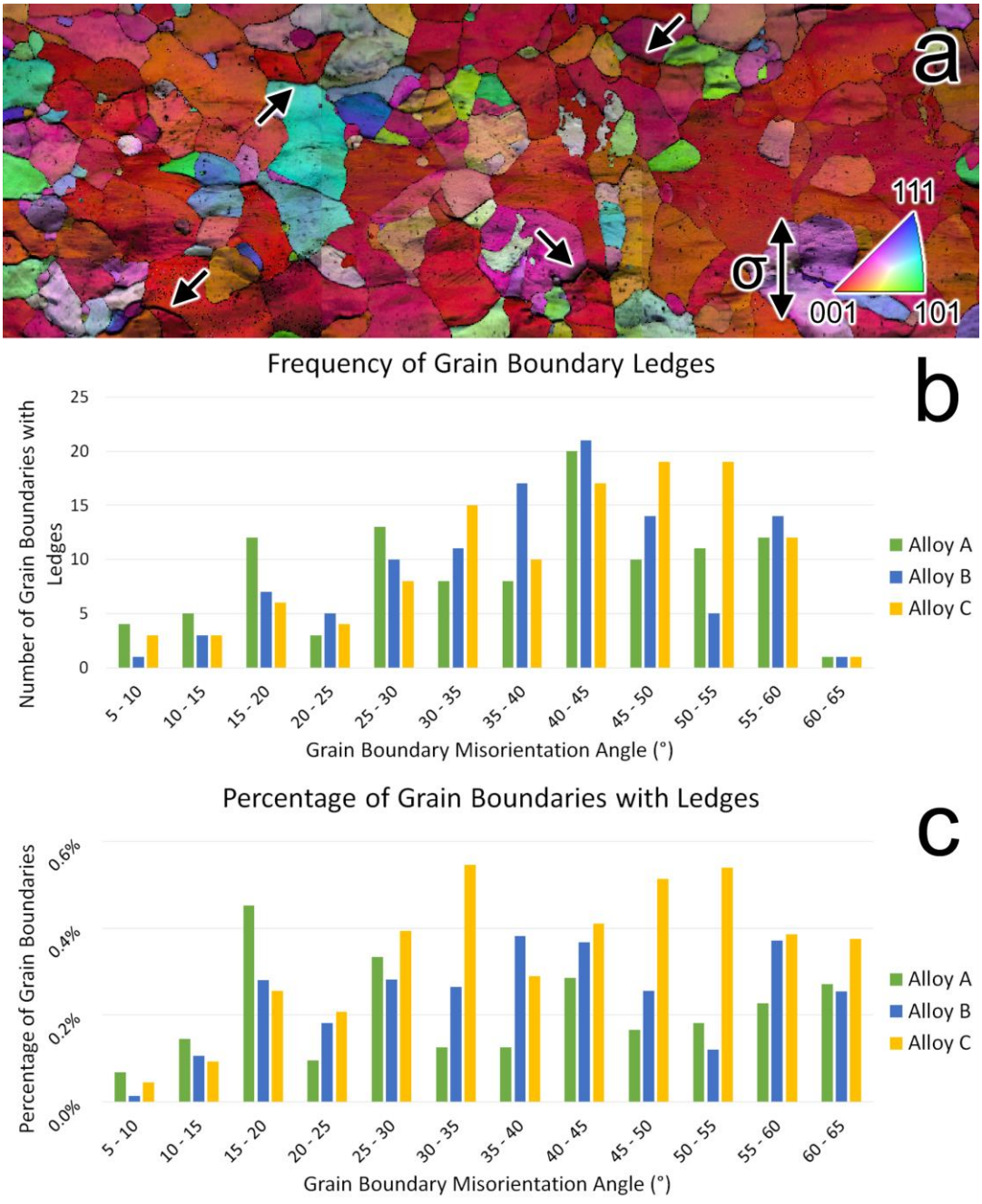

Figure 49. IPF map overlaid with the image quality (IQ) map generated from EBSD scans after deforming a T6 sample to 1 mm displacement. Histograms of b) number of grain boundaries with GBL and c) data normalized by the total number of grain boundaries within each of the misorientation angle range.

To explore the effects of grain boundary misorientation angles on GBL formation, seven, nine, and ten 700 × 700 μm EBSD scans using 2.5 μm step size were collected from T6 Alloys A, B, and C after applying 1 mm displacement. EBSD scans from T4 were not usable for analysis due to the significant surface roughness. **Figure 49a** shows IPF maps overlaid with image quality maps stitched together. Consistent with results from **Figure 35** and **Figure 36**, the IPF maps exhibited strong cube texture—most of the grains were red <001> grains. The image quality (IQ) maps, whose grayscale values increase depending on the quality and intensity of the EBSP, showed that GBL create "shadows" over their corresponding grain boundaries, showing up as thick black lines (**Figure 49a**, black arrows). Misorientation angles were determined by manually selecting grain pairs that neighbor GBL in the OIM Analysis software. 108, 117, and 118 grain boundaries were selected from Alloys A, B, and C to generate histograms shown in **Figure 49b-c**. Only boundaries that clearly bordered only two grains were selected. **Figure 49b** shows the number of GBL whose grain boundaries were within each misorientation angle range of the histogram. **Figure 49c** shows the data from **Figure 49b** normalized by the number of grain boundaries that fall within each misorientation range.

The results showed no correlation between GBL and grain boundary misorientation. Each sample exhibited peaks in certain intervals, but they were no consistent across different compositions. From the same EBSD data, a preliminary examination of the Schmid factor maps also revealed no trends. This suggests that the microstructural drivers for GBL formation in T6 is almost limited to grain boundary orientation and the PFZ size and that factors from the matrix has very little influence.

4.3.6 STEM and TKD Characterization

Previous mesoscale microscopy results identified grain boundaries and GBL as the most important microstructural features for crack initiation in T6 and T4. T6 and T4 samples were bend tested with applied displacements of 3 mm and 8 mm, respectively, to induce plastic deformation. Then FIB lift-out specimens were extracted from numerous grain boundaries in Alloys A, B, and C of both tempers. In this section, examples from a few lift-out specimens with representative features of interest will be shown to investigate the crack initiation mechanism of AA6451-T6 and -T4 during three-point bending tests.

To distinguish types of grain boundaries based on their origin, the adjective "native" will be used to refer to microstructural features that were present before the three-point bend tests. Although the term refers to metallurgical processes that produces finer grains, in this study, "grain refinement" will refer to the phenomenon of small grain formation around the native grain boundaries as a result of three-point bending. The grain boundaries that arise from grain refinement will be referred to as "refined grain boundaries".

4.3.6.1 Grain Boundary Ledge Formation and Grain Refinement in AA6451-T6

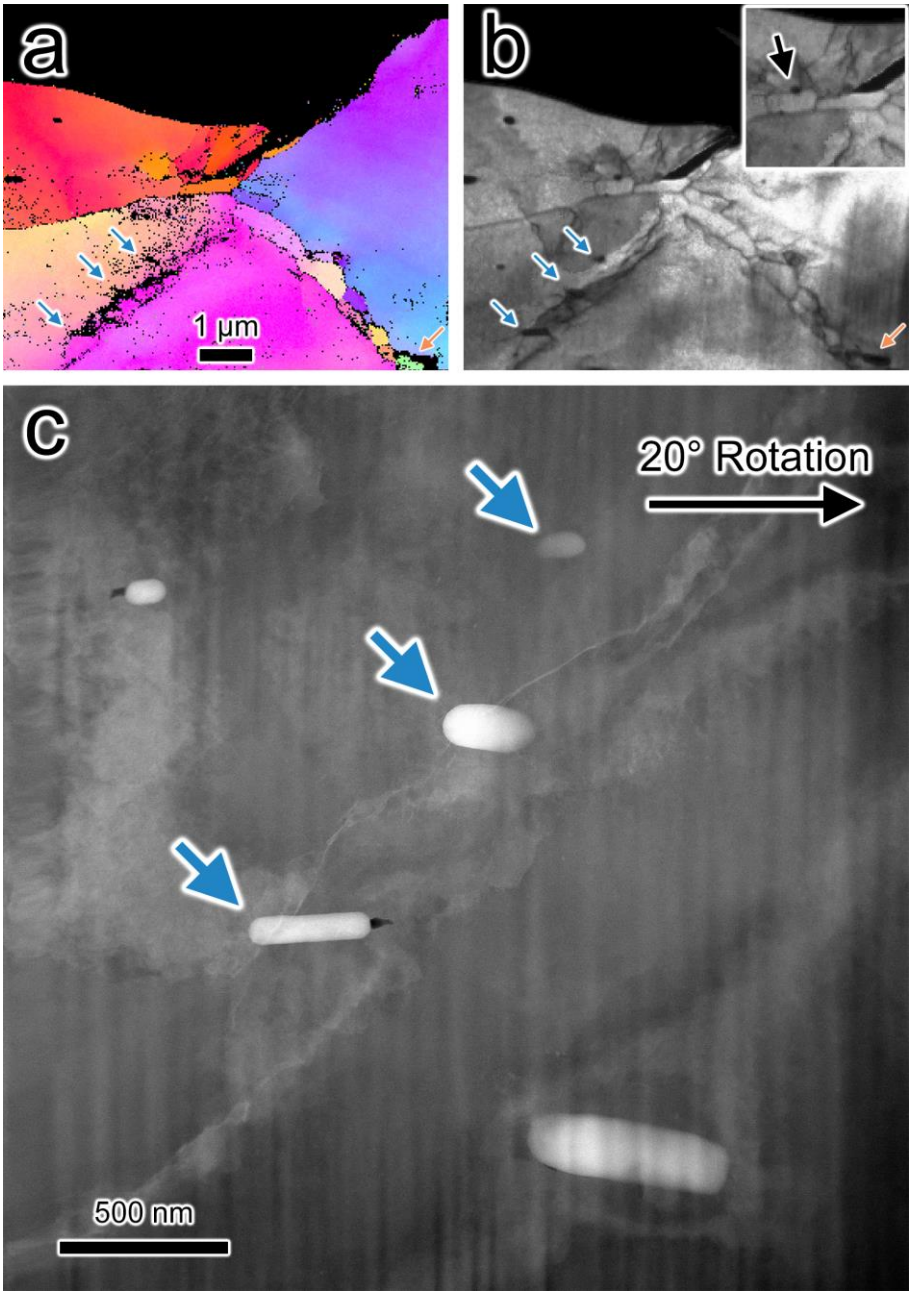

Figure 50. a) IPF and b) IQ maps (magnified in the inset) generated from TKD data of a FIB lift-out specimen extracted from a GBL. The blue arrows highlight three dispersoids that lie on a new boundary forming in a matrix ahead of the surface crack. Orange arrow indicates a cylindrical dispersoid that will be shown in the **Figure 51**. c) ADF STEM image shows the magnified image of the new boundary formation in the matrix.

Figure 50 shows results from TKD and STEM analysis of a lift-out specimen from a GBL in a T6 Alloy C. The IPF map (**Figure 50a**) shows three native grains—red on the left; blue/purple on the right; and yellow/pink at the bottom. Grain refinement can be observed along the three native grain boundaries, particularly between the blue/purple and yellow/pink grains where small grains about 200-500 nm in diameter. This suggests that grain refinement is a process that occurs exclusively within the PFZ in T6. In addition, some of the refined grains formed high-angle grain boundaries with the native grains. A closer inspection of the IQ map revealed that low-angle refined grain boundaries are also visible between the red and the yellow/pink grain (**Figure 50b**, inset). Grain refinement will be examined more in **Figure 51**.

As expected from SEM images of cracks at GBL (**Figure 44b**) and cross-sections (**Figure 48a**, inset), the ledge was formed close to—yet did not perfectly match—the native grain boundary. Observations of the IPF map (**Figure 50a**) showed that the surface crack was nucleated along the boundary between the matrix and the refined orange grains left of the native grain boundary. This indicates that the refined grain boundaries that border the matrix is where damage accumulates the most, serving as crack nucleation sites.

The IQ map (**Figure 50b**) revealed that the source of the significant crystal rotation in the yellow/pink grain is the formation of a new boundary, depicted as diagonal black lines that divide the yellow and the pink regions in the matrix. It is believed that the yellow and pink regions originally constituted the same grain and that the new boundary is a byproduct of mechanical deformation since it does not fully extend to the triple junction

near the crack tip. This new boundary creates a border between the two halves of the grain that results in an approximately 20° crystal rotation.

Since the orientation of the new boundary coincides with that of the surface crack, its formation may be a result of strain concentration ahead of the crack tip. Although there were refined grain boundaries that provided a path for the surface crack to grow into, the crack stopped near the triple junction, presumably because the change in direction was not energetically favorable. Instead, the matrix ahead of the crack exhibited high localized deformation, resulting in a formation of a new crystal rotation boundary. This behavior, however, appears to have been facilitated by the presence of unshearable dispersoids (**Figure 50**, blue arrows) in the matrix. Because of the incoherent dispersoid-matrix interface, dispersoids can pin dislocations [3, 7]. Although this property is a critical part in strain homogenization where strain localization is reduced, **Figure 50c** shows a slip band that was formed as a result of dislocation pinning at the two dispersoids (blue arrows). Despite the lack of slip bands associated with crack initiation or growth in T6, dislocation accumulation has been proven to be a precursor to various failure initiation mechanisms. This tradeoff of dislocation accumulation leading to strain homogenization at low- to mid-level stress and crystal rotation boundary at high-level stress must be considered when designing tougher alloys with dispersoids. The formation of this boundary is further discussed in *Section 4.4.5*.

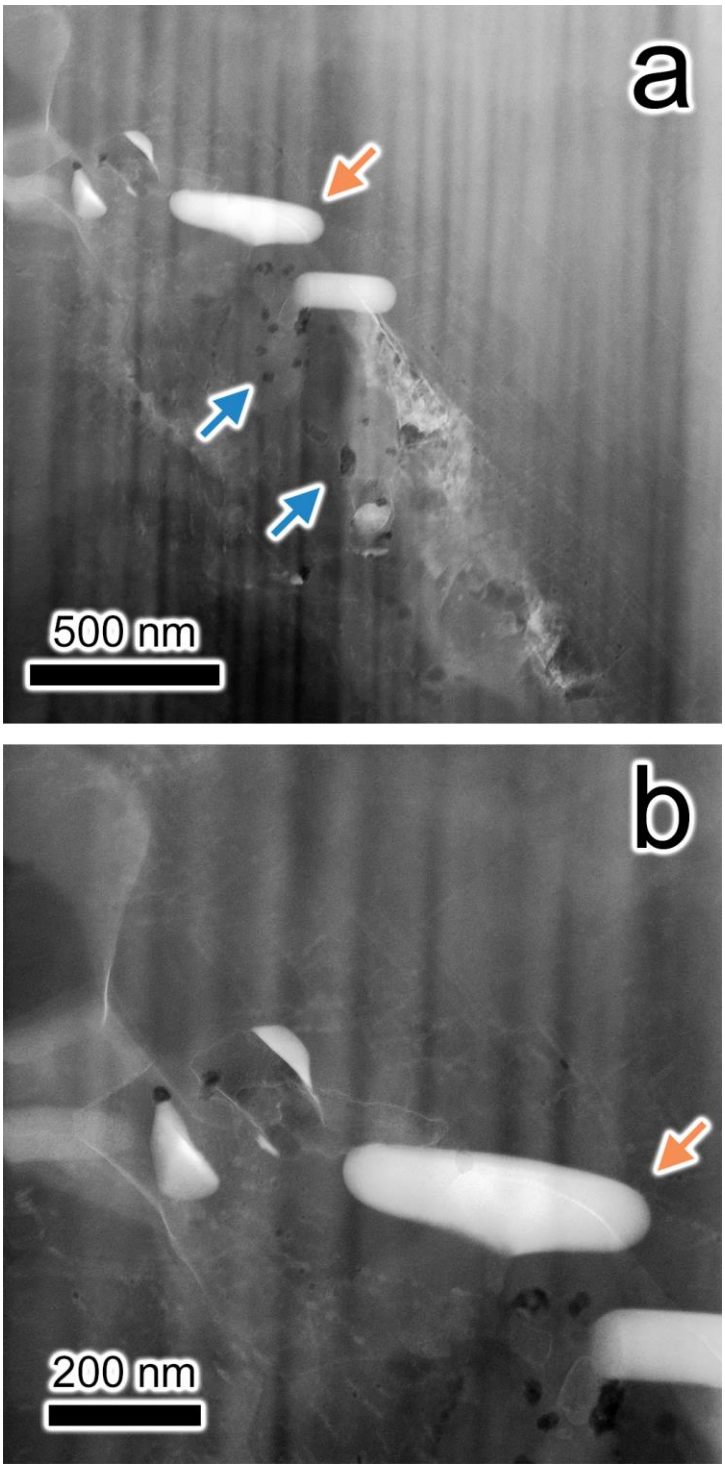

Figure 51. ADF STEM images of dispersoids in the grain refinement zone shown in **Figure 50**. The orange arrow points to the same dispersoid as in **Figure 50**. Blue arrows highlight void nucleation in the grain refinement zone.

Figure 51 shows magnified ADF STEM images of the grain refinement regions highlighted by orange arrows in **Figure 50a-b**. **Figure 51a** shows that the grain refinement zone is riddled with holes (blue arrows), some as wide as 80 nm. Most of the holes are either on the small grain boundaries or the dispersoid interface with the refined grains, which suggest that the localized deformation at the native grain boundaries may cause these cavities to form, possibly as a result of dislocation accumulation at the refined grain boundaries. Although grain refinement was observed in every FIB lift-out specimen from GBL, the holes at the refined grain boundaries were less common. Therefore, above observations are only speculative explanations of their origin and should be taken with caution. While the electron beam in STEM mode can also produce holes in TEM specimen [113], the holes in **Figure 51a** coincide too well with small grain boundaries and dispersoid-matrix interfaces to disregard mechanical sources.

Along with one captured in **Figure 51b**, several other broken dispersoids have been observed in the grain refinement regions in FIB lift-out specimens. Interestingly, the distance between the two halves of the broken dispersoids were on the order of 100 nm without any cavities that suggest the split occurred as a result of three-point bending. This suggests that the particle broke during the thermomechanical manufacturing process (*e.g.* hot rolling), and the space between the fractured particle was filled during subsequent heat treatments. Just like the holes in **Figure 51a**, locations of fractured dispersoids coincide with the small grain boundaries, and the exact process by which the particles fracture is yet unknown.

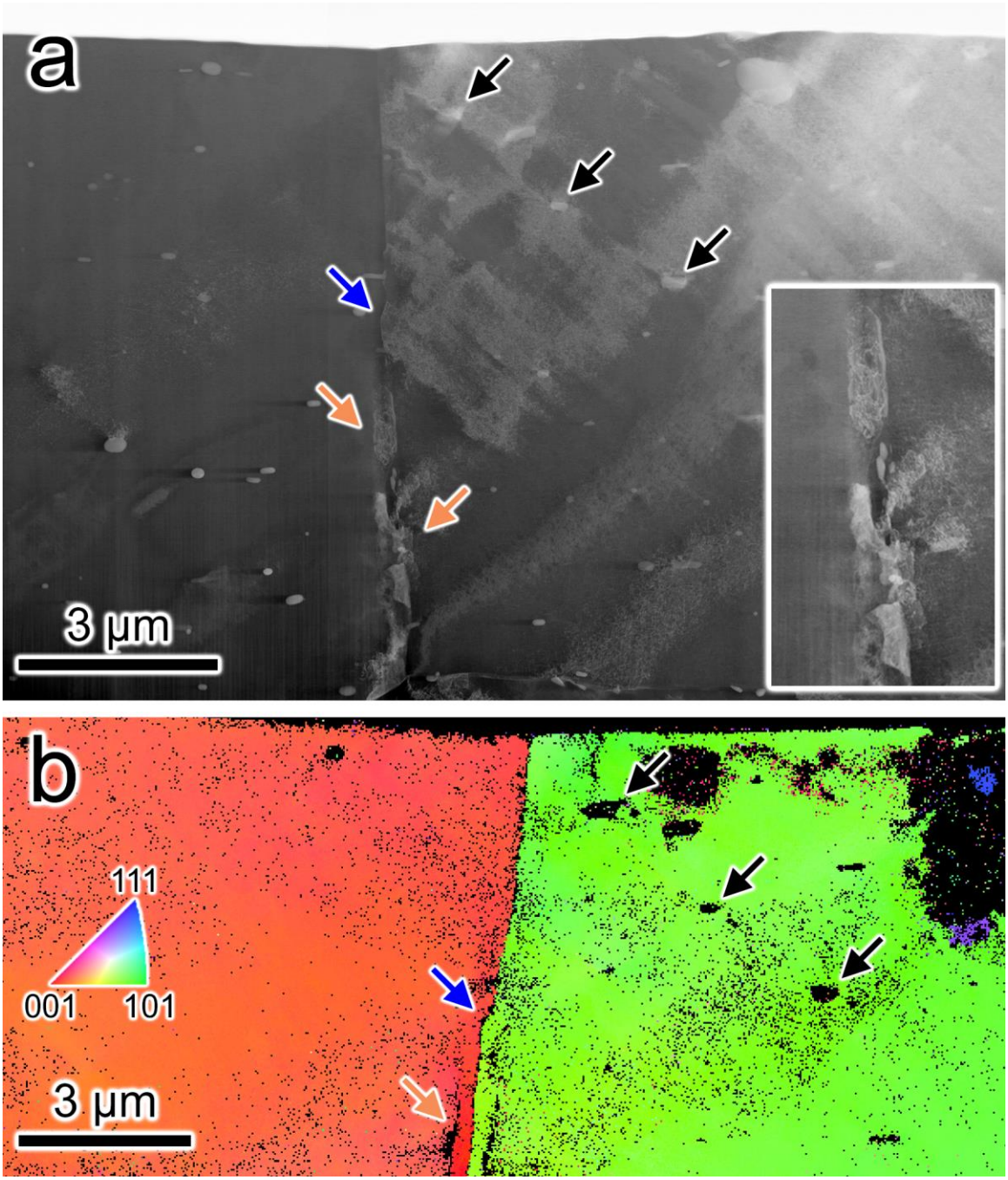

Figure 52. a) ADF STEM and b) IPF map generated from TKD scan of a FIB lift-out specimen from a grain boundary with ledge formation. The inset shows a magnified image of the region exhibiting grain refinement. The slanted grain boundary shown in the IPF map is caused by sample drift during the scan. Black arrows highlight three dispersoids connected by slip bands. Blue arrows indicate a kink in the grain boundary, and orange arrows show signs of grain refinement at the grain boundary (enlarged in inset).

For comparison with the FIB lift-out specimens from GBL, **Figure 52** shows a specimen from a grain boundary without any features of localized deformation. Consistent with the results from the cross-section study (*Section 4.3.4*), the grain boundary was oriented almost 90° from the tensile load axis. Although the native grain boundary itself was resistant to GBL formation, the surrounding microstructure exhibited the same signs of plastic deformation that were also present in **Figure 50**, but to a lesser extent.

Similar to the dispersoids in **Figure 50c**, dispersoids in this specimen (**Figure 52a**, black arrows) were connected by slip bands, caused by dispersoids pinning dislocation movement. The slip bands did not induce severe crystal rotation as the one shown in **Figure 50** presumably because the strain concentration is not as high as the area ahead of the crack tip. Close to the surface, the matrix appears to have multiple active slip systems, as evidenced by the crisscross patterns that arise as a consequence of lattice distortion.

Although the PFZ near the surface was indistinguishable from the matrix, approximately 3 μm below the surface, grain refinement was observed (**Figure 52a**, orange arrows and inset). Refined grains were about 200-300 nm wide—approximately the width of the PFZ—and contained high dislocation content. Although individual grains were not detectable in the TKD data, evidence of severe lattice distortion at the PFZ-matrix interface was observed in the IPF map (**Figure 52b**, orange arrow) as black pixels that have low confidence index. This indicates that although the grain boundary is oriented to naturally resist GBL formation, the PFZ still deforms to form low-angle refined grain boundaries, unlike the high-angle boundaries around GBL (**Figure 50a**).

4.3.6.2 Grain Boundary Ledge and Slip Traces in AA6451-T4

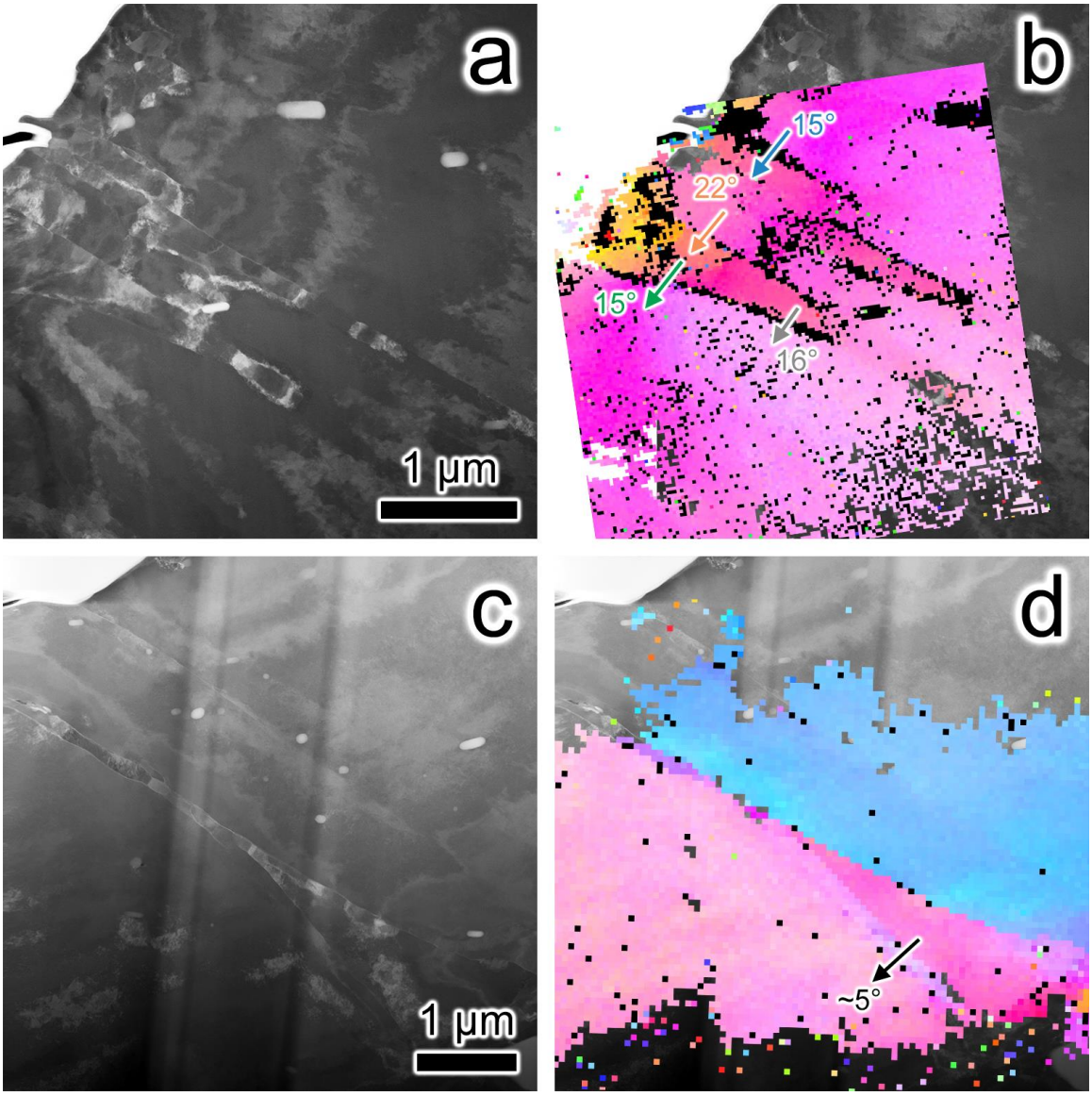

Figure 53. ADF STEM images of FIB lift-out specimens from T4 compositions a-b) A and c-d) B. The images are overlaid with IPF maps generated from corresponding TKD data on the right. Slip bands were observed in the matrix, producing crystal rotation that results in new boundaries. The arrows indicate which points were chosen to measure the misorientation angles. The small black cavity on the left edge of the STEM images are GBL-induced surface cracks.

Figure 53 shows ADF STEM images and TKD analysis results of FIB lift out specimens from T4 samples after three-point bend tests. The IPF maps generated from TKD data are overlaid on top of the ADF STEM images to identify areas with significant crystal rotation. Unlike that of T6, the T4 matrix is free of hardening precipitates that hinder glissile dislocation movement, and the abundance of slip activity in the matrix confirms this. SEM images (**Figure 46b**) show that multiple slip systems are clearly active on the surface, and several grains showed the same behavior. However, when the matrix is close to heavily deformed grain boundaries, such as those with GBL-induced surface cracks, one slip system becomes the dominant system for plastic deformation. For example, **Figure 53a** shows slip bands forming in the matrix next to a surface crack (black cavity on the left). TKD data (**Figure 53b**) show that the concentrated plastic strain around the bands induce crystal rotation that increases with proximity to the crack. Further away from the surface, the degree of lattice rotation decreases.

Figure 53c shows ~120 nm-wide grain refinement region around a native grain boundary deep in the surface, shown as a purple band in the IPF map in **Figure 53d**. Similar to the grain boundary shown in **Figure 50a-b**, grain boundaries do not need to be the primary boundary where GBL forms to undergo grain refinement. The difference in the case of **Figure 53c-d** is that the grain boundary did not form high-angle refined grain boundaries. This is because plastic deformation occurred in the matrix as well as near the native grain boundary, resulting in less strain localization at the grain boundaries. A slip in the matrix was observed to induce ~5° crystal rotation several micrometers away from the sample surface, showing that the matrix can accommodate noticeable amount of plasticity.

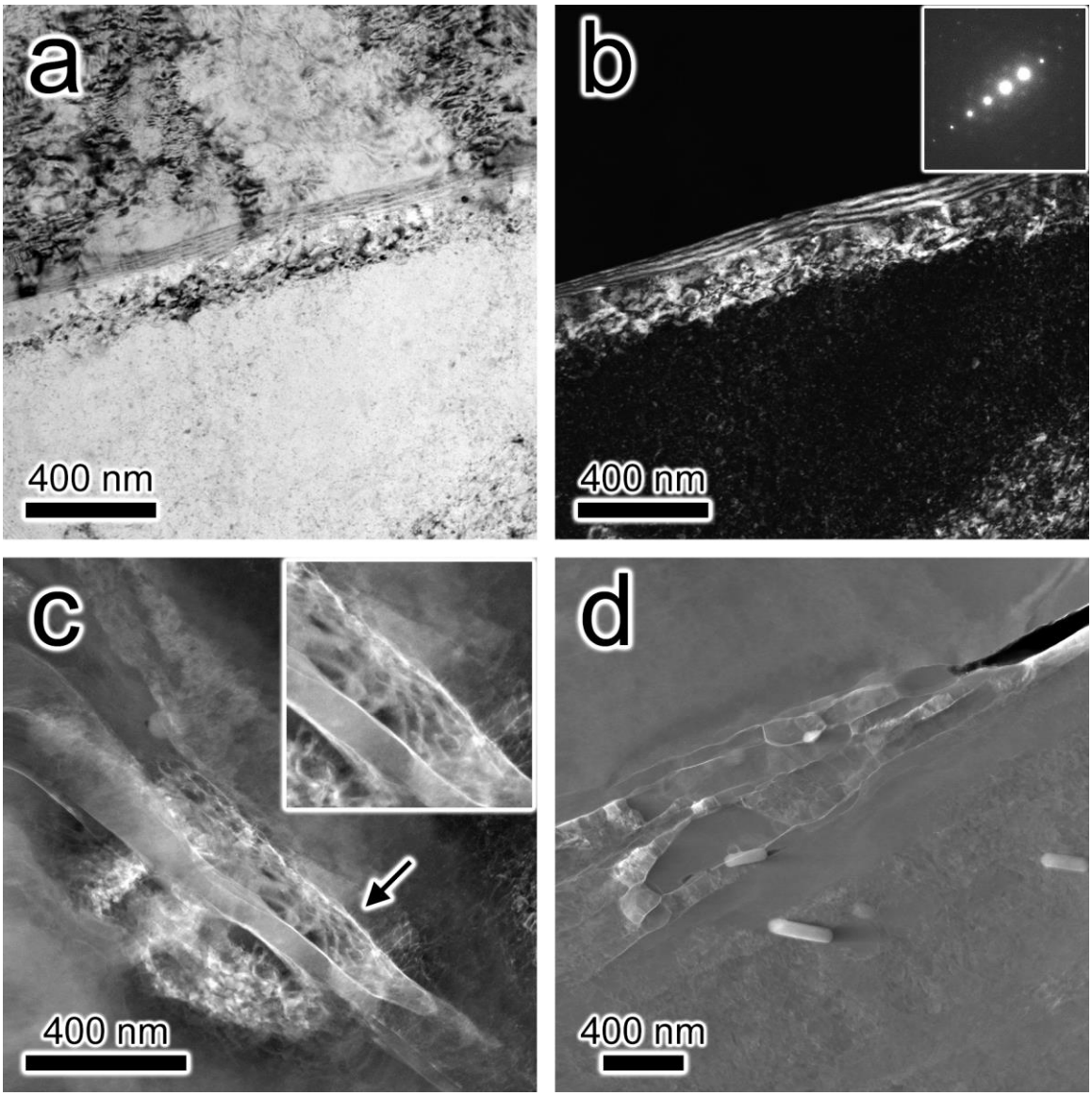

Figure 54. a) Bright field (BF) and b) dark field (DF) TEM and c-d) ADF STEM images of FIB lift-out specimens a T4 sample showing the progression of grain refinement. In the BF and DF TEM images, a dislocation forest is observed to form ~200 nm away from the grain boundary. ADF STEM images show that subsequently c) a refined grain boundary (black arrow and inset) can form, which develops into d) multiple layers with additional localized deformation. A surface crack is shown on the top right corner of image d.

Similar to the T6 FIB specimens, grain refinement was observed in every T4 lift-out specimen prepared from grain boundaries exhibiting plastic deformation. Depending on the degree of deformation, grain boundaries were at different stages of the refinement process. **Figure 54a-b** show BF and DF TEM images, respectively, of dislocations accumulating about 200 nm away from a native grain boundary located 8 μm below a GBL. The grain boundary appear to have experienced less tensile stress due to its distance from the surface but was not immune to it, therefore the dislocation structure shown in the TEM images is thought to be a snapshot of the early stages of grain refinement. Grain boundaries are inherently obstacles for dislocation movement and responds to dislocations with one of the following [114]:

1. Dislocation absorption into the boundary plane
2. Dislocation transmission into the neighboring grain
3. Dislocation absorption followed by transmission into the neighboring grain
4. Dislocation absorption followed by emission back into the original grain.

Dislocation forest forming at ~200 nm away from the native boundary is thought to be caused by entanglement between dislocations generated by localized shear at the grain boundaries and those gliding in the matrix.

The ADF STEM image in **Figure 54c** depicts a native grain boundary ~2 μm away from the GBL in the same FIB lift-out specimen. More dislocation content was evident near the native grain boundary than in **Figure 54a-b**, reinforcing the idea that the level of deformation in three-point bend tested samples increase with proximity to the sample

surface. Furthermore, dislocation forest developing into a refined grain boundary (**Figure 54c**, black arrow) was observed 100 nm away from the native boundary, likely as a result of experiencing higher tensile stress. The dislocation content within the refined grain shown in the inset suggests that it causes crystal rotations that can lead to high-angle grain boundaries. If the native grain boundary is exposed to higher localized stress that can result in surface cracks and tall GBL, it can have multiple "layers" of refined grains as illustrated in **Figure 54d**. Unlike T6 samples that contained grain refinement zones that had only a single layer of refined grains, localized grain boundary deformation is not restricted by the precipitate hardened matrix. The refined grain boundaries are more clearly defined at the center of the refined region while the ones on the fringes are fainter, which suggests that a new layer is formed after the previous one has reached a certain level of strain hardening.

4.3.6.3 Dispersoid-Dislocation Interaction

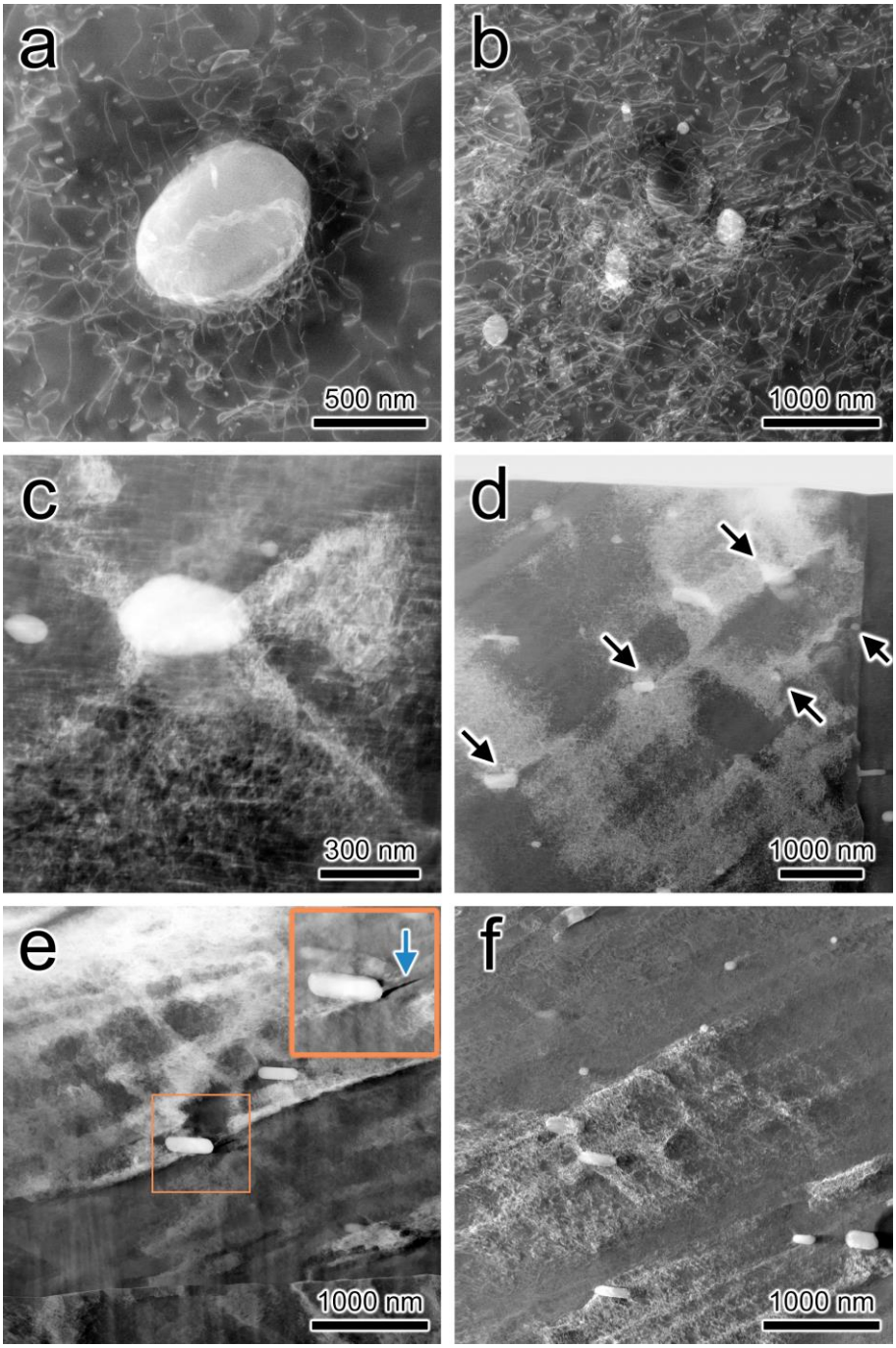

Figure 55. ADF STEM images showing a) dislocation accumulation around a dispersoid; b) dislocation entanglement around dispersoids; c) activation of multiple slips; d) slip band formation connecting dispersoids (black arrows); and e-f) dislocation cell formation.

As seen in **Figure 44** and **Figure 45**, dispersoids were observed to interact with the grain boundaries during the GBL formation process. ADF STEM images in **Figure 55** summarizes the microscale dispersoid interaction with dislocations. **Figure 55a-b** were taken from jet polished T4 from Alloy A; **Figure 55c-d** from a T6 Alloy C FIB lift-out specimen; and **Figure 55e-f** from T4 FIB lift-out specimens. The dislocations in **Figure 55a-b** originate from thinning the T4 sheets with SiC paper prior to jet polishing while those in **Figure 55c-f** are from three-point bending tests.

As previously mentioned in *Section 2.3.2*, dispersoids are unshearable second phase particles due to the crystallographic mismatch with the matrix that prohibits dislocations from transmitting through the particle-matrix interface (**Figure 55a-b**). As a result, dislocations accumulate around the dispersoids via the Orowan mechanism [3, 7], and this property has been attributed to the strain homogenizing effects of dispersoids in previous studies [3, 7, 9-12, 115]. In addition, slip bands have been observed to form around dispersoids **Figure 55c-d**, and often connecting them as a result of dislocations bowing.

As Dowling and Martin noted, the accumulated dislocations will work harden the active slip plane and cause slip to transfer to a different plane [11]. Combined with multiple active slip planes in the T4 matrix, dislocation cells can form around dispersoids **Figure 55e-f**. Cells were not observed in the T6 specimens due to the precipitate hardened matrix making plastic deformation difficult. The cell boundaries are evenly spaced apart, on the scale of approximately 500 nm apart.

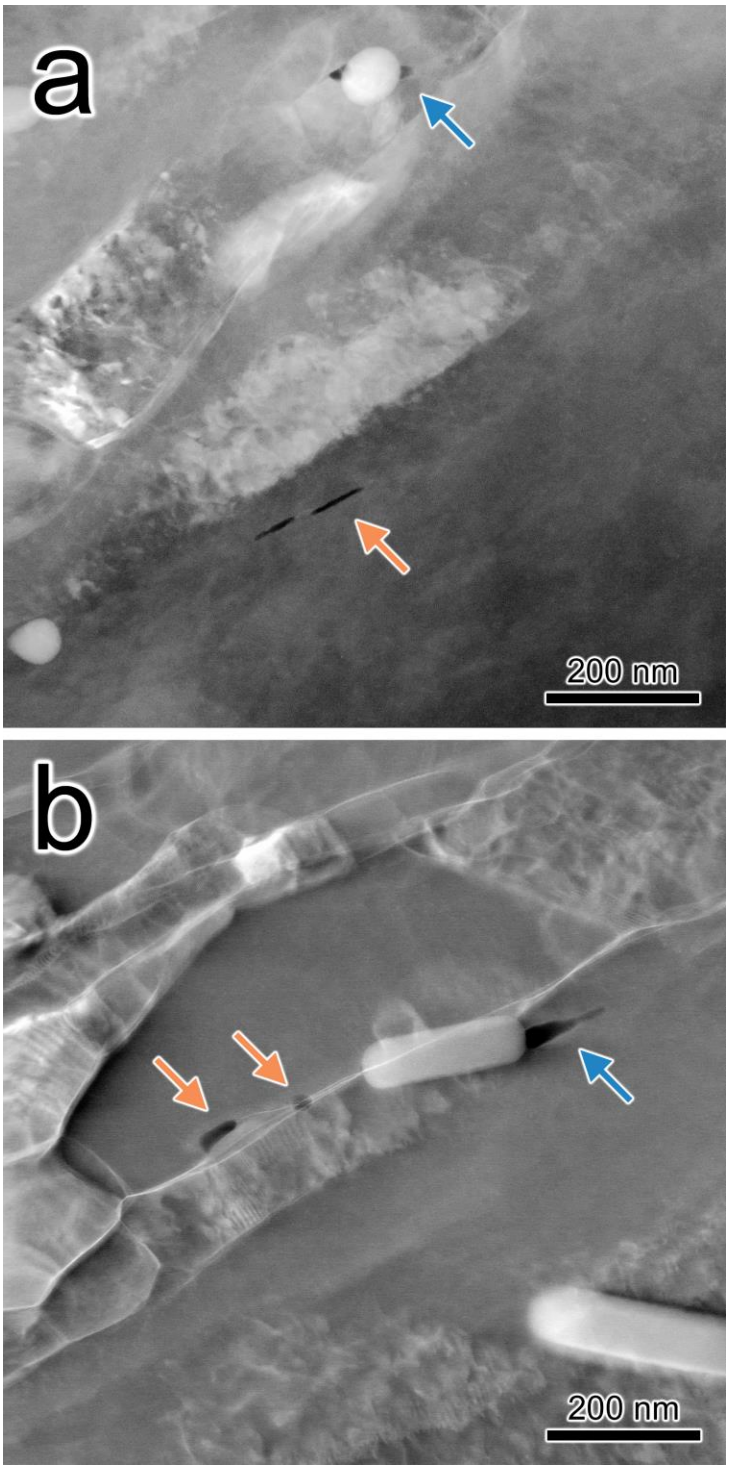

Figure 56. ADF STEM images of void formation (orange arrows) along a) slip and b) refined grain boundaries. The blue arrows highlight lateral cracks at the dispersoid-matrix interfaces. The lift-out specimens were prepared from Alloy a) B and b) C.

Microcracks were observed nucleating parallel to the slip bands (**Figure 55c** and **Figure 56b**) and refined grain boundaries (**Figure 56b**), which may explain the presence of subsurface voids under GBL, as shown in **Figure 48a** and **Figure 48d**. These voids are not very commonly observed because void nucleation via decohesion of particle-matrix interface is more energetically favorable than at the grain boundaries. Mechanism of decohesion involves dislocation accumulation and void formation near a rigid second phase particle [47, 116]. Along the same reasoning, the formation of microcracks in the STEM images may be explained by the mismatch of the degree of strain hardening at the slip band.

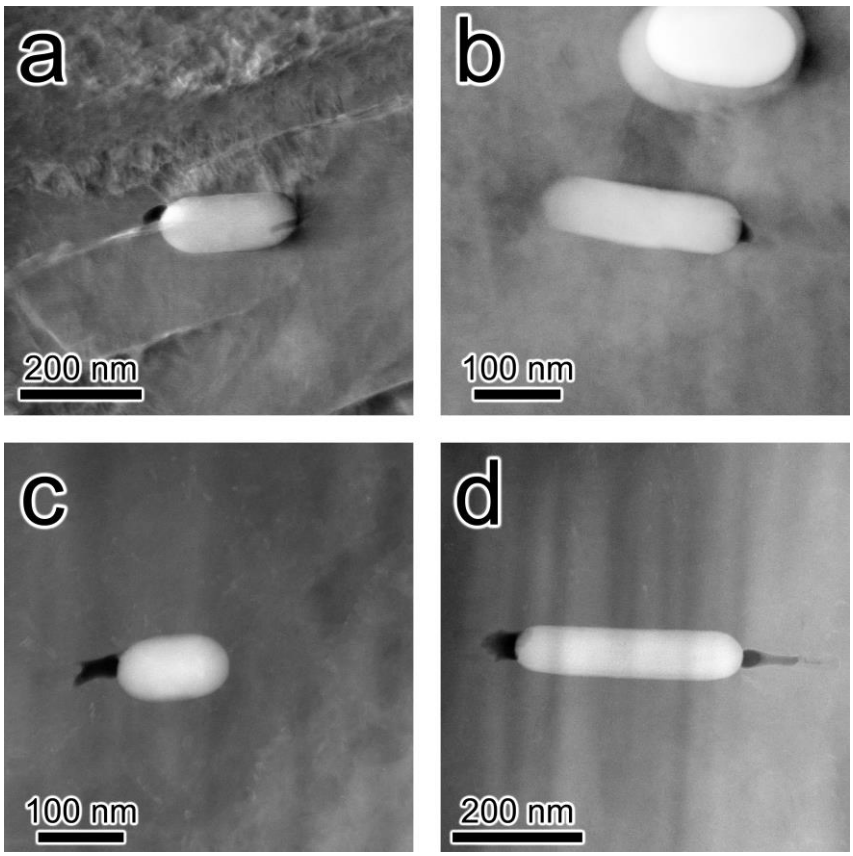

Figure 57. ADF STEM images of lateral microcracks around spherical (left) and cylindrical (right) from T4 (a-b) and T6 (c-d) samples.

Figure 57 shows that microcracks nucleating at the sides—parallel to the tensile stress—have been observed in both T4 and T6 FIB specimens extracted from GBL. FIB-induced damage did not cause this, as the directions of the cracks are perpendicular to the beam directions during the specimen preparation process. The most notable aspect of these microcracks is their direction: the cracks always grow laterally, parallel to the surface and the tensile stress direction. A similar observation has been made by Kikuchi *et al*. while studying void nucleation near grain boundary carbides in astroloy, a nickel-based superalloy [117]. They noted that although slip bands intersected with the carbides from all angles, only those impinged at the ends of the oblong carbides were associated with void nucleation. Their calculations revealed that when the surrounding matrix deformed plastically, it left residual shear stress profile that peaked at the ends of the carbides, which induced slip band formation at the tips of the carbides. The dislocation pileup at the bands that were responsible for void nucleation.

Although most of the dispersoids that exhibited lateral microcracks did not lie on any boundaries, they were observed in FIB specimen from heavily deformed regions, regardless of composition, temper, and morphology. It is thought that the microcracks were formed in a similar process as those near the grain boundary carbides, where dislocation accumulation facilitated by Orowan bowing induced void nucleation at the dispersoid.

4.4 Discussion

4.4.1 Grain Refinement

The surface SEM characterizations revealed grain boundaries were the primary crack nucleation sites, and grains Grain refinement has been observed in every FIB lift-out specimen that exhibited plastic deformation. In T6, the width of the refined grains indicated that it was limited to the PFZ around the native grain boundaries, and the grain refinement zone contained only one layer (200-500 nm). In contrast, the T4 matrix lacked hardening precipitates and therefore the grain refinement was not restricted to the PFZ, where multiple layers of refined grains constituted the grain refinement regions. The dislocation content (**Figure 52** and **Figure 54**); crystal rotation (**Figure 53**); high-angle refined grain boundaries (**Figure 50**); and rare instances of slip-induced void nucleation (**Figure 56**) shows that grain refinement is a consequence of localized grain boundary deformation from dislocation interaction. In this section, the mechanism of grain refinement will be explored with that arising from analogous processing methods.

Grain refinement also be observed after applying high strain during processing, such as cold rolling [118-125] or equal channel angular extrusion (ECAE) [73, 126-129]. Grain size of industrial-grade as-cast alloys is fairly large on the order of 100 μm in diameter, and to increase strength and toughness, the grain sizes are reduced by application of high strain using the techniques mentioned above.

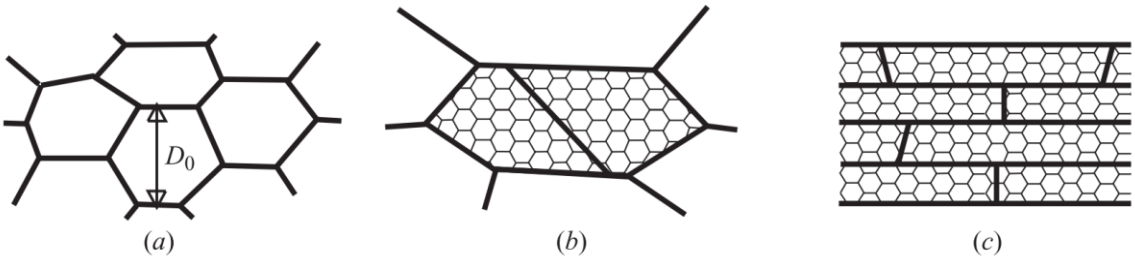

Figure 58. Schematic of grain refinement process with increasing strain: a) initial grain structure; b) subgrain and grain subdivision; and c) alignment of high-angle grain boundaries [126]. Reprinted with permission from The Royal Society.

Cold rolling involves alloy sheets passing through rollers at low temperatures—below recrystallization temperature and often at room temperature—to induce work hardening and reduction in thickness. A clear reduction in grain size is observed after rolling (**Figure 58c**), and Hughes and Hansen concluded that the most of the observed high angle boundaries are not native grain boundaries: rather, they are created as a result of grain subdivision during plastic deformation [130].

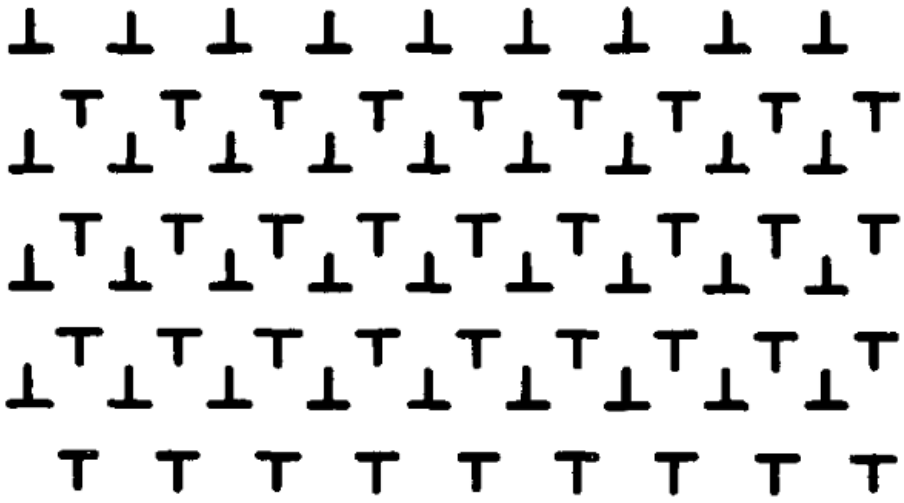

Figure 59. A simple Taylor lattice [131]. Reprinted with permission from Elsevier.

During cold rolling, cell-like dislocation structures initially develop as a result of multiple active slip systems [120]. Hughes observed that the dislocations were arranged into Taylor lattices (**Figure 59**) with multiple Burgers vectors and containing alternating misorientation along the (111)-family slip planes [131, 132]. The organization of dislocations into Taylor lattices lowers the overall energy compared to a randomly-distributed dislocation configuration [132]. These dislocation cell boundaries subdivide the native grain into sub-granular regions, and with further deformation, the crystal lattices in each cell rotate themselves to a stable final orientation [120]. High-angle grain boundaries are developed after large deformation since the stable final orientation for each cell may be different than its nearest neighbors. The subdivision is an energetically favorable process because offers a means to accommodate plasticity using fewer slips than required by the Taylor criterion [119, 124].

A similar behavior is thought to be responsible for grain refinement in AA6451-T6 and -T4. Two driving forces are attributed to this phenomenon: localized grain boundary deformation and crystal rotation. Grain refinement is only observed around native grain boundaries, where deformation was localized. When alloys with high stacking fault energy—such as aluminum—are subjected to large strain, dislocations can assimilate via dynamic recovery to form low-angle grain boundaries [126, 127]. During three-point bending, these boundaries form cells that can experience large crystal rotation with increasing strain. The degree and final crystallographic orientation of each cell depends on a variety of factors such as orientation of neighboring cells and grain boundary, and this difference results in formation of high-angle refined grain boundaries (orange arrows in

Figure 50a). This process is summarized in **Figure 54**, where dislocations initially accumulate around a native grain boundary (**Figure 54a-b**), followed by crystal rotation of cells around the native grain boundary (**Figure 54c**) forming high-angle grain boundaries (**Figure 54d**).

To recapitulate, the PFZ offers an approximately 300 nm-wide soft matrix where dislocations can be generated with relative ease in T6 alloys. These dislocations accumulated to form cell boundaries (**Figure 52a**, inset), and with additional strain, the cells reorient themselves to accommodate plasticity. Similarly, grain refinement is observed around native grain boundaries in T4 where GBL formation remains the primary crack nucleation sites. Multiple layers of grain refinement are observed due to the lack of precipitate hardened matrix restricting localized grain boundary deformation. Even without grain refinement, T4 exhibited increased crystal rotations with proximity to surface cracks and GBL (**Figure 53b**). Although the grain is not refined, this results in large misorientation across slip bands that mimics a medium-angle grain boundary. The combination of deformation around grain boundaries and rotation of crystal lattices as a response to applied strain during three-point bending facilitates grain refinement in AA6451-T6 and -T4.

4.4.2 Dispersoid Effects on Grain Refinement

Previous research on the effects of dispersoids on grain refinement have yielded somewhat conflicting results. Ning and Jiang showed that when compared to a dispersoid-free alloy of similar composition, Al-Mg-Mn alloys containing 50-100 nm-wide incoherent

Al_3Zr dispersoids produced finer grains when subjected to equal channel angular pressing (ECAP) at 350°C [133]. The Al_3Zr particles reduced the rate of static recovery and pinned refined grain boundaries during passes through ECAP at elevated temperatures, whereas the dispersoid-free samples experienced recovery and recrystallization during the same process. Consequently, the samples containing dispersoids exhibited slightly smaller grain sizes and increase in strength. Similarly, Nikulin *et al.* reported that incoherent Al_6Mn dispersoids facilitated grain refinement in Al-Mg-Mn during passes through ECAE after exposure to 300°C isothermal die [13]. These studies, however, do not correlate dispersoids to the grain refinement process itself: instead, dispersoids act as stabilizers for refined grain boundaries at elevated temperatures that hinders grain boundary movement that inhibits refined grains from growing. Numerous sources reported that dispersoids are a critical component for thermal stability of ultrafine grains at elevated temperatures [134-141]. In a dispersoid-free microstructure, there is no barrier to grain boundary migration at high temperatures, resulting in significant grain growth. In contrast, sub-micron grains are retained in alloys containing dispersoids because dispersoids restrict movements of grain boundaries through Zener pinning [13, 73, 142]. Although these studies associate well-developed grain refinement to dispersoids, they do not correlate the particles to mechanical deformation and therefore are insufficient explanations for grain refinement in AA6451.

A more relevant investigation was conducted by Barlow *et al.*, who studied the effects of nanoscopic alumina particles on the grain refinement in cold rolled commercially-pure aluminum [143]. They observed that the alumina particles were located on refined boundaries and dislocation cells. They concluded that alumina particles

facilitated dislocation nucleation even at low strain, and dislocation jogs produced during cold rolling formed high vacancies that increased dislocation mobility. The abundance of mobile dislocations accelerated the recovery process and by corollary, the grain refinement process. The crucial assumption for their explanation relied on dislocation generation at alumina particles, which assume the shapes of platelets that are 10 nm thick and 50-100 nm wide. However, the morphology, size, and aspect ratios of dispersoids in AA6451 are different from the alumina platelets, and the dislocations accumulating around them (**Figure 55a-b**) originate from the matrix as a result of plastic strain.

On the other hand, Apps *et al*. and Berta *et al.* observed that the Al-0.2 wt% Sc binary alloy contained ~20 nm-wide coherent Al_3Sc dispersoids that retarded the formation of subcellular structure, thereby delaying grain refinement during ECAE [73, 144]. Both studies attributed dispersoid-induced strain homogenization for inhibiting shear band and cell boundary formation, which is crucial to producing high-angle refined grain boundaries.

Taking into account the complexity of both seemingly conflicting results, the dispersoid effects on grain refinement can be categorized based on the level of applied strain. At low strain, dislocations nucleate and glide as a response to plastic deformation. Because of the strain homogenizing characteristic of dispersoids, dislocations are distributed evenly around dispersoids, and the dispersoids around grain boundaries suppress dislocations from assimilating into a cell boundary, effectively delaying grain refinement. The dispersoids essentially stabilize the native grain boundaries by inhibiting slip localization, which is why they are sometimes observed to be lodged at grain boundaries underneath GBL (**Figure 44a** and **Figure 45a**).

This, however, does not mean dispersoids are free from strain build up. Dislocations continue to accumulate around the particles via Orowan mechanism because of the incoherent dispersoid-matrix interface. With higher levels of applied strain, these dislocations are rearranged to form boundaries as low-energy structures [143], and the unshearable dispersoids serve as nucleation sites for cell boundaries. Because of Zener pinning [13, 73, 142], the cell boundaries rarely move away from the dispersoids. This explains why many of the dispersoids in **Figure 50c**, **Figure 51**, and **Figure 54d** intersect with refined grain boundaries. Grain refinement, which appears to be a necessary precursor to crack initiation, occurs at higher strain and delays fracture during three-point bend tests.

This could be one explanation of how increase in dispersoid content can improve the bendability of AA6451 [87], although development of strong cube texture may have a stronger effect on its bendability [145, 146]. Grain refinement at native grain boundaries emphasizes the influence of dispersoid density over dispersoid density in the matrix. This is in agreement with earlier studies compiled by Vasudévan and Doherty, who concluded that the area fraction of grain boundary particle is the most important parameter in intergranular ductile fracture [86]. Therefore, dispersoids ultimately improves the bendability of AA6451 by delaying grain refinement at the grain boundaries but appear to be associated with the refinement process because their unshearable interface promotes cell boundary formation.

4.4.3 GBL Formation

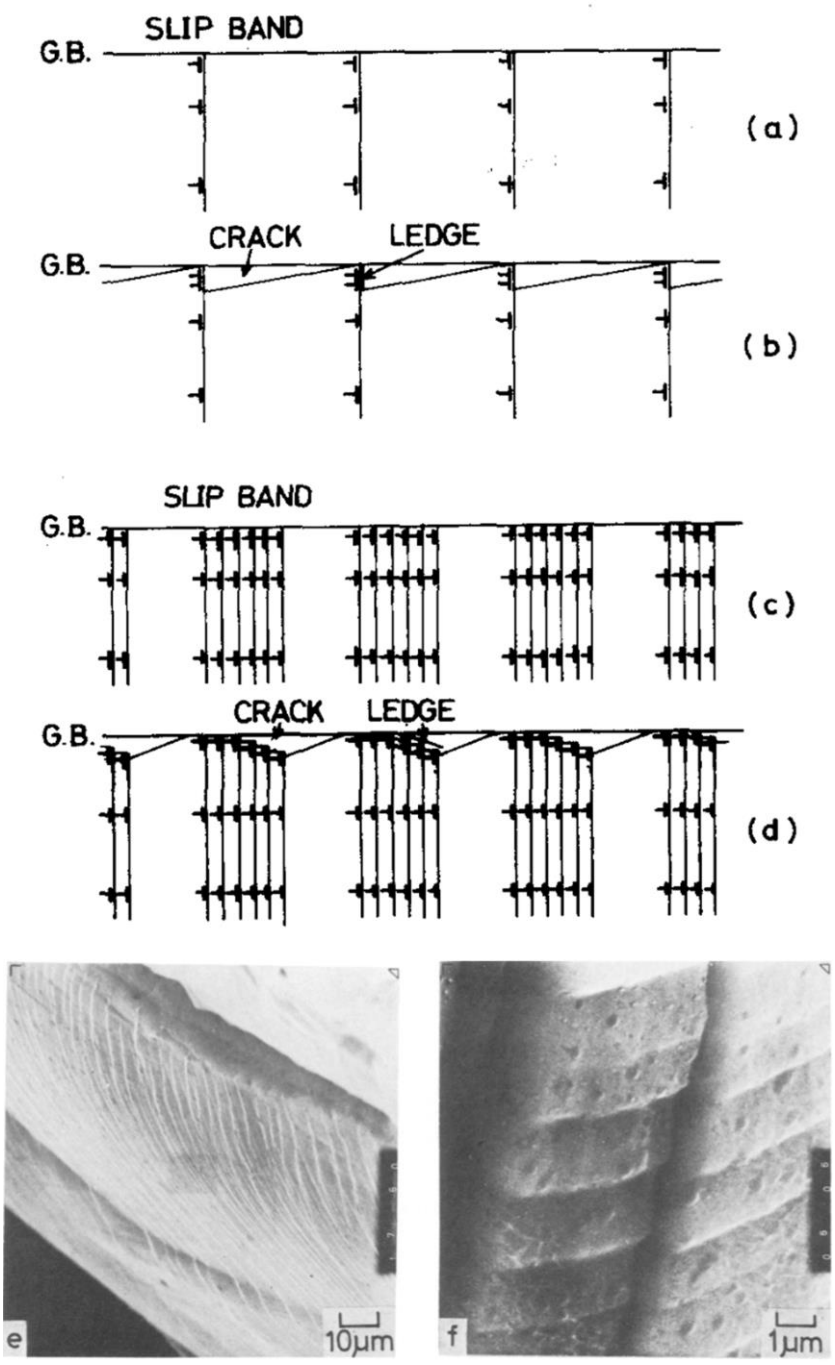

Figure 60. Schematic of ledge formation by a-b) one slip band and c-d) multiple slip bands on fracture surface grains in fatigue tested Al-Zn-Mg alloy [147]. e-f) Examples of ledges on grain surfaces on the fracture surface. Reprinted with permission from Royal Society.

GBL were observed as the primary crack nucleation sites in T6 (**Figure 44a-b**) and T4 (**Figure 45a-b**). The GBL are a strong evidence of localized plastic deformation around grain boundaries. Kawabata and Izumi also observed ledges (**Figure 60e-f**) on the fracture surface of fatigue-tested Al-Zn-Mg [147]. The schematic of the ledge formation mechanism is summarized in **Figure 60a-d**. They explained that dislocation in the slip band reacts with the grain boundary to produce a ledge height equal to the magnitude of the Burgers vector. The ledge height grows as it absorbs more dislocations. During fatigue testing, a macrocrack grows when the ledge height at the crack tip achieves critical height to produce a microcrack that can coalesce with the macrocrack. Although the ledges in Al-Zn-Mg grew perpendicular to the grain surface instead of parallel to the grain boundary, the ledge formation mechanisms are thought to be similar.

In AA6451-T6, plastic strain is localized to the soft PFZ, and when the dislocation glide plane matches the orientation of the native grain boundary within a certain angle, the dislocations are free to reach the surface (front plane in **Figure 26**). The ledges are created as a result of a large number of dislocation absorption at the surface. Since one grain appears to "elevate" relative to its neighboring grain, dislocation movement to the surface must be easier in one grain than the other. In other words, a combination of the orientation of grain boundary with respect to the tensile loading axis and the orientation of the slip planes that give dislocations access to the free surface dictate the creation of ledges at grain boundaries. It is thought that the cracks in T4 follow a similar process, but the area around the native grain boundaries conducive to ledge formation is not restricted by precipitates.

4.4.4 Crack Initiation Mechanism

For both T6 and T4, GBL were sites where most cracks appeared to nucleate. This behavior is quite different from previous studies on ductile alloys where fractographs suggested that fracture initiated in the matrix via void nucleation by either second phase particle fracture or decohesion at the particle-matrix interface [6, 37, 44, 45]. Several instances of intergranular crack initiation have been reported in Al-Si-Mg alloys, especially those in peak aged conditions [9, 42, 148, 149]. In these studies, intergranular fracture was attributed to strain concentrations at grain boundaries, which are expected to be larger in large grains; precipitate shearing at boundary structures; matrix softening in precipitate free zones near grain boundaries; or constituent particle-induced strain concentration. These, however, cannot explain the crack initiation at grain boundaries observed in this study. On the contrary, grains were refined near native grain boundaries; hardening precipitates were observed within the matrix; and cracks nucleated from cracked constituent particles did not extend into the matrix. An alternative explanation is required to explain the crack initiation behavior of bend tested AA6451.

According to cross-section (**Figure 48a**, inset) and TKD analyses (**Figure 50a**) of T6, surface cracks do not exactly coincide with the native grain boundaries. Rather, it appears cracks are nucleated at the interface between the refined grains and the precipitate hardened matrix. Therefore, the strain hardening effects of cell boundaries and refined grains must be taken into account.

The cell boundaries that constitute the areas around native grain boundaries during the early stages of bending tests hinder dislocation movement. Kuhlmann-Wilsdorf explored the implications of cell boundaries formed by glide dislocations on work hardening [131]. Glide dislocations make up cell boundaries, and they maintain their mobility and could bow out supercritically, and therefore, the cell boundaries are mobile. This property distinguishes cell boundaries from grain boundaries that provide unyielding obstacles to dislocation movement. Therefore, the dislocation interaction with cell boundaries are different, resulting in deviation from the Hall-Petch relationship. The cell boundaries hinder dislocation glide by reducing the mean free dislocation path, which can be approximated as the cell size (D_{cell}). Plastic strain occurs when the local shear stress overcomes critical shear stress, which can be expressed as

$$\tau_y(D_{cell}) \approx \frac{constant}{D_{cell}^{1.2}} \tag{8}$$

The derivation can be found in Kuhlmann-Wilsdorf's work cited above. Therefore, as the region near the native grain boundaries undergo grain refinement, the flow stress increases, work hardening the refinement zone [127].

The change in flow stress also influences the fracture toughness (K_{IC}). Although slip bands in the SEM images show that plastic deformation occurs in the matrix as well as around grain boundaries for both T6 and T4, the fact that the vast majority of the cracks are initiated at the grain boundaries suggests that the severest of strains are localized at

grain boundaries. Assuming that plastic deformation is almost entirely limited to the PFZ, Gräf and Hornbogen argued that the fracture toughness can be modeled by

$$K_{IC} = \sqrt{CE\varepsilon_{cPFZ}\sigma_{PFZ}n_{PFZ}^2\frac{d_{PFZ}}{D_{grain}}} \quad (9)$$

where C is a constant; E is the Young's modulus; ε_{cPFZ} is the critical strain at which crack propagation occurs; σ_{PFZ} is the flow stress in PFZ; n_{PFZ} is the work hardening exponent of the PFZ; d_{PFZ} is the PFZ width; and D_{grain} is the grain size [150, 151]. Although this approximation may deviate for T4 because of the increased contribution of plastic strain in the matrix, it is thought that the number of GBL-induced cracks justifies using the assumption. The increase in τ_y results in an in an increase in flow stress (σ_{PFZ}), and therefore decreases the likelihood that cracks can nucleate in the grain refinement region, which coincides with the PFZ. Gräf and Hornbogen's model also suggests that increase in toughness can result from increase in volume fraction of PFZ, which may be engineered by changing the heat treatment conditions.

Therefore, crack initiation at grain boundaries are preceded by GBL formation, an artifact of localized deformation at grain boundaries. During GBL formation, grains are refined around the native grain boundaries as plastic strain elevates one grain relative to the other, forming a ledge between the neighboring grains. The grain refinement strain hardens the refinement zone, thereby making crack initiation in the refinement zone difficult. Instead, cracks are formed at the boundary between the refinement zone and the precipitate hardened matrix.

4.4.5 Dispersoid Effects on Slip Formation

As previously mentioned in *Section 4.4.2*, dispersoids near grain boundaries homogenize slip at low strains but provide cell boundary nucleation sites at high strain. Dispersoids in the matrix have a similar effect on slip band formation. At low level of applied strain, dislocations are generated in the matrix and freely glide through the T4 matrix until they meet another microstructural defect such as a dispersoid. Because of strain homogenization, dislocations will strain harden the active slip plane and promote subsequent dislocation accumulation on a different plane. At higher levels of strain, the dislocations piled up around dispersoids develop into slip bands (**Figure 61**). Under the right conditions, long slip bands can form that connects multiple dispersoids, as shown in **Figure 61b**.

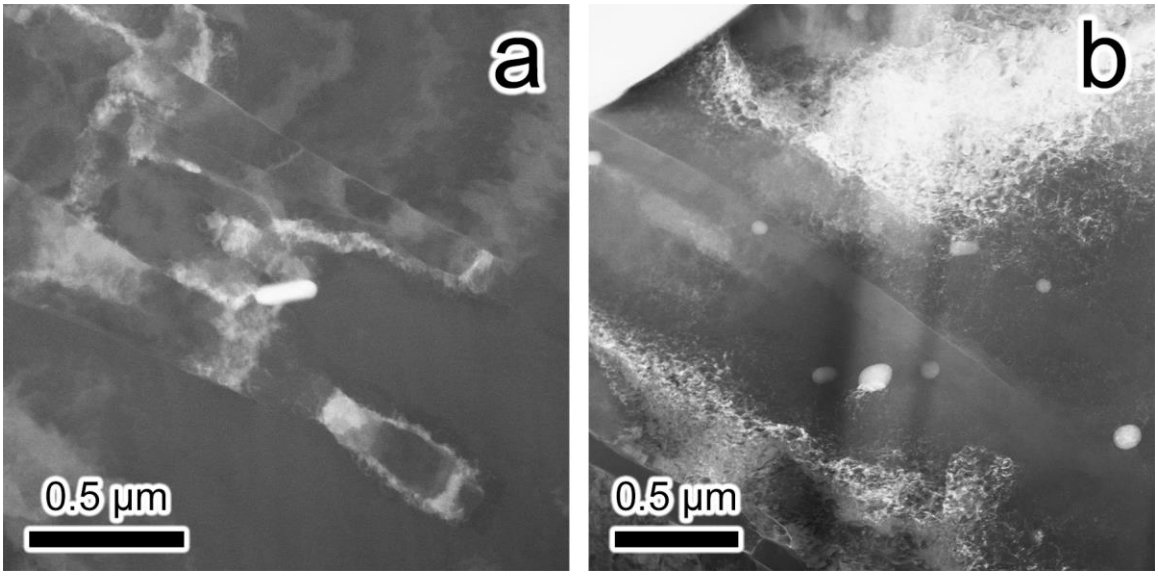

Figure 61. Magnified ADF STEM images of FIB specimens from **Figure 53** showing slip band formation around dispersoids in T4 matrix. The two dark vertical lines in image b are artifacts of FIB during milling.

Because of the ductility of T4 alloys, multiple slip systems are active. At depths of 5-6 μm from the surface, dislocations from active systems accumulate around dispersoids, resulting in net-shaped dislocation cells, as illustrated in **Figure 55e-f**. The periodic spacing between dislocation accumulations was between 400 and 550 nm and shows the slip homogenizing nature of dispersoids. This result is consistent with previous TEM studies that found improved fracture toughness in alloys containing dispersoids [11, 115].

Although slip bands are not as prominent as those in T4, they can also form in the T6 matrix. Dislocation movement is obstructed by Mg_2Si precipitates. When the flow stress reaches a critical value, the dislocations will shear through the precipitates and locally soften a slip plane, creating a path energetically favorable for dislocation movement [11]. This explains the sharp rise in flow stress at the start of the three-point bend tests, and slip is preferentially formed around dispersoids in the same manner as described above. Examples of shear bands can be seen in **Figure 55c-d**. Although dislocation cells similar to the one shown in **Figure 55e-f** were not observed, multiple active slip systems (**Figure 55c**) and long shear bands that connected dispersoids (**Figure 55d**) were observed.

A crystal rotation boundary was clearly observed in **Figure 50c**. The boundary is a noteworthy result of a combination of several factors. First, the IPF map (**Figure 50a**) shows that the native grain is comprised to two halves that rotated into different orientations. This grain is described as "unstable" because it cannot maintain its initial average orientation with increasing strain, which is caused by the orientation of the slip planes that favors activation of multiple slip systems [120]. During the three-point bend test, each half of the grain is rotated to its respective stable final orientation. The location

and orientation of the rotation boundary is determined by the surface crack and presence of dispersoids, which are the second and third factors, respectively. Propagation of the surface crack along the same grain boundary may be energetically unfavorable since it involves a drastic change in direction. The fact that the rotation boundary is parallel to the crack propagation direction indicates that the stress profile ahead of the crack tip facilitated significant localized deformation that could have extended the crack into the unstable grain. The third and last factor is the presence of several dispersoids that aligned with the crack growth direction. Compared to the diffuse clusters of dislocations that formed shear bands in **Figure 55c-d**, **Figure 50c** shows a well-developed boundary that resembles a grain boundary. This indicates that the stress profile ahead of the crack tip was high enough to produce a medium-angle grain boundary from accumulated dislocations around the dispersoids. In summary, the dispersoids were positioned in locations where the accumulated dislocations assimilated and developed into a grain boundary from highly localized plastic deformation ahead of a surface crack.

Therefore, it is important to note that although dispersoids homogenize strain and slip at low strains, they can also serve as potential sites for slip band formation at high strain. Despite their beneficial properties that delays grain refinement and slip band formation that leads to higher ductility and fracture toughness, significant localized plasticity buildup around dispersoids can facilitate slip band formation.

4.5 Conclusion

The effects of dispersoids on the deformation behavior and crack initiation mechanism of three-point bend tested AA6451-T6 and -T4 were investigated using multiscale electron microscopy. In addition, samples with varying Mn and Cr were compared to observe the influence of dispersoid density on the microstructure.

Although all the samples exhibited strong cube texture, the alloy containing the highest Mn and Cr content exhibited the strongest cube texture. No noticeable signs of change in grain size distribution or PFZ width was detected. Dispersoid densities in the matrix and on grain boundaries were the lowest in alloys that contained the lowest Mn content. Dispersoid densities did not increase much with addition of Cr.

Mesoscale electron microscopy of the bend tested T6 and T4 revealed that cracks mainly nucleate at grain boundaries. First, GBL are formed, followed by crack initiation at grain boundaries. Cracks can transition to transgranular and propagate into the neighboring grains once they grow beyond a critical size. The orientation of the grain boundaries with respect to the tensile load axis was found to be the most important microstructural factor that dictated where GBL formed: those oriented perpendicular to the axis were resistant to GBL formation. No correlation between the misorientation angle across grain boundaries and GBL was detected.

Although slip bands were observed for both tempers, only those in T4 developed into small surface cracks because of the lack of hardening precipitates. Unlike in the uniaxial tension tests, constituent particles are not the primary failure initiation sites.

Cracks can be nucleated by constituent particle cracking, but none of them extended into the surrounding matrix.

Microscale electron characterization of FIB lift-out samples taken from various grain boundaries revealed that grain refinement around native grain boundaries were associated with GBL formation. For T6, grain refinement was localized to the PFZ around native grain boundaries. Dislocation accumulation around native grain boundaries followed by assimilation into cell boundaries that developed into higher angle boundaries resulted in refined grain boundaries. Dispersoids delayed the grain refinement process via strain homogenization at low strains but served as cell boundary nucleation sites at higher levels of strain.

During grain refinement, plastic deformation results in production of GBL where the surface of one grain is elevated relative to the other. The ledge formation involves movement of dislocations to the free outer surface along the native grain boundary. The orientation of the grain boundaries relative to the tensile axis and the orientation of the slip plane in one of the two grains dictate which grain boundaries will produce ledges.

The surface cracks did not propagate along the native grain boundary: instead, they propagated between the matrix and the grain refinement zone. This results from increase in flow stress associated with decrease in cell size, which ultimately increases the fracture toughness of the grain refinement zone.

Multiple active slip systems were observed in both T6 and T4 samples. It was concluded that while dispersoids homogenize slip at low level of applied strain, the

unshearable nature of the particles facilitated the formation of slip bands. With the right set of conditions—strain concentration ahead of a crack tip; orientation of slip planes that promotes different stable final orientations for different parts of the grain; and alignment of dispersoids along the crack propagation direction—the dispersoid-induced slip band can develop into a medium-angle grain boundary.

CHAPTER 5. EFFECTS OF DISPERSOIDS ON CRACK PROPAGATION BEHAVIOR IN DEEP DRAWN AA3XXX

5.1 Introduction

The objective of this study is to investigate the effects of dispersoids on crack growth behavior in aluminum alloys. AA3xxx, an important aluminum alloy in the packaging industry, containing microcracks from deep drawing, ironing, and necking was chosen for this study. As discussed in *Section 2.2.1*, deep drawing is a widely used method of producing cans and bottles for the beverage industry. Due to the high plastic strain and high strain rate the alloys experience during the process, 1 out of every 50,000 cans was defective, according to a report in 1994 [27]. Although the exact current figures are undisclosed, the defect rate is thought to have decreased noticeably with the innovation in the last 16 years.

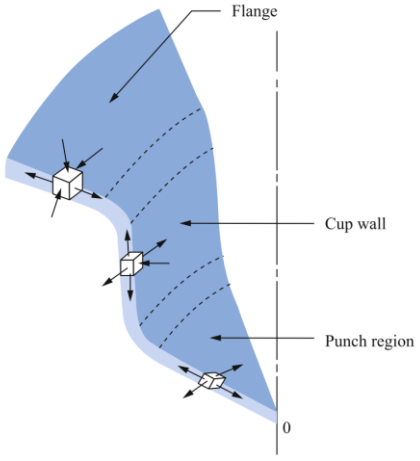

Figure 62. Stress states in a deep-drawn cup [36]. Reprinted with permission from Springer Nature.

Though the variety of defects abound (**Figure 8**), one of the biggest concerns of all is critical failure caused by process-induced microcracks growing above a critical size. The areas most prone to crack initiation are the can walls that experience high plastic strain through deep drawing and the tapered bottle top that has been necked to reduce the diameter [34, 152, 153]. The walls are susceptible to cracking from the intense tensile and shear stress the deep drawing and ironing (D&I) process induces on them [36]. After D&I, the tops of the walls are trimmed and further deformed during necking, inducing more damage. Preventative measures against microcrack formation ranges from optimizing process-related parameters to engineering the microstructure.

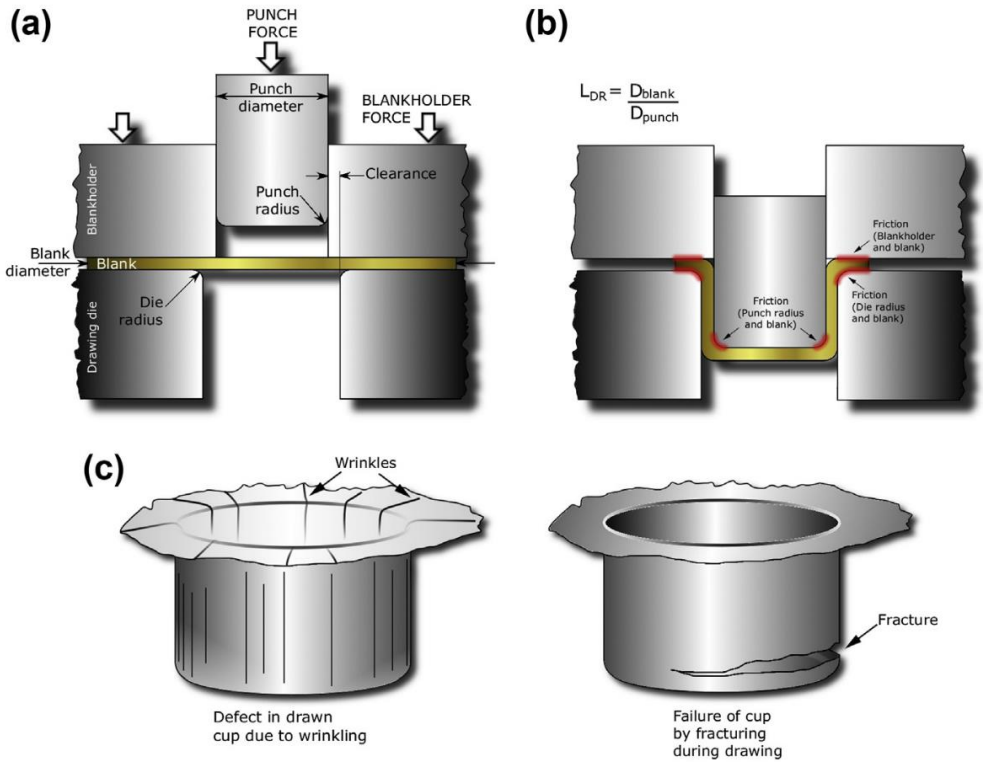

Figure 63. Illustrations of a) the deep drawing process; b) areas where the friction has significant influence; and c) commonly observed defects in the drawn parts [34]. Reprinted with permission from Elsevier.

Aside from the obvious parameters such as loading rate and geometry, optimization of processing parameters include controlling the friction between the metal sheet and the blank holder surface (highlighted red in **Figure 63**). For fine-grained thin sheets, damage caused by friction remains one of the most crucial limiting factors that determine the shape and size of the drawn parts [34].

The guiding principle for microstructure design is to increase formability by facilitating homogenous strain distribution during the drawing process. This involves tailoring the microstructure to have high strain-hardening (*n*) exponent and positive strain rate sensitivity (*m*) [36]. High *n* facilitates even strain distribution because additional plastic strain tends to areas with low strain. A material with positive *m* prevents further strain on areas with increased flow stress caused by high local strain rate. These attributes are desirable for strengthening the wall during the forming process while detrimental for flanges because it prevents further drawing. Therefore, caution must be exercised to balance the material properties to optimize the deep drawing process. One method of increasing the strain homogenization behavior is by engineering the dispersoid density, which was discussed in *Section 2.3.2*. In addition, alloys with fine grains and superplastic flow can help prevent cracking at the punch corner and flange-wall interface (highlighted red in **Figure 63**).

The complicated challenges that the deep drawing poses are also affected by maintenance of the manufacturing instruments. Moon *et al*. observed that temperature of the tools influence the drawability of AA1050 [154]. Tenner *et al.* [153] noted that the wall of a deep drawn AA6014 without any lubrication produced cracks where it came into

contact with the die and residual Al particles [34], illustrating that preventing failure in defect-prone regions requires consideration of not only mechanical loads, but also miscellaneous parameters.

In this chapter, microcracks at various stages of the D&I and necking of AA3xxx have been characterized using STEM, EDX, and TKD coupled with the dictionary approach for indexing Kikuchi patterns. Various grain boundary character such as grain boundary misorientation angles; grain boundary length; and presence of dispersoids have been studied to characterize microcracks. Furthermore, the effects of dispersoids on crack propagation are also considered. The challenges and their possible solutions of TKD, a relatively new technique for analyzing crystallographic orientation, are also discussed.

5.2 Experimental Procedures

The bulk samples investigated were taken from two different stages in the manufacture of an aluminum bottle from AA3xxx alloy sheet using processes of drawing and ironing followed by multi-stage die necking. As mentioned in **Table 4**, "ironed sample" was from the wall of the initial cylinder formed from drawing and ironing. The "necked-1 sample" is prepared approximately midway through the sequence of necking passes. The "necked-2 sample" was from a later stage in the forming process after more than double the number of passes than necked-1. The bulk samples were then cut into smaller pieces using metal shears and attached to one-inch diameter scanning electron microscopy (SEM) stubs with Crystalbond^{TM}. Characterization of the bulk sample surface

was performed using a TESCAN MIRA3 scanning electron microscope with 10 kV acceleration voltage. Focused-ion beam (FIB) machining was used to extract lamellae for scanning transmission electron microscopy (STEM) characterization from surface cracks using a FEI Nova Nanolab 200 FIB/SEM. One lift-out sample was prepared from each of the samples. STEM and energy dispersive X-ray spectroscopy (EDX) data were collected using a FEI Tecnai F30 transmission electron microscope with 300 kV acceleration voltage. Annular dark field (ADF) STEM images were taken using camera length of 250 mm, and bright field (BF) STEM images were taken with a camera length of 2000 mm. Transmission Kikuchi diffraction (TKD) patterns were collected using the TESCAN MIRA3 scanning electron microscope at 25 kV at a sample tilt angle of 0° and scan step size of 20 nm.

The TKD patterns were found to be of low quality due to the heavily deformed state of the Al matrix. In order to clearly resolve the grain and grain boundary structures, the dictionary approach was used to index the collected patterns. OIM Analysis software from EDAX/TSL was used to determine grain boundary misorientation angles and generate microstructure maps.

More specific details and information about the experimental procedures can be found in the following sections: *3.1.4 AA3xxx*; *3.1.5 Focused Ion Beam* ; *3.3.1 Scanning Electron Microscopy*; *3.3.3 Electron Backscatter Diffraction and Transmission Kikuchi Diffraction*; *3.3.4 Dictionary Approach*; and *3.3.5 Scanning Transmission Electron Microscopy*.

5.3 Results

5.3.1 Initial Microstructural Characterization

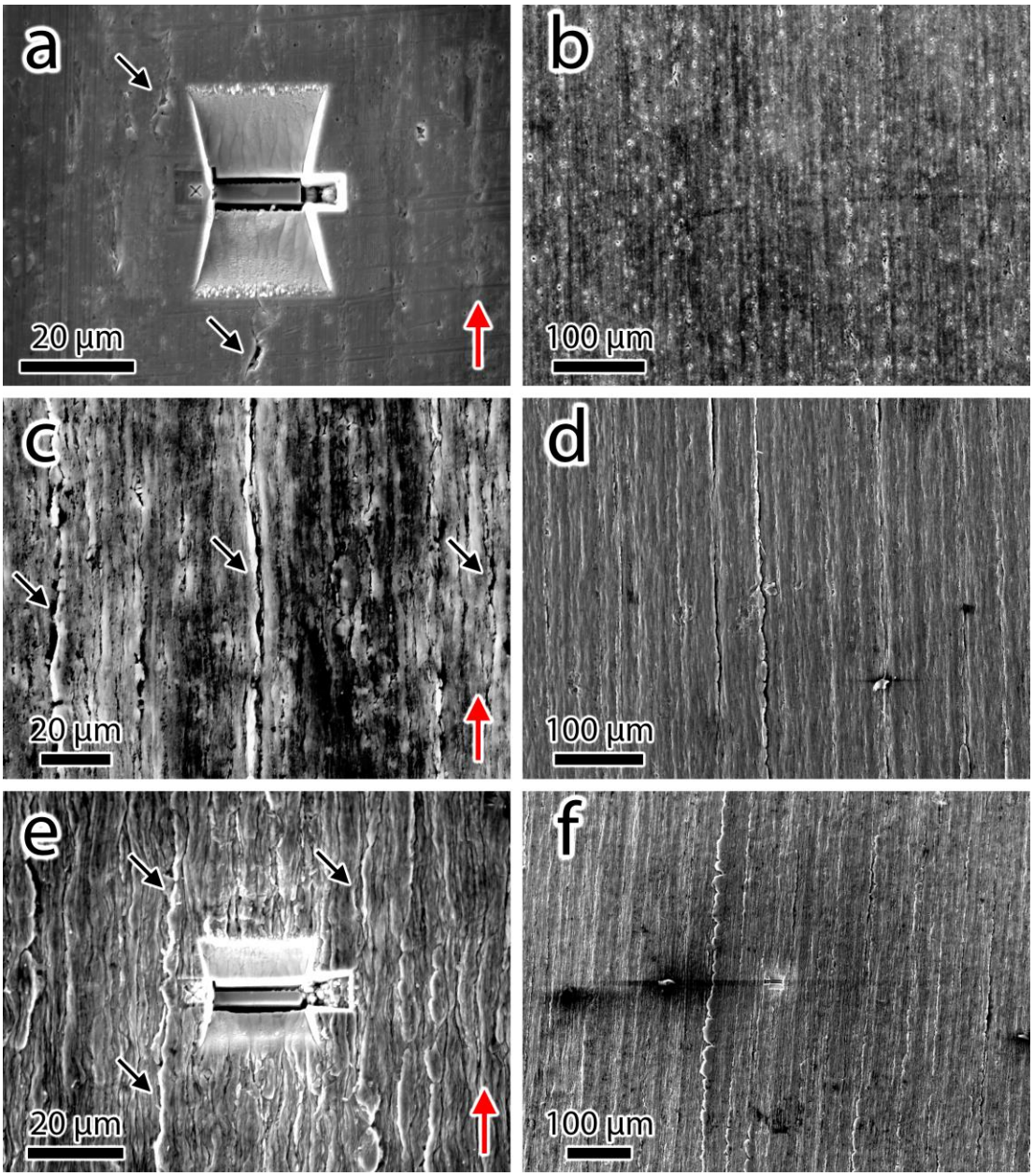

Figure 64. High and low magnification secondary electron images of the surfaces of a-b) ironed, c-d) necked-1, and e-f) necked-2 samples. Red arrows indicate the deep drawing directions. Black arrows indicate examples of surface cracks.

The SEM images of the ironed sample (**Figure 64a-b**) revealed a smooth surface marked by occasional cracks that were several micrometers long, parallel to the drawing direction. The presence of microcracks on the ironed sample indicates that they originate at the earlier stages of the forming sequence.

In contrast, the images of the necked-1 and necked-2 samples (**Figure 64e-f**) exhibited wrinkles, parallel to the drawing direction, expected of samples that have undergone significant drawing processes. Comparisons among the low magnification images (**Figure 64b**, **d**, and **f**) clearly showed more wrinkling as the drawing process progressed. The wrinkles on **Figure 64e** are artifacts of these processes and contain microcracks underneath. The reduced sample diameter during the necking process presumably closed most of the microcracks and the compression resulted in formation of the wrinkles parallel to the drawing direction. FIB lift-out specimens were extracted from arbitrarily chosen microcracks in both ironed and necked-2 samples, whose lift-out sites are shown in **Figure 64**. The plane normal of the lift-out specimen is parallel to the drawing direction, highlighted by red arrows in **Figure 64**.

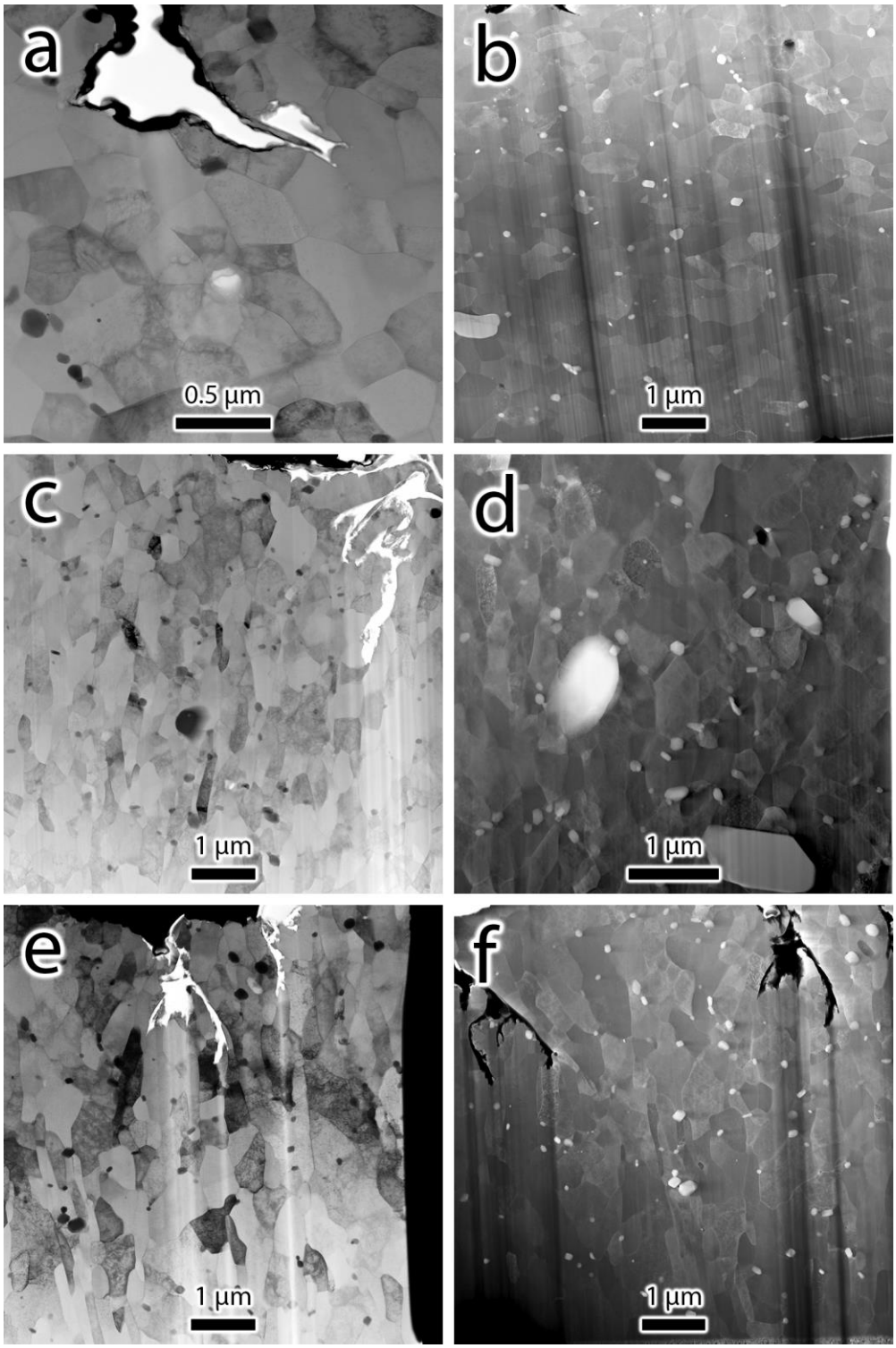

Figure 65. BF (left) and ADF (right) STEM images of ironed (a, b), necked-1 (c, d), and necked-2 (e, f) samples. The bulk sample surfaces are near the top of the images.

Figure 65 shows BF and ADF STEM images of the subsurface microstructure of the ironed, necked-1, and necked-2 samples. Comparisons among different samples reveal the changes in grains as it undergoes more high strain rate drawing processes. The ironed sample (**Figure 65a-b**) exhibited equiaxed grains at all depths of the sample. The matrix contained significant dislocation content, suggesting that the sample had already experienced work hardening. Hardening precipitates were not observed, as expected of a non-heat treatable alloy. The necked-1 sample (**Figure 65c-d**) retained equiaxed grains near the surface of the sample while the grains deeper into the sample were elongated in the radial direction from the center of the bulk sample. This is caused by the reduction in sample diameter during the deep drawing process: the grains near the center experience more compression in the hoop direction than the ones far away (near the sample surface). Nearly every grain was elongated in the necked-2 sample (**Figure 65e-f**), indicating the extent to which the reduction in sample diameter during necking compressed the material.

Dispersoids are shown as black and white particles in the BF and ADF images, respectively. Dispersoids are observed to be distributed evenly throughout the FIB specimens. The images did not reveal any sheared or broken secondary phase particles. Furthermore, most of the dispersoids are located on grain boundaries, possibly because they serve as grain nucleation sites and pin grain boundaries during recrystallization, limiting grain growth [60, 70]. The constituent particles may have stayed intact due to the lack of large grains, those that are microns in diameter. The small grains make dislocation accumulation in the matrix difficult while work hardening via dislocation entanglement easier [155].

5.3.2 TKD Analysis

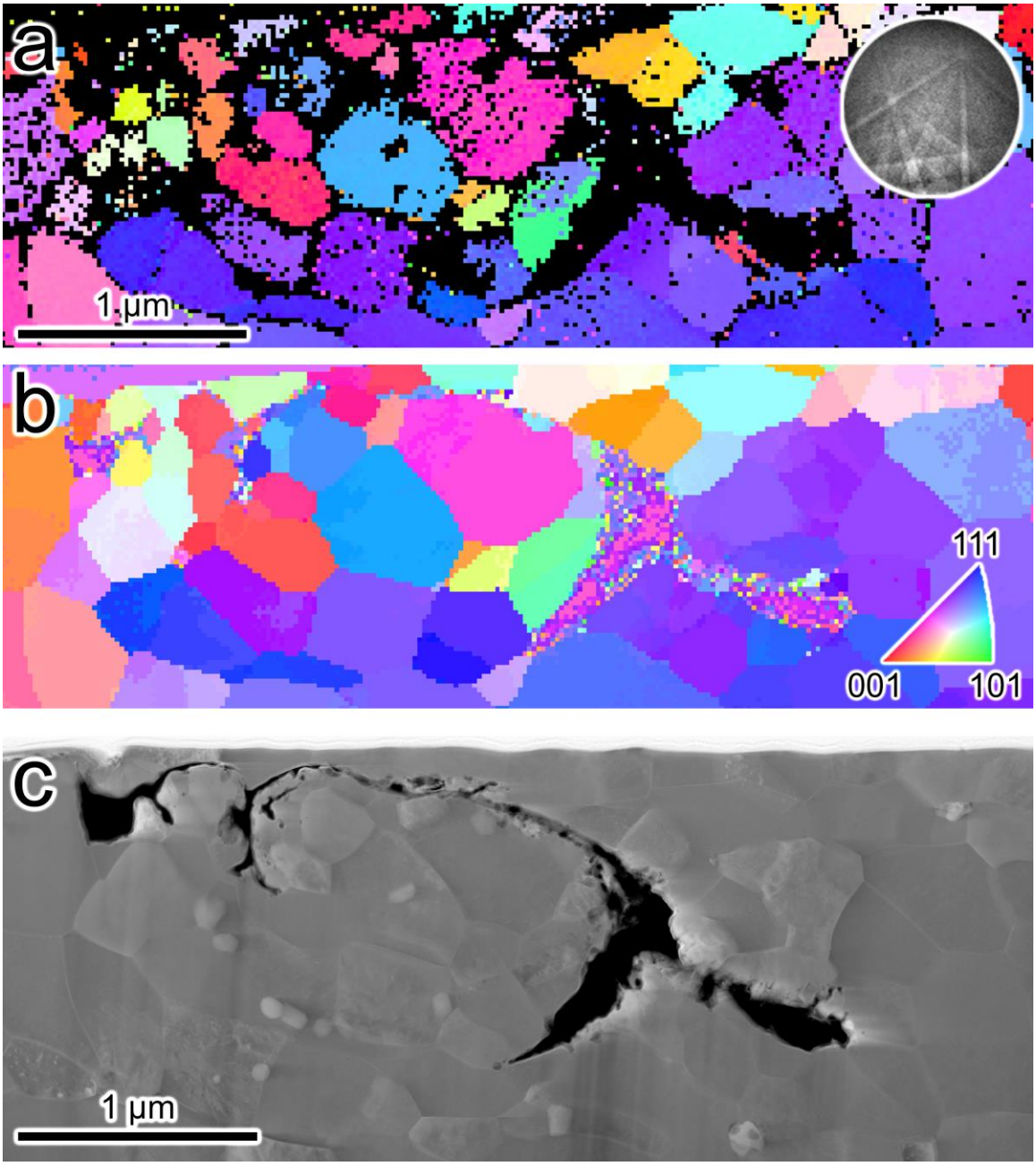

Figure 66. Comparison between inverse pole figure maps generated from TKD patterns a) using the Hough-based (points with confidence index below 0.1, as defined by EDAX/TSL colored black) and b) the dictionary approach. For reference, c) an ADF STEM image is shown at the bottom. The circular inset shows an example of a TKD pattern.

Figure 66a shows the indexing result using the conventional Hough-based indexing method. Because low-quality TKD patterns cannot be accurately indexed, the datapoints whose patterns yielded confidence index of less than 0.1 were filtered out of the inverse pole figure (IPF) map and colored black. The abundance of black pixels illustrates the limitation of Hough-based indexing on severely deformed alloys and the degree to which the sample has been strained. Furthermore, it is unknown if the areas with large clusters of black pixels contain small grains. The fact that many of the black pixels are near the grain boundaries suggests that the latter is more susceptible to localized deformation. Consequently, it is difficult to determine whether the crack path is intergranular or transgranular, restricting the information that can be gathered from the data.

Figure 66b shows an IPF map generated from the dictionary approach. The dictionary approach resolved many ambiguities near grain boundaries and revealed small grains that were not observable in **Figure 66a**. Therefore, the dictionary approach is robust against noise, including those caused by deformed lattices, and can handle overlapping diffraction patterns that occur near grain boundaries.

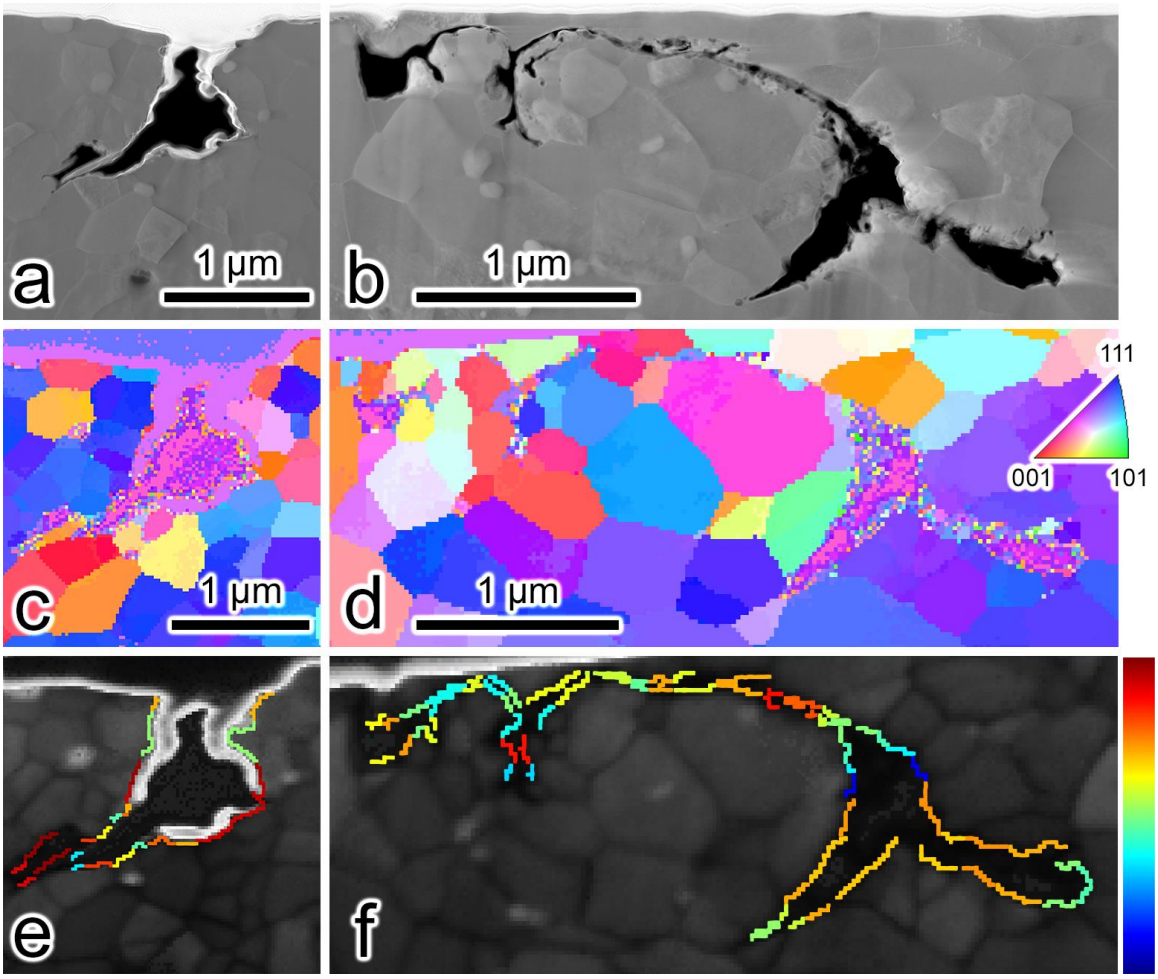

Figure 67. ADF STEM images (a-b), IPF maps (c-d), and EBSD image quality (IQ) maps (e-h) of two different cracks in a FIB lift-out specimen machined from region shown in **Figure 64a**. The dictionary approach was used to index the patterns from the TKD-EBSD data to generate the IPF and IQ maps. The colored pixels in (e-f) represent the misorientation angles between grains on either side of the cracks. The color bar on the right, ranging from 0° to 60°, represents the legend for the colored pixels.

Figure 67 shows ADF STEM images and TKD analysis of two cracks in a FIB lift-out specimen extracted from the ironed sample. As the ADF STEM image (**Figure 67b**) shows, the cracks extend much further below the surface, making microcrack detection with surface characterization alone inadequate, making FIB lift-out a necessity. The STEM

images also show that the FIB milling process resulted in some widening of the cracks and blunting of the crack tips.

Multiple crack bifurcation events are also evident as the crack extends further into the sample and occur at certain triple junctions. This selective behavior suggests that the cracks branch when the local strain—possibly in combination with the strain rate—at the crack tips reach a critical level.

Figure 67c-f shows the combined TKD/dictionary approach analysis of the crack propagation pathway through the microstructure. The IPF maps (**Figure 67c-d**) show that the cracks follow an intergranular pathway, with crack bifurcations correlating with triple junctions in the material. The intergranular fracture is likely due to matrix hardening during the deep drawing process leading to strain localization at the grain boundaries. The IPF maps generated from the TKD data provide insight into possible grain boundary orientation effects on crack propagation pathways.

Figure 67e-f shows the misorientation angle data of the fractured boundaries overlaid on an image quality (IQ) map generated from the TKD patterns. From the analysis, it is evident that the cracks propagate through both high and low angle grain boundaries, suggesting that the boundary character does not play a dominant role in dictating the crack propagation pathway, though more samples would need to be analyzed to establish this with statistical certainty.

5.3.3 STEM Characterization

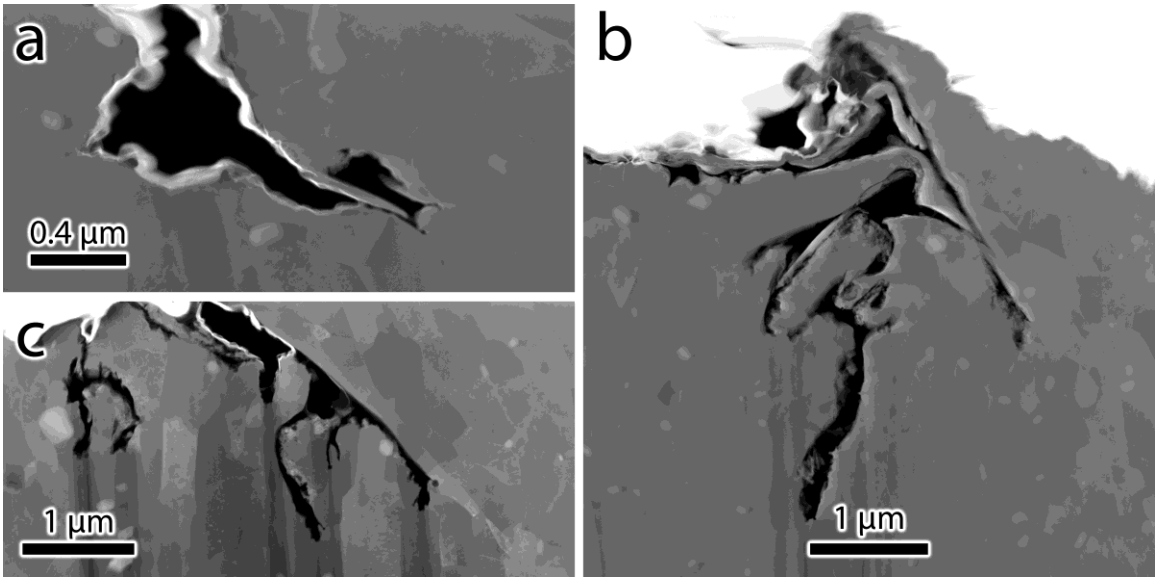

Figure 68. ADF STEM images showing branched microcracks in a) ironed, b) necked-1, and c) necked-2 samples.

Figure 68 shows microcracks in FIB lift-out specimens extracted from the three bulk samples. Consistent with the TKD results in *Section 5.3.2*, the microcracks in the lift-out specimens were intergranular and bifurcated at various triple junctions. If cracks bifurcate when the crack tip meets a triple junction above the critical strain rate, then the number of bifurcation points and the crack length from the surface should correlate with the number of deep drawing dies the samples have passed. As expected, the microcrack shown in **Figure 68a** is the shortest with the fewest bifurcation points. The comparison between the necked-1 sample (**Figure 68b**) and the necked-2 sample (**Figure 68c**) shows the former containing a longer microcrack with possibly more bifurcation points. This is due to the strong sample variance of the site-specific nature of the FIB lift-out specimens.

It is possible that the specimens prepared for this study deviated from the statistical average. A study with larger sample size is required to draw statistically robust conclusions.

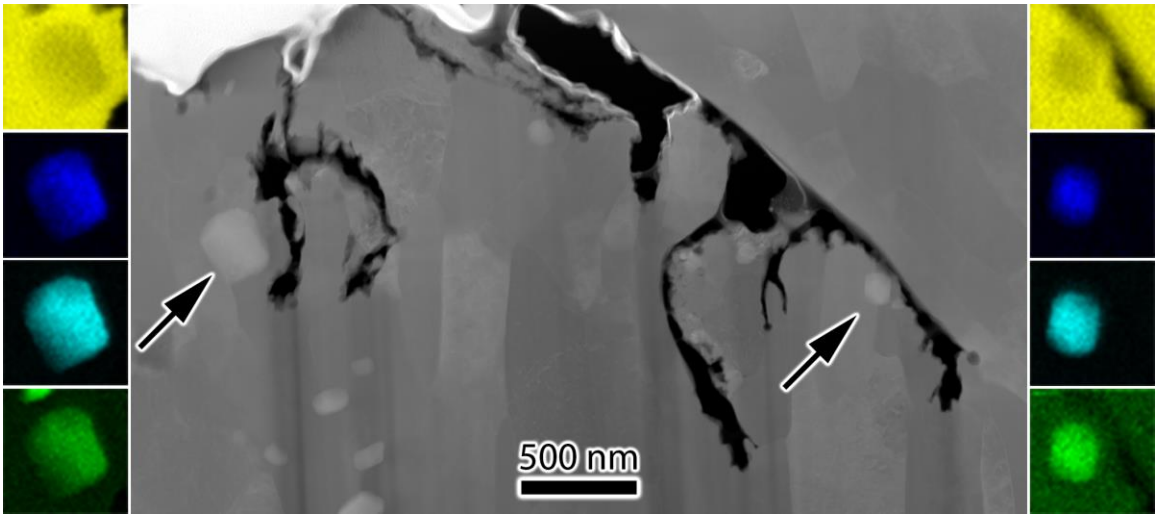

Figure 69. STEM images of FIB lift-out machined from region shown in **Figure 64c**. a) ADF STEM image of branched cracks with EDX chemical maps of Al (yellow), Fe (blue), Mn (cyan), and Si (green) from the dispersoid in the white square. Arrows highlight regions where the EDX analysis was performed.

Figure 69 shows STEM images of the FIB lift-out taken from the necked-2 sample. Compared to **Figure 67a-b**, the cracks in **Figure 69** are extended much longer with multiple bifurcation points, as expected of a more heavily deformed sample. In agreement with the TKD results shown in **Figure 67**, the cracks present in the material later in the forming sequence were still found to be intergranular. Furthermore, the crack tips that are facing down appear blunted, but the curtaining below them indicate that the blunting is most likely an artifact of the FIB milling process [156-158]. However, as will be shown in **Figure 70a-b**, close inspection of the crack tips arrested by the dispersoid shows that, when not blunted by the FIB milling process, they are very sharp and intergranular. These features are likely reflective of the hardened matrix, which is expected to have a high

dislocation content from the forming processes and does not accommodate the plasticity needed to blunt the cracks.

The insets in **Figure 69** are chemical maps generated from EDX data from the two areas highlighted by black arrows. The Z-contrast in the ADF STEM image highlights the dispersoids bright objects throughout a dark matrix. This is most likely caused by elements with higher atomic numbers than Al present in the particles. As shown in the EDX chemical maps, the dispersoids are Al(Fe, Mn)Si, which is consistent with previous studies [3, 4, 8, 61]. The crystal structure of dispersoids can be deduced from the chemical composition. It has been noted that the addition of Si favors the formation of simple cubic α-Al(Mn)Si [33] while Fe can substitute Mn in the α-Al(Mn)Si phase and increase the likelihood that a body centered cubic structure forms [3, 4, 61]. When the Mn:Fe ratio is high, the dispersoids are likely to be simple cubic, while a low Mn:Fe ratio may result in a body centered cubic structure. Due to the presence of Fe, the dispersoids in the samples are presumed to be body centered cubic.

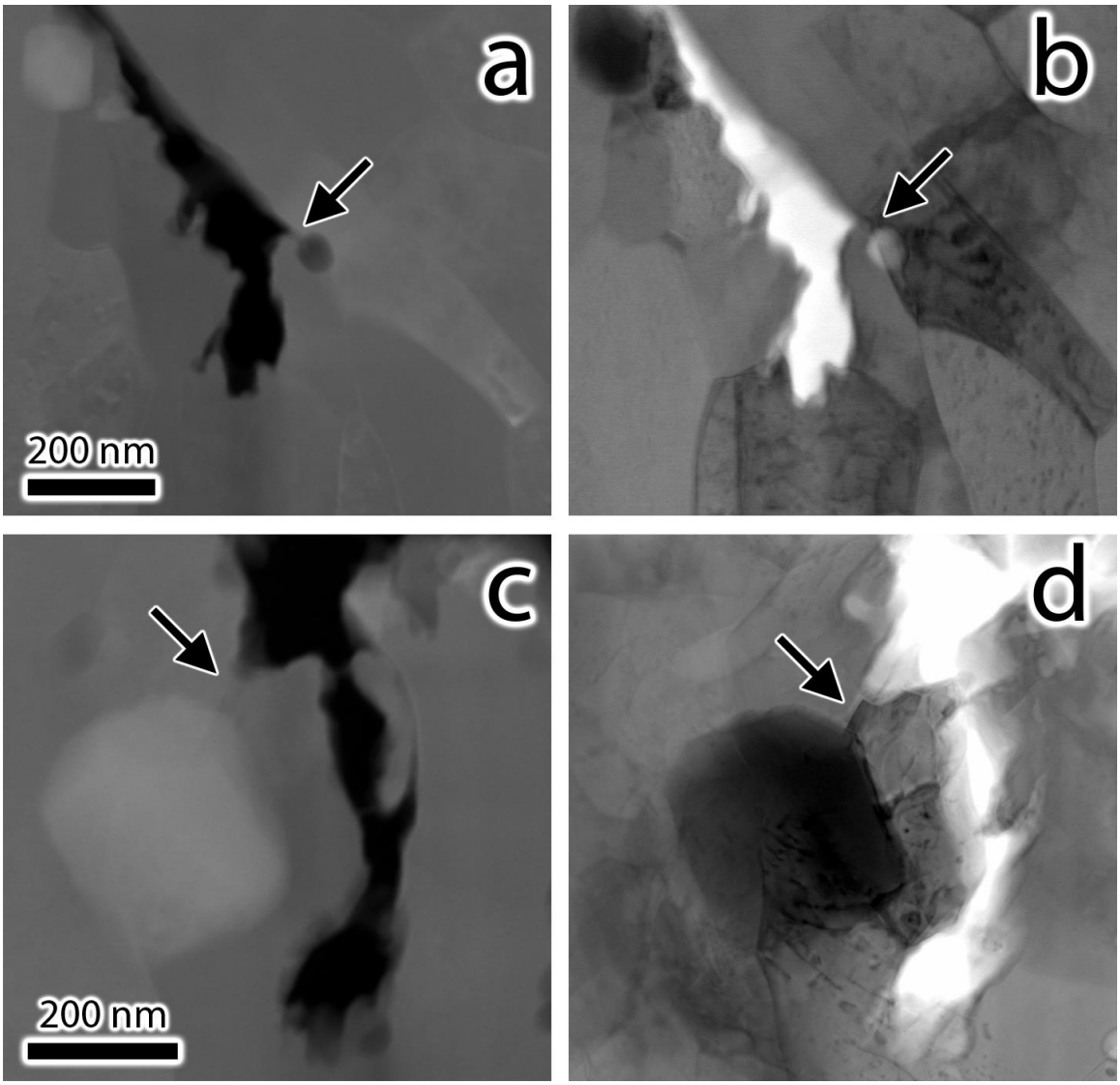

Figure 70. ADF (a, c) and BF (b, d) STEM images of dispersoids highlighted by black arrows in **Figure 69**. The black arrows in this figure indicate grain boundaries ahead of crack tips that were arrested and changed the propagation direction to grow away from the dispersoids.

The regions pointed out by black arrows in **Figure 69** exhibited evidence of cracks whose pathways deviated from a direct path. Enlarged views of these regions, shown in **Figure 70**, show that these deviation points correlate with dispersoids being present in the grain boundary, presumably blocking the crack propagation and diverting further crack

propagation into a different grain boundary. In **Figure 70a-b**, the dispersoid, which normally appears brighter in ADF and darker in BF images, has fallen out during the sample preparation process, leaving a hollow spherical region, making it appear darker in the ADF image and brighter in the BF image. **Figure 70d-e** show another example of a dispersoid causing a deviation in the most direct crack growth direction. The two highlighted dispersoids differ in size by approximately one order of magnitude, suggesting that there is a wide range in dispersoid sizes that can cause the observed effect.

5.4 Discussion

5.4.1 Intergranular Crack Propagation

In general, ductile alloys such as AA3xxx fail via void nucleation-growth-coalescence mechanism when subjected to extreme tensile loads, and the abundance of dimples on fracture surfaces (**Figure 11**) is evidence of this phenomenon [47, 48]. In addition, at the centers of large dimples are constituent particles, indicating that they can act as void nucleation sites, whether by decohesion at the particle-matrix interface or by particle cracking (**Figure 11a-b**). The hardening precipitates in AA6061 have also been shown to be conducive to void nucleation (**Figure 11c-d**) [59], although whether a crack is intergranular or transgranular depends on various factors such as aging condition [151]. Furthermore, increasing the concentration of dispersoids in aluminum alloys has commonly been shown to promote transgranular fracture over intergranular fracture and increase the ductility in a range of loading conditions [9, 11]. This effect is commonly

attributed to the dispersoids homogenizing the plasticity in the matrix and decreasing the magnitude of strain concentrations at grain boundaries.

Despite the presence of microstructural features that are conducive to transgranular fracture, however, all the observed microcracks were intergranular. This phenomenon can be explained with microstructural and external factors. The grains in this study were found to be mostly less than 1 μm in diameter. The small grains provide limited volume where dislocations can form and accommodate plastic strain, resulting in a Hall-Petch type strengthened microstructure [155, 159]. In addition, smaller grains can be saturated of dislocation content at lower plastic strain levels, increasing the work hardening exponent. The grains in ironed AA3xxx were observed to have high dislocation content even at early stages of the deep drawing process, resulting in a work hardened matrix that gave limited space for dislocation pileups that can nucleate voids in the matrix or at the particle-matrix interface, which also explains the lack of cracked secondary particles. Therefore, the grain size made intergranular crack propagation more energetically favorable than transgranular crack path.

The external reason for intergranular crack can be attributed to high strain rate. The strain rates for the studies mentioned above are lower than that used for the deep drawing process. The effects of high strain can vary depending on the material and the stress state of the crack tip in consideration. However, applying high strain rate to a work-hardened grain would be difficult to introduce or move dislocations, consequently moving the burden of plastic deformation to the grain boundaries. Therefore, the intergranular crack paths are

consequences of the microstructural state and the high strain rate, despite the presence of constituent particles and aluminum matrix that suggest transgranular failure.

5.4.2 Crack Branching

Cracks branches have also been observed in all samples with bifurcation points at certain triple junctions. This is presumed to be caused when the local strain, possibly along with local strain rate, at the crack tip reaches a critical threshold. Several other microstructural factors may also decide which triple junctions can become bifurcation points: orientation and length of grain boundaries. The angle at which the grain boundary meets the crack tip is an important factor to consider. The complexity of the stress state around an out-of-plane crack tip requires theoretical calculations to measure the shear stress at a given grain boundary orientation. The grain boundaries lie within the range of angles where the critical shear strain is achieved around crack tip are potential crack propagation paths.

When energy is taken into consideration, the length of grain boundaries dictates the amount of energy that can be released by separating two grains. In **Figure 68b-c**, it is noteworthy that cracks bifurcate primarily close to the surface, and there are longer cracks deeper into the sample that exhibit little to no crack branching behavior. This behavior can be attributed to the elongated grain deep within the sample. From **Figure 65**, it can be observed that elongated grains are only present deep in the sample at early stages of the drawing process. At later stages of the process, elongated grains are observed near the surface as well. With longer grain boundaries, not only are triple junctions rarer, energy

can be released easier by growing a crack along the same grain boundary rather than by changing directions and splitting the crack into paths that deviate from the original grain boundary. Therefore, longer grain boundaries not only decrease the number of potential bifurcation points, but also decrease the likelihood of bifurcation events by providing crack paths that does not require change in crack propagation direction.

5.4.3 Dispersoid Effects on Crack Propagation

In **Figure 70**, dispersoids showed evidence of arresting cracks and diverting cracks away from them. Assuming dispersoids play no role in crack propagation behavior, both of the intergranular microcracks should have continued growing in the same direction and propagated into the grain boundaries that housed the dispersoids. Thermodynamically speaking, the cracks should continue growing in the same direction unless a less resistant and more energetically favorable path becomes available at the crack tip. Instead, the cracks either stop at the dispersoid interface (black arrow, **Figure 70a-b**) or at the triple junction near it (black arrow, **Figure 70c-d**). The cracks change their directions to propagate to an adjacent grain boundary, a more energetically favorable path due to the presence of dispersoids.

Dispersoids have been shown to influence local deformation behavior by homogenizing slip distribution [11]. The dislocations cannot transmit though the incoherent dispersoid-matrix interface, making the dispersoids unshearable. Dowling and Martin observed that dispersoids reduce the strain concentrations caused by slip bands by work hardening the active slip planes around them, promoting the formation of slip at a

different plane [11]. Consequently, dislocations accumulate at the interface when the alloy deforms plastically and work hardens the active slip plane. This causes the transfer of slip to a different slip plane, thereby eventually homogenizing the distribution of dislocations and slip, leading to increased toughness. In fracture mechanics terms, dispersoids increase the work hardening exponent (*n*), which is generally beneficial for mitigating wall cracking, as discussed in the introduction section of this chapter (see **5.1 Introduction**).

This dispersoid effect has a direct influence on the crack tip behavior, which translates to increased ductility and toughness. Prince and Martin observed that the size of the plastic zone ahead of crack tips increases with increases in dispersoid density, though intergranular fracture still occurred where slip bands impinged on grain boundaries [9]. Edwards and Martin observed that increasing the dispersoid volume fraction from 0 to 0.78 vol% significantly delayed fatigue crack nucleation and increased the number of cycles to failure from 160 to 2500 during low cycle fatigue tests [74]. Davidson and Lankford also reported that dispersoid mean free path affected the growth rate of fatigue cracks more than grain size and strengthening precipitates [75]. As previous studies have demonstrated, dispersoid content is an influential factor for determining various loading conditions.

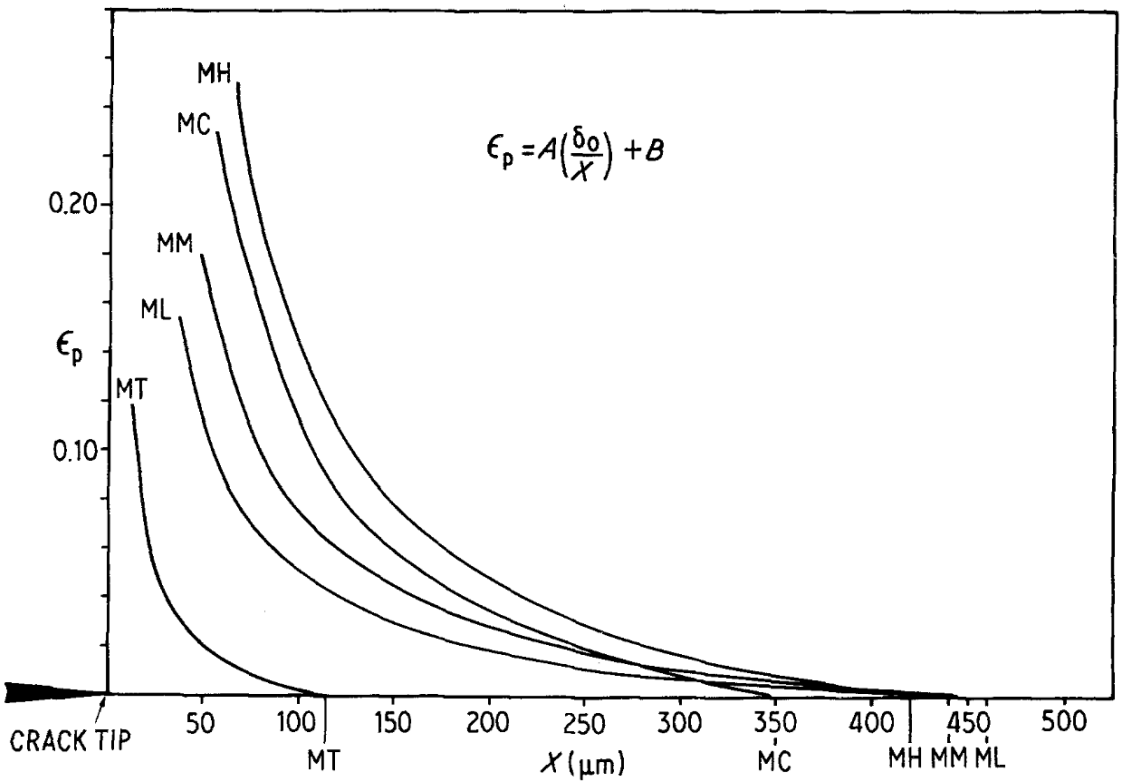

Figure 71. a) Plastic strain profile ahead of a crack tip in an Al-Mg-Si system with (ML, MM, MH, and MC, ordered in increasing dispersoid volume fraction) and without dispersoids (MT) [10]. Sample "MC" had a lower strain profile than sample "MH" despite having higher dispersoid volume fraction, possibly because it contains coarse particles that serve as void nucleation sites. Reprinted with permission from Springer Nature.

In the case of deep drawn AA3xxx, the crack arrest may be a manifestation of two different characteristics of dispersoids: strain homogenization and high hardness. Blind and Martin also noted that the plastic zone ahead of crack tips (**Figure 71**) are considerably larger for dispersoid-containing alloys than those without [10], consistent with results by Prince and Martin [9]. They observed that the strain profile ahead of the crack tip was generally increased as a function of dispersoid volume fraction, meaning samples with higher dispersoid content were able to accommodate more plastic energy and critical strain must be achieved over larger critical distances for crack growth. The crack arrest observed

in this study (**Figure 70**) is a related phenomenon, where the strain field around dispersoids required addition of more energy to propagate to a grain boundary containing it than an adjacent boundary without. Consequently, the microcrack propagated to the adjacent boundary, which provided a lower-energy path for crack growth.

Dispersoid-induced crack arrest may also be a result of the difference in hardness of the dispersoids compared to the soft Al matrix. Studies with ceramics embedded with harder and stiffer particles exhibited higher tensile strength [160]. When a crack meets hard particles, more energy must be consumed to break the particles before the crack can further propagate. Similarly, dispersoids may be playing a role as a hard particle that resists crack extension, making the grain boundaries that contain them pose as a significant energy barrier for crack propagation, causing cracks to change their paths.

In all the samples, dispersoids were found to be fairly evenly distributed throughout the microstructure (**Figure 65**), many of which lie on grain boundaries. Although its effects are difficult to quantify with limited number of samples, the ubiquity of dispersoids suggest that they play a significant role in the drawability of AA3xxx. This does not imply that higher dispersoid content are always better: as Blind and Martin showed in **Figure 71**, excessive addition of alloying elements to boost dispersoid volume leads to decreased toughness [10]. Even if the dispersoid density increased while the size remained optimal, microcracks will always find a grain boundary to propagate, and if the dispersoid density is too high, cracking may occur at the few boundaries left without dispersoids, leading to catastrophic failure before the part is finished.

5.4.4 Gnomonic Projection in TKD Patterns

TKD patterns and EBSP are generated as gnomonic projections of angular diffraction data that are collected on a flat phosphor screen on EBSD detectors [161]. The TKD configuration used in this study (**Figure 30b**) and many others [90, 93, 97, 100, 101] is set up so that the phosphor screen of the EBSD detector is oriented vertically, almost perpendicular to the specimen. Consequently, this configuration only allows for detection of electron scattered at high angles, which leads to several problems such as low intensity electron signal and geometric pattern distortion [94, 162]. Although the former may be resolved relatively easily by changing the electron beam settings or thinner specimens [163, 164], the latter poses a greater challenge for indexing the TKD patterns.

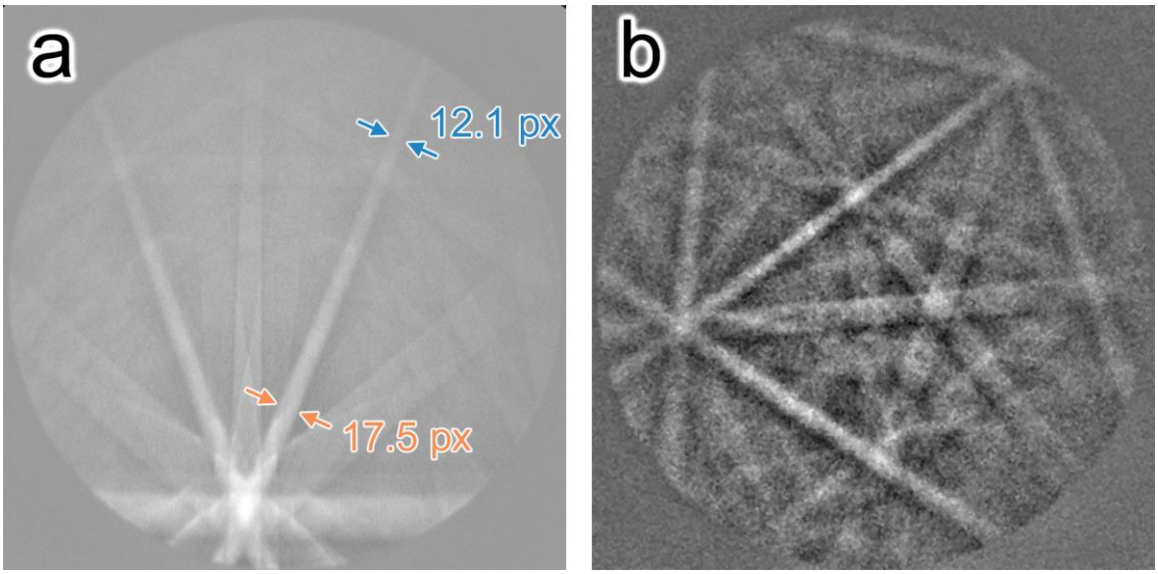

Figure 72. a) TKD pattern and b) EBSP collected at 25 kV and 20 kV electron acceleration voltage, respectively. The arrows indicate different widths of the same Kikuchi band caused by gnomonic distortion.

The gnomonic distortion is caused by the distance between the center of the detector and the pattern center (PC) [94], where the central z-axis of the gnomonic projection meets the detector plane [161]. Because of the limited size of the phosphor screens, EBSD detectors can only capture a small portion of the diffraction data, and the further its center is from the PC, greater the distortion due to the nature of gnomonic projection. This induces strong gnomonic projection-induced distortion in TKD patterns (**Figure 72a)** that are not often observed in conventional EBSD patterns (**Figure 72b**). The distance between the PC and the center of the phosphor screen can be changed by adjusting the sample tilt. As a result, the TKD patterns are generated from low intensity signals that yield broader, fainter, and warped Kikuchi bands. More specifically, the distortion causes Kikuchi bands to widen with increasing distance from the PC, making it difficult to index using the conventional Hough-based method, which relies on detection of straight lines. More FIB lift-out specimens with minimal ion damage may be required to study which of the two explanations are responsible for the dispersoid-induced crack arrest.

One way to reduce the gnomonic distortions is by aligning the center of the EBSD detector to the optical axis of the SEM [94, 162, 165]. The new sample-detector geometry solves the low intensity and strong distortion issues by placing the sample close to the phosphor screen whose center is aligned with the SEM optical axis, minimizing the PC deviation from the detector center.

5.5 Conclusion

The effects of dispersoids and grain boundary characteristics on the crack propagation behavior in AA3xxx during deep drawing have been studied using STEM and TKD combined with dictionary approach. Despite the ductile nature of AA3xxx containing dispersoids, the microcracks did not follow the void nucleation-growth-coalescence mechanism.

The results showed that the matrix was significantly strain hardened even at an early stage of the drawing process, facilitating intergranular crack propagation. In addition, crack branching was observed where cracks bifurcated at certain triple junctions, possibly where the local strain and the strain rate reached a critical threshold. Grain elongation as a function of depth and level of deformation was also explored: revealing that grains were originally equiaxed but were eventually elongated from deep within the sample to the surface. This, along with grain boundary orientation relative to the microcrack, can influence the frequency and probability of crack bifurcation. The present work also revealed that the misorientation angle between grain boundaries has little influence on the crack propagation behavior of AA3xxx during deep drawing.

Furthermore, the cracks avoided propagating to grain boundaries with dispersoids, showing that dispersoids can arrest cracks and divert crack growth pathways. The strain homogenizing effect of dispersoids and their higher hardness are likely causing the crack to propagate to a lower-energy pathway. Although the strain homogenizing effects of dispersoids have been studied for decades, their interaction with different loading

conditions and strain rates requires further research to fully comprehend how dispersoids can be utilized to engineer tougher aluminum alloys.

The present work is one of the first practical application of TKD combined with the dictionary approach. The enhanced spatial resolution of TKD compared with the traditional EBSD technique allowed for probing of small grains with greater clarity of the matrix. The dictionary approach made characterization of severely deformed polycrystalline alloys possible. The dictionary approach had an additional serendipitous benefit of overcoming challenges of indexing TKD patterns with gnomonic distortion in the TKD patterns by simulating patterns using a physics-based model.

CHAPTER 6. CONCLUSIONS AND FUTURE WORK

6.1 Overarching Conclusions

The aim of this dissertation was to investigate the influence of dispersoids on the crack initiation mechanism of AA6451 during three-point bending tests and crack propagation behavior in AA3xxx during deep drawing.

During three-point bending of AA6451, cracks nucleated at grain boundaries preceded by formations of ledges. Microscale characterization revealed that the ledges were manifestations of localized plastic deformation at grain boundaries. The locations of ledges were chiefly determined by the orientation of the grain boundary with respect to the tensile load axis on the front plane, while misorientation angle had no noticeable effect. The formation of ledges was accompanied by grain refinement around the grain boundaries as a result of dislocation accumulation and assimilation into low-angle boundaries followed by heterogeneous crystal rotation. It was found that dispersoids delayed the formation of dislocation structures that precedes grain refinement at low levels of applied strain. At high strain, however, the dislocation structures evolved into distinct crystal rotation boundaries preferentially around the unshearable dispersoids, which may serve as crack nucleation sites or potential crack propagation paths.

The variation in dispersoid density, grain size, and precipitate free zone width were not clearly detectable from microscopy analyses. EBSD scans, however, revealed that higher Mn and Cr content produced stronger cube texture in AA6451-T6 and -T4.

Deep drawn and necked AA3xxx exhibited intergranular surface cracks that bifurcated at certain triple junctions. It is thought that the high dislocation content in the matrix strain hardened the grains and facilitated intergranular cracking. The branching behavior is seen as a result of localized strain and strain rate at the crack tips overcoming critical thresholds during the deformation process. Dispersoids were observed to arrest and divert crack propagation directions away from them. This is achieved by reducing localized plastic deformation around the grain boundary, thereby making it more energetically favorable for cracks to grow through other grain boundaries without dispersoids.

Overall, dispersoids were observed to have a significant impact on the crack initiation and propagation behaviors in aluminum. Generally, dispersoids were observed to be beneficial by delaying crack nucleation and arresting intergranular cracks via strain homogenization, but the accumulation of dislocations around dispersoids may facilitate localized formation of defect structures that precede crack initiation and propagation.

6.2 Future Research Directions

6.2.1 AA6451 Project

Much of the conclusions about dispersoid effects on the bending behavior of AA6451 were deduced from post-mortem SEM, TEM, and STEM images. Although they provided a wealth of information about how dispersoids influenced slip band and grain refinement, there remain aspects of the particles that have yet to be explored.

For one, implementing 4D-STEM analysis around dispersoids at various stages of the grain refinement and slip band formation will paint a more comprehensive picture of the details of the processes. The diffraction-based techniques may provide insight into the strain build up around the dispersoids. This can also be used to quantitatively measure the strain homogenization that occurs around dispersoids. 4D-STEM can also be used to generate strain maps of grain refinement process. These will be useful data for keeping track of cell boundary generation and movement leading up to the formation of refined grain boundary. Another interesting study will be to use strain maps around cracked constituent particles to investigate why cracks nucleated from cracked constituent particles did not propagate into the matrix, unlike those during the tensile tests.

In this study, only grain boundary orientation with respect to the tensile load axis was identified as the driving factor for GBL formation. A more in-depth correlation study must be conducted on the large-scale EBSD scans after mechanical testing. Due to the complexity of the microstructure from the variety of microstructural defects, identifying more microstructural factors will require more sophisticated and rigorous statistical analyses that looks into synergistic effects of combinations of defects (*e.g.* correlating GBL formation around small grains that has dispersoid volume fraction above 0.05).

In-situ SEM three-point bend test would be a great way to observe the development of dislocation structures. The bend test rig used for this project orients the sample in a way that the narrow top plane of the sample is visible. Taking SEM images and EBSD scans from the top surface during bending at interrupted stages of the tests will show how dispersoids and grain boundaries affect formations of microshear bands. Another idea

would be to use a rig that allows for EBSD characterization of the front plane *in-situ*. This will involve a stationary rigid sheet with a rectangular hole where the rig tries to push the sample through the hole. SEM image and EBSD scans of the front planes will provide more data for identifying the microstructural features conducive to GBL formation. It may also shed light onto the dislocation structures that develop near grain boundaries that produce ledges, which can be used as data for studying the plastic strain in the matrix.

6.2.2 AA3xxx Project

Although FIB lift-out is an excellent technique for probing the local interactions of cracks with its surrounding microstructure, its biggest drawback is the difficulty of verifying the interactions with statistics. Each lift-out specimen takes at least 4 hours to prepare, and significant increase in speed runs the risk of damaging the specimen with ion beam that can hinder careful microscopy. Therefore, making a large number of lift-out specimen for statistical studies comes at a great financial and labor cost.

A potential method of investigating large number of microcracks is to mount the bulk samples into a conductive epoxy or Bakelite for polishing. SEM and EBSD analyses will allow for microscale surveys to confirm the presence of intergranular crack branches. This may also allow for correlating the grain boundary misorientation angle to crack propagation paths. Although the results shown in **Figure 67e-f** showed no correlation, the microscale approach will provide the necessary sample size to draw a more statistically-robust conclusion. With large enough samples, it may also be possible to study the origin of the microcracks and the microstructural features that are conducive to their formation.

If the SEM resolution allows for detection of dispersoids, it will also be possible to statistically correlate microcrack paths with dispersoid number density.

It will also be interesting to perform FIB-SEM tomography in a coupled with EDX and EBSD analyses. Some microcracks may be small enough to be contained within a tomography sample, while the EDX detector can confirm the presence of dispersoids in their surroundings. The goal of EBSD analysis will be to confirm if the crack propagation is a slip-driven process or a consequence of brittle intergranular fracture of a work-hardened alloy. The 3-dimensional analysis of microcracks may also assist with the theoretical models for crack propagation behavior. The results can also provide insights into modeling strain fields around dispersoids and how they affect the mechanical behavior of AA3xxx.

REFERENCES

1. H. Klocker and C. Yukna, *Aluminum Sheet Metal Damage Mechanisms Application to Trimming and Hemming*. 2017.

2. F.N. Afshar, J.H.W. de Wit, H. Terryn, and J.M.C. Mol, *Scanning Kelvin probe force microscopy as a means of predicting the electrochemical characteristics of the surface of a modified AA4xxx/AA3xxx (Al alloys) brazing sheet.* Electrochimica Acta, 2013. **88**: p. 330-339.

3. A.M.F. Muggerud, E.A. Mørtsell, Y. Li, and R. Holmestad, *Dispersoid strengthening in AA3xxx alloys with varying Mn and Si content during annealing at low temperatures.* Materials Science and Engineering: A, 2013. **567**: p. 21-28.

4. Y.J. Li and L. Arnberg, *Quantitative study on the precipitation behavior of dispersoids in DC-cast AA3003 alloy during heating and homogenization.* Acta Materialia, 2003. **51**(12): p. 3415-3428.

5. J. Courbon. *Mechanical metallurgy of aluminium alloys for the beverage can*. in *Materials science forum*. 2000. Trans Tech Publ.

6. Q. Zhao, B. Holmedal, and Y. Li, *Influence of dispersoids on microstructure evolution and work hardening of aluminium alloys during tension and cold rolling.* Philosophical Magazine, 2013. **93**(22): p. 2995-3011.

7. D.H. Lee and S.W. Nam, *Role of Mn-dispersoid in the fracture toughness enhancement of Al-Zn-Mg-(Mn) alloys.* Metals and Materials, 1995. **1**(1): p. 71-76.

8. Y.J. Li, A.M.F. Muggerud, A. Olsen, and T. Furu, *Precipitation of partially coherent α-Al(Mn,Fe)Si dispersoids and their strengthening effect in AA 3003 alloy.* Acta Materialia, 2012. **60**(3): p. 1004-1014.

9. K.C. Prince and J.W. Martin, *The effects of dispersoids upon the micromechanisms of crack propagation in Al-Mg-Si alloys.* Acta Metallurgica, 1979. **27**(8): p. 1401-1408.

10. J.A. Blind and J.W. Martin, *The effect of dispersoids on the micromechanisms of crack extension in Al-Mg-Si alloys.* Journal of Materials Science, 1983. **18**(4): p. 1224-1234.

11. J.M. Dowling and J.W. Martin, *The influence of MN additions on the deformation behaviour of an Al-Mg-Si alloy.* Acta Metallurgica, 1976. **24**(12): p. 1147-1153.

12. K.C. Prince and J.W. Martin, *The study of local plastic strain distribution in aged Al alloys by selected area channelling patterns in the SEM.* Metallography, 1977. **10**(1): p. 107-113.

13. I. Nikulin, A. Kipelova, S. Malopheyev, and R. Kaibyshev, *Effect of second phase particles on grain refinement during equal-channel angular pressing of an Al–Mg–Mn alloy.* Acta Materialia, 2012. **60**(2): p. 487-497.

14. N. Le Maoût, S. Thuillier, and P.Y. Manach, *Aluminum alloy damage evolution for different strain paths – Application to hemming process.* Engineering Fracture Mechanics, 2009. **76**(9): p. 1202-1214.

15. K.-i. Mori and Y. Abe, *A review on mechanical joining of aluminium and high strength steel sheets by plastic deformation.* International Journal of Lightweight Materials and Manufacture, 2018. **1**(1): p. 1-11.

16. K.K. Sankaran and R.S. Mishra, *Metallurgy and Design of Alloys with Hierarchical Microstructures*. 2017: Elsevier.

17. T.A. Barnes and I.R. Pashby, *Joining techniques for aluminium spaceframes used in automobiles: Part II — adhesive bonding and mechanical fasteners.* Journal of Materials Processing Technology, 2000. **99**(1): p. 72-79.

18. H. Livatyali, A. Müderrisoğlu, M.A. Ahmetoğlu, N. Akgerman, G.L. Kinzel, and T. Altan, *Improvement of hem quality by optimizing flanging and pre-hemming operations using computer aided die design.* Journal of Materials Processing Technology, 2000. **98**(1): p. 41-52.

19. Z. Hamedon, K.-i. Mori, and Y. Abe, *Hemming for Joining High Strength Steel Sheets.* Procedia Engineering, 2014. **81**: p. 2074-2079.

20. S. Gürgen, M.İ. Gökler, H. Darendeliler, Ç.C. Çelikkaya, and K. Erden, *Analysis of roller hemming process for a vehicle tailgate closure.* AIP Conference Proceedings, 2013. **1532**(1): p. 367-374.

21. P. Jimbert, I. Pérez, I. Eguia, and G. Daehn, *Straight Hemming of Aluminum Sheet Panels Using the Electromagnetic Forming Technology: First Approach.* Key Engineering Materials - KEY ENG MAT, 2007. **344**: p. 365-372.

22. H. Livatyali, *Computer aided process design of selected sheet metal bending processes - flanging & hemming.* 1998, The Ohio State University.

23. H. Livatyali and S.J. Larris, *Experimental investigation on forming defects in flat surface–convex edge hemming: roll, recoil and warp.* Journal of Materials Processing Technology, 2004. **153-154**: p. 913-919.

24. H. Livatyali, T. Laxhuber, and T. Altan, *Experimental investigation of forming defects in flat surface–convex edge hemming.* Journal of Materials Processing Technology, 2004. **146**(1): p. 20-27.

25. N. Le Maoût, S. Thuillier, and P.Y. Manach, *Classical and Roll-hemming Processes of Pre-strained Metallic Sheets.* Experimental Mechanics, 2010. **50**(7): p. 1087-1097.

26. S.F. Golovashchenko, *Sharp flanging and flat hemming of aluminum exterior body panels.* Journal of Materials Engineering and Performance, 2005. **14**(4): p. 508-515.

27. W.F. Hosford and J.L. Duncan, *The Aluminum Beverage Can*, in *Scientific American*. 1994, Scientific American, a division of Nature America, Inc. p. 48-53.

28. M. Wallmeier, E. Linvill, M. Hauptmann, J.-P. Majschak, and S. Östlund, *Explicit FEM analysis of the deep drawing of paperboard.* Mechanics of Materials, 2015. **89**: p. 202-215.

29. M. Sodeik, Auml, K. Ffner, and F. Weber, *Fundamentals of Modern Can Making and Materials Development for Two-piece Can Manufacturing.* Transactions of the Iron and Steel Institute of Japan, 1988. **28**(8): p. 672-677.

30. W. Wen, J. Go, and D. Kang, *Aluminum alloys for highly shaped packaging products and methods of making the same*, in *Google Patents*, U.S. Patent, Editor. 2018, Novelis Inc.: United States.

31. J. Go, G.-F. Cheng, J.S. Warner, and S. Jurendic, *Process to manufacture large format aluminum bottles*, in *Google Patents*, U.S. Patent, Editor. 2017, Novelis Inc.: United States.

32. H.H. Diekhoff and A.F. Clarke, *Threaded aluminum cans and methods of manufacture*, in *Google Patents*, U.S. Patent, Editor. 1998, Aluminum Company of America: United States.

33. D.T.L. Alexander and A.L. Greer, *Solid-state intermetallic phase tranformations in 3XXX aluminium alloys.* Acta Materialia, 2002. **50**(10): p. 2571-2583.

34. Y. Qin, W.-N. W.A, and J. Zhao, *Chapter 13 - Forming of Micro-sheet Metal Components*, in *Micromanufacturing Engineering and Technology (Second Edition)*, Y. Qin, Editor. 2015, William Andrew Publishing: Boston. p. 299-322.

35. M. Ramezani and Z.M. Ripin, *6 - Deep drawing of sheet metals using the friction-actuated blank-holding technique*, in *Rubber-Pad Forming Processes*, M. Ramezani and Z.M. Ripin, Editors. 2012, Woodhead Publishing. p. 119-147.

36. A. Bhaduri, *Deep Drawing*, in *Mechanical Properties and Working of Metals and Alloys*. 2018, Springer Singapore: Singapore. p. 693-719.

37. D. Lassance, D. Fabregue, F. Delannay, and T. Pardoen, *Micromechanics of room and high temperature fracture in 6xxx Al alloys.* Progress in Materials Science, 2007. **52**(1): p. 62-129.

38. G.S. Chen, M. Gao, and R.P. Wei, *Microconstituent-Induced Pitting Corrosion in Aluminum Alloy 2024-T3.* CORROSION, 1996. **52**(1): p. 8-15.

39. R.S. Piascik and S.A. Willard, *THE GROWTH OF SMALL CORROSION FATIGUE CRACKS IN ALLOY 2024.* Fatigue & Fracture of Engineering Materials & Structures, 1994. **17**(11): p. 1247-1259.

40. P.S. Pao, S.J. Gill, and C.R. Feng, *On fatigue crack initiation from corrosion pits in 7075-T7351 aluminum alloy.* Scripta Materialia, 2000. **43**(5): p. 391-396.

41. K. Jones and D.W. Hoeppner, *The interaction between pitting corrosion, grain boundaries, and constituent particles during corrosion fatigue of 7075-T6 aluminum alloy.* International Journal of Fatigue, 2009. **31**(4): p. 686-692.

42. Y.S.J. Yoo, H. Lim, J. Emery, and J. Kacher, *Relating microstructure to defect behavior in AA6061 using a combined computational and multiscale electron microscopy approach.* Acta Materialia, 2019. **174**: p. 81-91.

43. R. Chang, W.L. Morris, and O. Buck, *Fatigue crack nucleation at intermetallic particles in alloys — A dislocation pile-up model.* Scripta Metallurgica, 1979. **13**(3): p. 191-194.

44. A. Ghahremaninezhad and K. Ravi-Chandar, *Ductile failure behavior of polycrystalline Al 6061-T6.* International Journal of Fracture, 2012. **174**(2): p. 177-202.

45. A. Ghahremaninezhad and K. Ravi-Chandar, *Ductile failure behavior of polycrystalline Al 6061-T6 under shear dominant loading.* International Journal of Fracture, 2013. **180**(1): p. 23-39.

46. G. Le Roy, J.D. Embury, G. Edwards, and M.F. Ashby, *A model of ductile fracture based on the nucleation and growth of voids.* Acta Metallurgica, 1981. **29**(8): p. 1509-1522.

47. A.S. Argon, J. Im, and R. Safoglu, *Cavity formation from inclusions in ductile fracture.* Metallurgical Transactions A, 1975. **6**(4): p. 825.

48. A. Needleman, *A Continuum Model for Void Nucleation by Inclusion Debonding.* Journal of Applied Mechanics, 1987. **54**(3): p. 525-531.

49. M.F. Horstemeyer and A.M. Gokhale, *A void–crack nucleation model for ductile metals.* International Journal of Solids and Structures, 1999. **36**(33): p. 5029-5055.

50. J.R. Fisher and J. Gurland, *Void nucleation in spheroidized carbon steels Part 2: Model.* Metal Science, 1981. **15**(5): p. 193-202.

51. A. Stroh, *The formation of cracks as a result of plastic flow.* Proceedings of the Royal Society of London. Series A. Mathematical and Physical Sciences, 1954. **223**(1154): p. 404-414.

52. M.F. Ashby, *Work hardening of dispersion-hardened crystals.* The Philosophical Magazine: A Journal of Theoretical Experimental and Applied Physics, 1966. **14**(132): p. 1157-1178.

53. K. Tanaka, T. Mori, and T. Nakamura, *Cavity formation at the interface of a spherical inclusion in a plastically deformed matrix.* The Philosophical Magazine: A Journal of Theoretical Experimental and Applied Physics, 1970. **21**(170): p. 267-279.

54. H.G.F. Wilsdorf, *The ductile fracture of metals: A microstructural viewpoint.* Materials Science and Engineering, 1983. **59**(1): p. 1-39.

55. C.i.a. Thomson, M.J. Worswick, A.k. Pilkey, D.J. Lloyd, and G. Burger, *Modeling void nucleation and growth within periodic clusters of particles.* Journal of the Mechanics and Physics of Solids, 1998. **47**(1): p. 1-26.

56. S.H. Goods and L.M. Brown, *Overview No. 1: The nucleation of cavities by plastic deformation.* Acta Metallurgica, 1979. **27**(1): p. 1-15.

57. L.M. Brown and W.M. Stobbs, *The work-hardening of copper-silica v. equilibrium plastic relaxation by secondary dislocations.* The Philosophical Magazine: A Journal of Theoretical Experimental and Applied Physics, 1976. **34**(3): p. 351-372.

58. Z. Chen and C. Butcher, *Micromechanics modelling of ductile fracture*. 2013: Springer.

59. E. Budzakoska, D.G. Carr, P.A. Stathers, H. Li, R.P. Harrison, A.K. Hellier, and W.Y. Yeung, *Predicting the J integral fracture toughness of Al 6061 using the small punch test.* Fatigue & Fracture of Engineering Materials & Structures, 2007. **30**(9): p. 796-807.

60. R. Hu, T. Ogura, H. Tezuka, T. Sato, and Q. Liu, *Dispersoid Formation and Recrystallization Behavior in an Al-Mg-Si-Mn Alloy.* Journal of Materials Science & Technology, 2010. **26**(3): p. 237-243.

61. L. Lodgaard and N. Ryum, *Precipitation of dispersoids containing Mn and/or Cr in Al–Mg–Si alloys.* Materials Science and Engineering: A, 2000. **283**(1): p. 144-152.

62. L. Lodgaard and N. Ryum, *Precipitation of chromium containing dispersoids in Al–Mg–Si alloys.* Materials Science and Technology, 2000. **16**(6): p. 599-604.

63. T. Sato, K. Hirose, and S. Hirosawa. *Nano-cluster Controlled Precipitation in Al-Cu and Al-Mg-Si Alloys Containing Microalloying Elements*. in *Materials Forum*. 2004.

64. H. Hirasawa, *Precipitation process of Al-Mn and Al-Cr supersaturated solid solution in presence of age hardening phases.* Scripta Metallurgica, 1975. **9**(9): p. 955-958.

65. R. Kamat, J. Ng-Yelim, and S. Saimoto, *Morphology and precipitation of α-Al (Fe, Mn) Si phase in hot rolled AA3004.* Z. Metallkd, 1995. **86**(1): p. 49-53.

66. P. De Haan, J. Van Rijkom, and J. Söntgerath. *The precipitation behaviour of high-purity Al-Mn alloys*. in *Materials Science Forum*. 1996. Trans Tech Publ.

67. E. Nes, *The effect of a fine particle dispersion on heterogeneous recrystallization.* Acta Metallurgica, 1976. **24**(5): p. 391-398.

68. F.J. Humphreys, *The nucleation of recrystallization at second phase particles in deformed aluminium.* Acta Metallurgica, 1977. **25**(11): p. 1323-1344.

69. Y. Kwag and J.G. Morris, *The effect of structure on the mechanical behavior and stretch formability of constitutionally dynamic 3000 series aluminum alloys.* Materials Science and Engineering, 1986. **77**: p. 59-74.

70. L. Eschbach, P.J. Uggowitzer, and M.O. Speidel, *Effect of recrystallisation and grain size on the mechanical properties of spray formed AlCuMgAg-alloys.* Materials Science and Engineering: A, 1998. **248**(1): p. 1-8.

71. R. Behr, J. Mayer, and E. Arzt, *TEM investigations of the superdislocations and their interaction with particles in dispersion strengthened intermetallics.* Intermetallics, 1999. **7**(3): p. 423-436.

72. D. Hull and D.J. Bacon, *Chapter 7 - Jogs and the Intersection of Dislocations*, in *Introduction to Dislocations (Fifth Edition)*, D. Hull and D.J. Bacon, Editors. 2011, Butterworth-Heinemann: Oxford. p. 137-155.

73. P.J. Apps, M. Berta, and P.B. Prangnell, *The effect of dispersoids on the grain refinement mechanisms during deformation of aluminium alloys to ultra-high strains.* Acta Materialia, 2005. **53**(2): p. 499-511.

74. L. Edwards and J.W. Martin, *The Influence of Dispersoids on the Low Cycle Fatigue Properties of Al-Mg-Si Alloys*, in *Strength of Metals and Alloys (ICSMA 6)*, R.C. Gifkins, Editor. 1982, Pergamon. p. 873-878.

75. D.L. Davidson and J. Lankford, *The effects of aluminum alloy microstructure on fatigue crack growth.* Materials Science and Engineering, 1985. **74**(2): p. 189-199.

76. E. Hall, *The deformation and ageing of mild steel: III discussion of results.* Proceedings of the Physical Society. Section B, 1951. **64**(9): p. 747.

77. K. Huang, Y.J. Li, and K. Marthinsen, *Effect of heterogeneously distributed pre-existing dispersoids on the recrystallization behavior of a cold-rolled Al–Mn–Fe–Si alloy.* Materials Characterization, 2015. **102**: p. 92-97.

78. J.-F. Nie, *20 - Physical Metallurgy of Light Alloys*, in *Physical Metallurgy (Fifth Edition)*, D.E. Laughlin and K. Hono, Editors. 2014, Elsevier: Oxford. p. 2009-2156.

79. M.A. van Huis, J.H. Chen, H.W. Zandbergen, and M.H.F. Sluiter, *Phase stability and structural relations of nanometer-sized, matrix-embedded precipitate phases in Al–Mg–Si alloys in the late stages of evolution.* Acta Materialia, 2006. **54**(11): p. 2945-2955.

80. M.A. van Huis, J.H. Chen, M.H.F. Sluiter, and H.W. Zandbergen, *Phase stability and structural features of matrix-embedded hardening precipitates in Al–Mg–Si alloys in the early stages of evolution.* Acta Materialia, 2007. **55**(6): p. 2183-2199.

81. M. Murayama and K. Hono, *Pre-precipitate clusters and precipitation processes in Al–Mg–Si alloys.* Acta Materialia, 1999. **47**(5): p. 1537-1548.

82. C.D. Marioara, S.J. Andersen, J. Jansen, and H.W. Zandbergen, *Atomic model for GP-zones in a 6082 Al–Mg–Si system.* Acta Materialia, 2001. **49**(2): p. 321-328.

83. M.H. Jacobs, *The structure of the metastable precipitates formed during ageing of an Al-Mg-Si alloy.* The Philosophical Magazine: A Journal of Theoretical Experimental and Applied Physics, 1972. **26**(1): p. 1-13.

84. M. Kanno, *THE PRECIPITATION OF THETA'PHASE IN AN AL-4% CU-0, 06% IN ALLOY.* 1980.

85. X. Zhang, X. Zhou, and J.-O. Nilsson, *Corrosion behaviour of AA6082 Al-Mg-Si alloy extrusion: The influence of quench cooling rate.* Corrosion Science, 2019. **150**: p. 100-109.

86. A.K. Vasudévan and R.D. Doherty, *Grain boundary ductile fracture in precipitation hardened aluminum alloys.* Acta Metallurgica, 1987. **35**(6): p. 1193-1219.

87. S. Das, M. Heyen, R. Kamat, and R. Hamerton. *Improving Bendability of Al–Mg–Si Alloy Sheet by Minor Alloying Element Addition*. 2018. Cham: Springer International Publishing.

88. R.H. Geiss, K.P. Rice, and R.R. Keller, *Transmission EBSD in the Scanning Electron Microscope.* Microscopy Today, 2013. **21**(3): p. 16-20.

89. S. Suzuki, *Features of Transmission EBSD and its Application.* JOM, 2013. **65**(9): p. 1254-1263.

90. R.R. Keller and R.H. Geiss, *Transmission EBSD from 10 nm domains in a scanning electron microscope.* Journal of Microscopy, 2012. **245**(3): p. 245-251.

91. R. Geiss, R. Keller, S. Sitzman, and P. Rice, *New Method of Transmission Electron Diffraction to Characterize Nanomaterials in the SEM.* Microscopy and Microanalysis, 2011. **17**(S2): p. 386-387.

92. A.A. Saleh, G. Casillas, E.V. Pereloma, K.R. Carpenter, C.R. Killmore, and A.A. Gazder, *A transmission Kikuchi diffraction study of cementite in a quenched and tempered steel.* Materials Characterization, 2016. **114**: p. 146-150.

93. N. BRODUSCH, H. DEMERS, and R. GAUVIN, *Nanometres-resolution Kikuchi patterns from materials science specimens with transmission electron forward scatter diffraction in the scanning electron microscope.* Journal of Microscopy, 2013. **250**(1): p. 1-14.

94. J.J. Fundenberger, E. Bouzy, D. Goran, J. Guyon, H. Yuan, and A. Morawiec, *Orientation mapping by transmission-SEM with an on-axis detector.* Ultramicroscopy, 2016. **161**: p. 17-22.

95. G.C. Sneddon, P.W. Trimby, and J.M. Cairney, *Transmission Kikuchi diffraction in a scanning electron microscope: A review.* Materials Science and Engineering: R: Reports, 2016. **110**: p. 1-12.

96. K.P. Rice, R.R. Keller, and M.P. Stoykovich, *Specimen-thickness effects on transmission Kikuchi patterns in the scanning electron microscope.* Journal of Microscopy, 2014. **254**(3): p. 129-136.

97. P.W. Trimby, *Orientation mapping of nanostructured materials using transmission Kikuchi diffraction in the scanning electron microscope.* Ultramicroscopy, 2012. **120**: p. 16-24.

98. P.W. Trimby, Y. Cao, Z. Chen, S. Han, K.J. Hemker, J. Lian, X. Liao, P. Rottmann, S. Samudrala, J. Sun, J.T. Wang, J. Wheeler, and J.M. Cairney, *Characterizing deformed ultrafine-grained and nanocrystalline materials using transmission Kikuchi diffraction in a scanning electron microscope.* Acta Materialia, 2014. **62**: p. 69-80.

99. D.C.K. Wong, W.K. Yeoh, P.W. Trimby, K.S.B. De Silva, P. Bao, W.X. Li, X. Xu, S.X. Dou, S.P. Ringer, and R.K. Zheng, *Characterisation of nano-grains in MgB2 superconductors by transmission Kikuchi diffraction.* Scripta Materialia, 2015. **101**: p. 36-39.

100. W. Zieliński, T. Płociński, and K.J. Kurzydłowski, *Transmission Kikuchi diffraction and transmission electron forescatter imaging of electropolished and FIB manufactured TEM specimens.* Materials Characterization, 2015. **104**: p. 42-48.

101. A. Garner, A. Gholinia, P. Frankel, M. Gass, I. MacLaren, and M. Preuss, *The microstructure and microtexture of zirconium oxide films studied by transmission electron backscatter diffraction and automated crystal orientation mapping with transmission electron microscopy.* Acta Materialia, 2014. **80**: p. 159-171.

102. T. Schwarz, G. Stechmann, B. Gault, O. Cojocaru-Mirédin, R. Wuerz, and D. Raabe, *Correlative transmission Kikuchi diffraction and atom probe tomography study of Cu(In,Ga)Se2 grain boundaries.* Progress in Photovoltaics: Research and Applications, 2018. **26**(3): p. 196-204.

103. E. Pascal, S. Singh, P.G. Callahan, B. Hourahine, C. Trager-Cowan, and M.D. Graef, *Energy-weighted dynamical scattering simulations of electron diffraction modalities in the scanning electron microscope.* Ultramicroscopy, 2018. **187**: p. 98-106.

104. S. Singh and M. De Graef, *Orientation sampling for dictionary-based diffraction pattern indexing methods.* Modelling and Simulation in Materials Science and Engineering, 2016. **24**(8): p. 085013.

105. D.J. Lloyd, M. Gallerneault, and R.B. Wagstaff, *The Deformation of Clad Aluminum Sheet Produced By Direct Chill Casting.* Metallurgical and Materials Transactions A, 2010. **41**(8): p. 2093-2103.

106. L. Mattei, D. Daniel, G. Guiglionda, H. Klöcker, and J. Driver, *Strain localization and damage mechanisms during bending of AA6016 sheet.* Materials Science and Engineering: A, 2013. **559**(Supplement C): p. 812-821.

107. M. Asano, H. Uchida, and H. Yoshida, *Effect of second phase particles on the bendability of an Al-Mg-Si alloy.* Journal of Japan Institute of Light Metals, 2002. **52**(10): p. 448-452.

108. A. Davidkov, M.K. Jain, R.H. Petrov, D.S. Wilkinson, and R.K. Mishra, *Strain localization and damage development during bending of Al–Mg alloy sheets.* Materials Science and Engineering: A, 2012. **550**(Supplement C): p. 395-407.

109. A. Davidkov, R.H. Petrov, P. De Smet, B. Schepers, and L.A.I. Kestens, *Microstructure controlled bending response in AA6016 Al alloys.* Materials Science and Engineering: A, 2011. **528**(22): p. 7068-7076.

110. D. Lloyd, D. Evans, C. Pelow, P. Nolan, and M. Jain, *Bending in aluminium alloys AA 6111 and AA 5754 using the cantilever bend test.* Materials science and technology, 2002. **18**(6): p. 621-628.

111. M. Moghaddam, A. Zarei-Hanzaki, M.H. Pishbin, A.H. Shafieizad, and V.B. Oliveira, *Characterization of the microstructure, texture and mechanical properties of 7075 aluminum alloy in early stage of severe plastic deformation.* Materials Characterization, 2016. **119**: p. 137-147.

112. J.K. MACKENZIE, *SECOND PAPER ON STATISTICS ASSOCIATED WITH THE RANDOM DISORIENTATION OF CUBES.* Biometrika, 1958. **45**(1-2): p. 229-240.

113. X. Qu and Q. Deng, *Damage and recovery induced by a high energy e-beam in a silicon nanofilm.* RSC Advances, 2017. **7**(59): p. 37032-37038.

114. T.C. Lee, I.M. Robertson, and H.K. Birnbaum, *TEM in situ deformation study of the interaction of lattice dislocations with grain boundaries in metals.* Philosophical Magazine A, 1990. **62**(1): p. 131-153.

115. D.S. Park and S.W. Nam, *Effects of manganese dispersoid on the mechanical properties in Al-Zn-Mg alloys.* Journal of Materials Science, 1995. **30**(5): p. 1313-1320.

116. Y.W. Chang and R.J. Asaro, *Bauschinger effects and work-hardening in spheroidized steels.* Metal Science, 1978. **12**(6): p. 277-284.

117. M. Kikuchi, K. Shiozawa, and J.R. Weertman, *Void nucleation in astroloy: theory and experiments.* Acta Metallurgica, 1981. **29**(10): p. 1747-1758.

118. B. Bay, N. Hansen, D.A. Hughes, and D. Kuhlmann-Wilsdorf, *Overview no. 96 evolution of f.c.c. deformation structures in polyslip.* Acta Metallurgica et Materialia, 1992. **40**(2): p. 205-219.

119. D.A. Hughes, *Microstructural evolution in a non-cell forming metal: Al-Mg.* Acta Metallurgica et Materialia, 1993. **41**(5): p. 1421-1430.

120. D.A. Hughes and N. Hansen, *High angle boundaries formed by grain subdivision mechanisms.* Acta Materialia, 1997. **45**(9): p. 3871-3886.

121. D.A. Hughes and N. Hansen, *Microstructure and strength of nickel at large strains.* Acta Materialia, 2000. **48**(11): p. 2985-3004.

122. P.J. Hurley and F.J. Humphreys, *The application of EBSD to the study of substructural development in a cold rolled single-phase aluminium alloy.* Acta Materialia, 2003. **51**(4): p. 1087-1102.

123. P.J. Hurley, P.S. Bate, and F.J. Humphreys, *An objective study of substructural boundary alignment in aluminium.* Acta Materialia, 2003. **51**(16): p. 4737-4750.

124. B. Bay, N. Hansen, and D. Kuhlmann-Wilsdorf, *Deformation structures in lightly rolled pure aluminium.* Materials Science and Engineering: A, 1989. **113**: p. 385-397.

125. D. Kuhlmann-Wilsdorf and N. Hansen, *Geometrically necessary, incidental and subgrain boundaries.* Scripta Metallurgica et Materialia, 1991. **25**(7): p. 1557-1562.

126. F. Humphreys, P. Prangnell, J.R. Bowen, A. Gholinia, and C. Harris, *Developing stable fine–grain microstructures by large strain deformation.* Philosophical Transactions of the Royal Society of London. Series A: Mathematical, Physical and Engineering Sciences, 1999. **357**(1756): p. 1663-1681.

127. D.J. Lloyd and D. Kenny, *The structure and properties of some heavily cold worked aluminum alloys.* Acta Metallurgica, 1980. **28**(5): p. 639-649.

128. L.S. Tóth, B. Beausir, C.F. Gu, Y. Estrin, N. Scheerbaum, and C.H.J. Davies, *Effect of grain refinement by severe plastic deformation on the next-neighbor misorientation distribution.* Acta Materialia, 2010. **58**(20): p. 6706-6716.

129. J.R. Bowen, P.B. Prangnell, and F.J. Humphreys, *Microstructural evolution during formation of ultrafine grain structures by severe deformation.* Materials Science and Technology, 2000. **16**(11-12): p. 1246-1250.

130. D.A. Hughes and N. Hansen, *High angle boundaries and orientation distributions at large strains.* Scripta Metallurgica et Materialia, 1995. **33**(2): p. 315-321.

131. D. Kuhlmann-Wilsdorf, *Theory of plastic deformation: - properties of low energy dislocation structures.* Materials Science and Engineering: A, 1989. **113**: p. 1-41.

132. D.A. Hughes, *Microstructural evolution in a non-cell forming metal: Al・ Mg.* Acta Metallurgica et Materialia, 1993. **41**(5): p. 1421-1430.

133. J.L. Ning and D.M. Jiang, *Influence of Zr addition on the microstructure evolution and thermal stability of Al–Mg–Mn alloy processed by ECAP at elevated temperature.* Materials Science and Engineering: A, 2007. **452-453**: p. 552-557.

134. M. Furukawa, Z. Horita, M. Nemoto, R.Z. Valiev, and T.G. Langdon, *Microhardness measurements and the Hall-Petch relationship in an Al-Mg alloy with submicrometer grain size.* Acta Materialia, 1996. **44**(11): p. 4619-4629.

135. J. Wang, M. Furukawa, Z. Horita, M. Nemoto, R.Z. Valiev, and T.G. Langdon, *Enhanced grain growth in an Al-Mg alloy with ultrafine grain size.* Materials Science and Engineering: A, 1996. **216**(1): p. 41-46.

136. J. Wang, Y. Iwahashi, Z. Horita, M. Furukawa, M. Nemoto, R.Z. Valiev, and T.G. Langdon, *An investigation of microstructural stability in an AlMg alloy with submicrometer grain size.* Acta Materialia, 1996. **44**(7): p. 2973-2982.

137. M. Furukawa, Y. Iwahashi, Z. Horita, M. Nemoto, N.K. Tsenev, R.Z. Valiev, and T.G. Langdon, *Structural evolution and the Hall-Petch relationship in an Al-Mg-Li-Zr alloy with ultra-fine grain size.* Acta Materialia, 1997. **45**(11): p. 4751-4757.

138. H. Hasegawa, S. Komura, A. Utsunomiya, Z. Horita, M. Furukawa, M. Nemoto, and T.G. Langdon, *Thermal stability of ultrafine-grained aluminum in the presence of Mg and Zr additions.* Materials Science and Engineering: A, 1999. **265**(1): p. 188-196.

139. C.Y. Yu, P.L. Sun, P.W. Kao, and C.P. Chang, *Evolution of microstructure during annealing of a severely deformed aluminum.* Materials Science and Engineering: A, 2004. **366**(2): p. 310-317.

140. Y.H. Zhao, X.Z. Liao, Z. Jin, R.Z. Valiev, and Y.T. Zhu, *Microstructures and mechanical properties of ultrafine grained 7075 Al alloy processed by ECAP and their evolutions during annealing.* Acta Materialia, 2004. **52**(15): p. 4589-4599.

141. M. Ferry, N.E. Hamilton, and F.J. Humphreys, *Continuous and discontinuous grain coarsening in a fine-grained particle-containing Al–Sc alloy.* Acta Materialia, 2005. **53**(4): p. 1097-1109.

142. R.Z. Valiev and T.G. Langdon, *Principles of equal-channel angular pressing as a processing tool for grain refinement.* Progress in Materials Science, 2006. **51**(7): p. 881-981.

143. C.Y. Barlow, N. Hansen, and Y.L. Liu, *Fine scale structures from deformation of aluminium containing small alumina particles.* Acta Materialia, 2002. **50**(1): p. 171-182.

144. M. Berta, P.J. Apps, and P.B. Prangnell, *Effect of processing route and second phase particles on grain refinement during equal-channel angular extrusion.* Materials Science and Engineering: A, 2005. **410-411**: p. 381-385.

145. I. Westermann and G. Gruben, *Heat-Treatable Aluminum Alloys: Three-Point Bending.* Encyclopedia of aluminum and its alloys, 2018.

146. A. Saai, I. Westermann, S. Dumoulin, and O.S. Hopperstad, *Crystal plasticity finite element simulations of pure bending of aluminium alloy AA7108.* International Journal of Material Forming, 2016. **9**(4): p. 457-469.

147. T. Kawabata and O. Izumi, *On the intergranular fracture mechanism due to ledge formation in an Al-6.0% Zn-2.5% Mg alloy.* Journal of Materials Science, 1979. **14**(5): p. 1071-1079.

148. J.D. Evensen, N. Ryum, and J.D. Embury, *The intergranular fracture of Al-Mg-Si alloys.* Materials Science and Engineering, 1975. **18**(2): p. 221-229.

149. O. Lohne and O.J. Naess, *The Effect of Dispersoids and Grain Size on Mechanical Properties of AlMgSi Alloys*, in *Strength of Metals and Alloys*. 1979, Pergamon. p. 781-788.

150. B. Morere, J.C. Ehrström, P.J. Gregson, and I. Sinclair, *Microstructural effects on fracture toughness in AA7010 plate.* Metallurgical and Materials Transactions A, 2000. **31**(10): p. 2503-2515.

151. M. Gräf and E. Hornbogen, *Observation of ductile intercrystalline fracture of an Al-Zn-Mg-alloy.* Acta Metallurgica, 1977. **25**(8): p. 883-889.

152. W.A.P. Wen, PA, US), Wang, Yi (Los Angeles, CA, US), Hamerton, Richard (Kennesaw, GA, US), Ferreira, Adriano Manuel Povoa (Acworth, GA, US), Raeisinia, Babak (Acworth, GA, US), Wu, Zhuoru (Marietta, GA, US), Jurendic, Sebastijan (Göttingen, DE), Hegadekatte, Vishwanath (Kennesaw, GA, US), Nobrega, Carlos (Woodstock, GA, US),, *ALUMINUM ALLOYS AND METHODS OF MANUFACTURE*. 2019, Novelis Inc. (Atlanta, GA, US): United States.

153. J. Tenner, K. Andreas, A. Radius, and M. Merklein, *Numerical and experimental investigation of dry deep drawing of aluminum alloys with conventional and coated tool surfaces.* Procedia Engineering, 2017. **207**: p. 2245-2250.

154. Y.H. Moon, Y.K. Kang, J.W. Park, and S.R. Gong, *Tool temperature control to increase the deep drawability of aluminum 1050 sheet.* International Journal of Machine Tools and Manufacture, 2001. **41**(9): p. 1283-1294.

155. C.W. Sinclair, W.J. Poole, and Y. Bréchet, *A model for the grain size dependent work hardening of copper.* Scripta Materialia, 2006. **55**(8): p. 739-742.

156. L.A. Giannuzzi and F.A. Stevie, *A review of focused ion beam milling techniques for TEM specimen preparation.* Micron, 1999. **30**(3): p. 197-204.

157. M.W. Phaneuf, *FIB for Materials Science Applications - a Review*, in *Introduction to Focused Ion Beams: Instrumentation, Theory, Techniques and Practice*, L.A. Giannuzzi and F.A. Stevie, Editors. 2005, Springer US: Boston, MA. p. 143-172.

158. S. Zaefferer, S.I. Wright, and D. Raabe, *Three-Dimensional Orientation Microscopy in a Focused Ion Beam–Scanning Electron Microscope: A New Dimension of Microstructure Characterization.* Metallurgical and Materials Transactions A, 2008. **39**(2): p. 374-389.

159. H. Qiu, L.N. Wang, T. Hanamura, and S. Torizuka, *Prediction of the work-hardening exponent for ultrafine-grained steels.* Materials Science and Engineering: A, 2012. **536**: p. 269-272.

160. N. Claussen, *Strengthening strategies for ZrO2-toughened ceramics at high temperatures.* Materials Science and Engineering, 1985. **71**: p. 23-38.

161. T.B. Britton, J. Jiang, Y. Guo, A. Vilalta-Clemente, D. Wallis, L.N. Hansen, A. Winkelmann, and A.J. Wilkinson, *Tutorial: Crystal orientations and EBSD — Or which way is up?* Materials Characterization, 2016. **117**: p. 113-126.

162. D. Goran, J.R. Michael, and B.B. McKenzie, *Advantages of TKD in SEM using on-axis detector.*

163. F. Niessen, A. Burrows, and A.B.d.S. Fanta, *A systematic comparison of on-axis and off-axis transmission Kikuchi diffraction.* Ultramicroscopy, 2018. **186**: p. 158-170.

164. E. Brodu, E. Bouzy, and J.J. Fundenberger, *Diffraction contrast dependence on sample thickness and incident energy in on-axis Transmission Kikuchi Diffraction in SEM.* Ultramicroscopy, 2017. **181**: p. 123-133.

165. H. Yuan, E. Brodu, C. Chen, E. Bouzy, J.J. Fundenberger, and L.S. Toth, *On-axis versus off-axis Transmission Kikuchi Diffraction technique: application to the characterisation of severe plastic deformation-induced ultrafine-grained microstructures.* Journal of Microscopy, 2017. **267**(1): p. 70-80.